SURFACE STRUCTURE EVOLUTION AND H UPTAKE OF NICKEL UNDER CATHODIC CHARGING

A Dissertation

by

LAI JIANG

Submitted to the Graduate and Professional School of
Texas A&M University
in partial fulfillment of the requirements for the degree of

DOCTOR OF PHILOSOPHY

Chair of Committee,	Michael J. Demkowicz
Committee Members,	Bilal Mansoor
	Homero Castaneda-Lopez
	George Mathews Pharr V
	Raymundo Case
Head of Department,	Ibrahim Karaman

December 2021

Major Subject: Materials Science and Engineering

ABSTRACT

Nickel (Ni) being a member of the transition metal series, possess excellent corrosion-resistant properties that it has been widely used as key alloying elements for stainless fabrication as well as other nickel-based alloys with high corrosion and temperature resistance. Additionally, as a group 10 metal, it has the comparable catalytic performance to the more rare and precious Palladium (Pd) and Platinum (Pt). Due to its abundance by weight in the earth crust and readiness to be mined and refined, Ni becomes a low-cost substitution catalyst for many catalytic reactions such as hydrolysis, cross-coupling chemical reactions, and reforming reactions. Because of all these mentionings above, Ni is frequently exposed to the aqueous environment that contains hydrogen. Ni as a cathode under cathodic charging is a very typical situation and gradually drawing more and more attention and interest to its research during the recent decades.

In this dissertation, the goal of the research presented here is to investigate the structure and properties of Ni surface under cathodic charging as there was remarkably little information about the surface on Ni under cathodic charging was known from previous studies. Only XRD and SEM observations were commonly conducted by previous investigations, not to mention that the XRD detection range is also relatively narrow that surface changes fall outside this range may be overlooked. Therefore, in the first part of the dissertation, more advanced, thin-film specialized 2D-XRD measurements are conducted, along with a wide range of surface characterization techniques. As a result, the surface phases that are rich in Ni-O-S-H have been successfully observed. These phases partially cover the Ni surface with ~150 nm thickness and have surface potential that is cathodic compared to the surrounding Ni surface. These phases are proposed to be the decay product of the oxidation reactions of some Ni surface hydride with the electrolyte. Such unique crystallographic structure, electrochemical and mechanical properties are highly likely to cause various degradation and performance breakdowns such as localized corrosion, electrode deactivation, and hydrogen embrittlement.

Following the findings of the first part, hydrogen concentration measurements of cathodically charged Ni are conducted as an indirect way to infer the surface hydrogen concentration and seek the existence of surface hydride. It shows that the amount of hydrogen that can diffuse into the Ni is not governed by electrochemical parameters such as overpotential or current. In fact, it is surface H coverage dependent. Additionally, the un-restricted current density at full hydrogen surface coverage is found to be related to the switching of the hydrogen evolution reaction pathway. The full hydrogen coverage at the Ni surface under cathodic charging provides necessary but not sufficient conditions for the surface hydride formation.

Finally, the third part of the thesis demonstrates observation of localized corrosion pitting that initiated on Ni surface under cathodic charging. These localized corrosion features are found to occur when surface hydrogen, as well as surface phases introduced in the first part, reach their full coverage. The change of semiconducting behavior and existence of Aluminum impurity inclusions that are preferentially located inside the corrosion pittings are hypotheses to be related to the surface passive film breakdown and corrosion initiation.

DEDICATION

This dissertation is dedicated to both my paternal and maternal grandfather, their benevolent smiles are always in my mind and they are forever alive in my heart.

ACKNOWLEDGEMENTS

Particularly, I would like to give my sincerest thanks to my advisor, Dr. Michael J. Demkowicz. His passion, vision, and perceptive senses of science always shed light on my path towards the truth. His rigor and attention to detail inspired me to demand more from myself to be qualified and capable in academia. He is also extremely patient when it comes to explaining the concept, going through the derivation, and correcting my mistake. I am so grateful for this guidance during my Ph.D. to make me not only a better scientist but also a better person.

I would like to acknowledge my committee members, Dr. Homero Castaneda, Dr. Matt Pharr, Dr. Raymundo Case, and Dr. Bilal Mansoor. Their insightful discussion, useful guidance, and inspiring encouragement enable me to go this far and successfully finish my research.

Next are my collaborators, Dr. Emile Schweikert and Dr. Stanislav Verkhoturov, who provide important research support and useful discussion for my study.

I would also like to thank all the research staff that assists me with all the experiments and measurements: Dr. Jesus I Barraza-Fierro, Dr. Anup Bandyopadhyay, Dr. Bryan Tomlin, Dr. SiSi Xiang, Dr. Winson Kuo, and Dr. Wilson Serem.

Thanks also go to my colleagues and friends: Dr. Mengying Liu, Dr. Yuwei Zhang, Dexin Zhao, Qing Zhou, and Zeyi Tan. They not only provide valuable support and discussion in research but also create a harmonious and friendly atmosphere in ordinary life. Getting along with them always makes me happy, supported and joyful.

I am also very grateful to my fiancée, who always being incredibly loving, supportive, patient, and considerate. It is her perseverance in this long-distance relationship that gives me confidence and encourages me to finish my research and Ph.D.

Last but by no means the least, as cliché as it may sound, this accomplishment can not be possible without the support from my family. My parents always devote their love and support not only financially but also mentally. Whenever I get frustrated, they are always my most solid and dependable backup. I can not express more gratitude towards the upbringing and education of my parents and I am so proud to be proud of them. All I am, I can, owe to my dear parents.

CONTRIBUTORS AND FUNDING SOURCES

Contributors

The work of this dissertation is supervised by a dissertation committee led by Professor Michael J. Demkowicz of the Department of Materials Science and Engineering and consist of Professor Bilal Mansoor of Texas A&M Qatar, Professor Homero Castaneda-Lopez of the Department of Materials Science and Engineering, Professor George Mathews Pharr V joint appointed in the Department of Mechanical Engineering and Department of Materials Science and Engineering and Professor Raymundo Case of the Department of Materials Science and Engineering.

The XRD measurements are conducted by Dr. Anup Bandyopadhyay in the Department of Materials Science and Engineering at Texas A&M University, the SIMS measurements are conducted by Dr. Stanislav Verkhoturov in the Department of Chemistry at Texas A&M University and the ICP-MS measurements are conducted by Dr. Bryan Tomlin in the Department of Chemistry at Texas A&M University. All other work conducted for the study of this dissertation was completed by myself independently.

Funding Sources

My PhD study is supported by NPRP grant #11S-1129-170045 from the Qatar National Research Fund (a constituent member of the Qatar Foundation). The SIMS measurements are carried out using resources at Department of Chemistry supported by NSF grant CHE-130812.

NOMENCLATURE

2D	Two-dimensional
AFM	Atomic force microscope
ATR-FTIR	Attenuated total reflection-Fourier transform infrared
C_H	Equilibrium hydrogen concentration
EBSD	Electron backscatter diffraction
EDS	Energy-dispersive X-ray spectroscopy
θ	Hydrogen surface coverage
H	Hydrogen
HER	Hydrogen evolution reaction
KPFM	Kelvin probe force microscope
t_{on}	Time when potentiostat is on
t_{off}	Time when potentiostat is off
OCP	Open circuit potential
SCE	Saturated calomel electrode
SIMS	Secondary ion mass spectrometry
XRD	X-ray diffraction

TABLE OF CONTENTS

Page

LIST OF FIGURES

LIST OF TABLES

Page

1. LITERATURE REVIEW

1.1 Cathodic charging of Ni

Cathodic charging is an electrochemical process that based on an electrochemical cell, in which Ni acts as the cathode, and usually, a piece of platinum acts as the anode, both submerged in an electrolyte. Figure 1 shows the schematic diagram of cathodic charging on Ni.

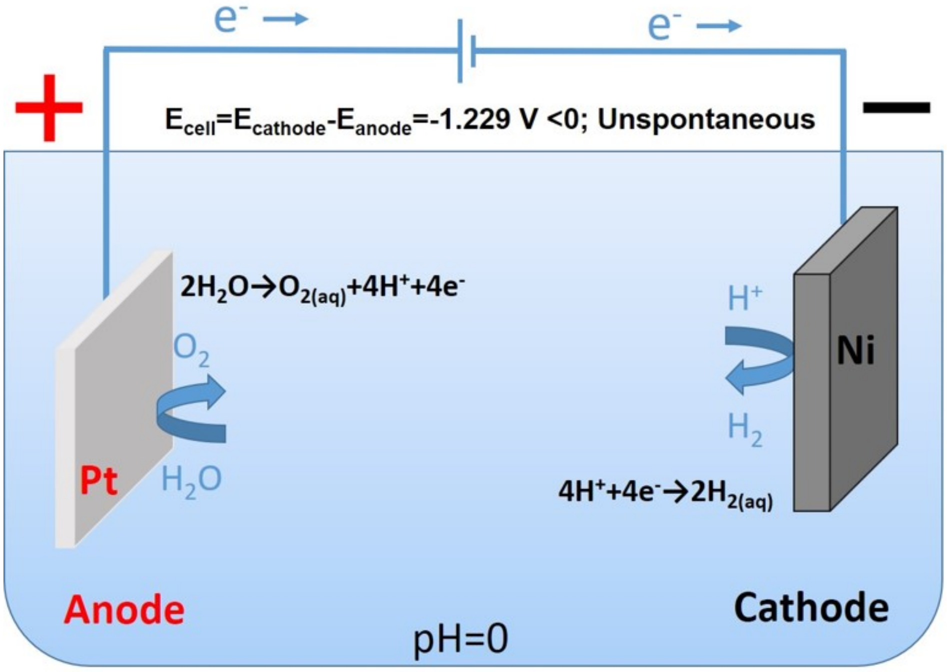

The cathodic potential is applied at the sample surface to drive electrons to flow towards the sample and introduce a reduction reaction. In a water-based electrolyte environment, the electrolytic solution will decompose, hydrogen ions will be produced and combine with electrons at the Ni surface to generate hydrogen atoms. Hydrogen atoms will either combine with other hydrogen atoms to form an H_2 molecule or become absorbed H and diffuse into Ni.

1.2 Effect of cathodic charging on Ni surfaces

Cathodic charging has long been suspected to change the Ni surface structure and properties in different ways. Previous studies showed that Ni under cathodic charging could be charged with hydrogen to a concentration as high as 0.7 hydrogen atoms per Ni atom[1]. Although they claimed that the diffused hydrogen has virtually no effect on the lattice structure of Ni, The cathodic charging process on the Ni surface are reported to form H/Ni phase that has an FCC crystal lattice and its lattice parameter a is approximately 6% larger than that of Ni which measured by using XRD[2].

As structure and properties are closely related, change of surface structure usually comes with the change of various properties of Ni. Ni is a good catalyst for electrolytic hydrogen production that has been reported that will gradually lose the HER activity compared to the fresh Ni electrodes after several hours of water electrolysis[3, 4]. Besides, cathodic charging also influences the mechanical properties of the Ni surface. A study reported an increase of hardness at the Ni surface as cathodic charging introduce hydrogen into Ni[5]. However, a recent study also shows that hydrogen produced by cathodic charging affects the elastic properties as well as plastic deformation[6]. It reported a ~ 22% decrease of elastic modulus after hydrogen charging and also a change of plastic deformation behavior.

1.3 Effect of cathodic charging on other materials

A similar effect on aluminum has been reported[7] that cathodic charging produced a severely hardened surface with higher hardness along with reduced ductility and increased yield and tensile strength. Bond et al[8]. studied the effect of cathodic charging on aluminum and found that diffused hydrogen from the charging process enhances the dislocation mobility and reduces the flow stress. Steel, as a good choice of materials for its good resistance to the harsh environment, is inevitable to a cathodic charging environment and therefore has been investigated. Several studies[9, 10] reported degradation of various mechanical properties including decreased ductility, lower elasticity, and plasticity, on different steels under cathodic polarization.

The influence of cathodic charging on the mechanical behavior of brass was also studied[11]. Under the condition of cathodic charging with constant current density, the microhardness of H-charged surface layers increased with increasing charging time. The increasing current density also increases the surface layer microhardness under the same charging time. It is also reported that the cathodic charging on brass can reduce the ductility as well as the UTS to some extent.

Cathodic charging showed a similar effect on alloys such as Al-4Zn-1Mg[12], it hardens the alloy surface, decreases the UTS, and also causes the transformation of ductile intergranular fracture to brittle transgranular fracture in the outer H-charged surface layer.

1.4 Previous studies on cathodic charged Ni

Surface structure and mechanical properties wise, cathodic charging on Ni causes uptake of H into the material resulting in embrittlement and cracking [13, 14]. Under some conditions, cathodic charging also leads to the onset of localized intergranular corrosion [15].

Catalytic performance-wise, the activity of Ni being as a catalyst for the HER is observed to decrease progressively over time [3, 4]. It often shows as a gradually decreasing current density under the same overpotential with increasing charging time.

Previous studies have used x-ray diffraction (XRD) to evaluate cathodically polarized Ni surfaces to elucidate the loss of Ni surface characteristics during charging[1, 16, 17]. They identified the presence of additional Bragg diffraction peaks that were not Ni-related and interpreted them as evidence of Ni hydride formation. Because there are no thermodynamically stable compounds in the Ni-H binary system at atmospheric pressure [18], the proposed hydrides would have to be metastable, which means that the new diffraction peaks should gradually fade once the charged samples are removed from the electrolyte. It has been proposed that surface hydrides may be responsible for H embrittlement [13, 14] and deactivation of the HER [3, 4]. All these earlier investigations, on the other hand, were limited to a narrow range of diffraction angles, with 2θ falling between ~42° and ~54°. As a result, any other surface phases that could have contributed to Bragg diffraction peaks outside of this range would have gone unnoticed.

1.5 Previous studies on other cathodic charged materials

As the cathodic charging usually creates hydrogen exposure to the metal surface, many relevant studies in this area are focusing on the investigation of possible hydride existence and formation.

Song *et al* [19] studied the corrosion behavior of AZ91 alloy in 1N NaCl at pH 11 under both cathodic and anodic polarization. By simultaneously measuring the hydrogen evolution rate and the magnesium dissolution rate using the gas collection method and ICP (the technique that we also used), they found out that under cathodic polarization, anodic dissolution of Mg not only occur, but the dissolution rate is also comparable to the hydrogen evolution rate. This suggests that Mg dissolution can occur independent of the polarization and may also be related to the hydrogen evolution. They explained this by proposing that both magnesium dissolution and hydrogen evolution occur in a coupled manner in a phase (possibly Mg hydride) at the surface with exposure to the water that metallic magnesium is oxidized into univalent ions and then react with water to produce hydrogen gas and Mg^{2+}.

Chen *et al* [20] followed up this proposed mechanism while investigating the possible cathodic charging induced surface structure changes of AZ91 alloy in 3.5 wt% NaCl solution at pH 7 and its influence on the negative difference effect (NDE) with special attention to the cathodic Mg dissolution process. Using gas collection method, potentiostatic test, and also thermodynamic calculation, they found out the calculated current density based on the evolved H_2 gas was less than the measured current density in high cathodic polarization region, which implied there was another cathodic reaction, presumably hydride formation, consumes electrons besides hydrogen evolution. The Gibbs energies of the formation of Mg^{2+} and $Mg(OH)_2$ are below zero, suggesting that MgH_2 is unstable and will spontaneously react with water and decompose into $Mg(OH)_2$ that has Mg^{2+} oxidized state and hydrogen gas. Thus, they concluded that the corrosion behavior of AZ91 alloy at the cathodic region is consists of Mg hydride formation during cathodic polarization and its decomposition when reacting with water into Mg hydroxide and hydrogen gas. They also mentioned that Mg hydride is possible to form in the whole pH range based on the thermodynamic calculations of MgH_2 and the Pourbaix diagram of Mg-H_2O.

Williams *et al*[21] advanced the understanding of this corrosion mechanism of hydride formation and decomposition reaction of water to produce Mg hydroxide by using in situ scanning vibrating electrode technique (SVET) to characterize the localized corrosion occurring on unpolarized Mg in 5% wt NaCl electrolyte at pH 6.5. The corrosion features are shown to consist of a cathodic center of Mg hydroxide and an anodic ring of possibly Mg hydride, in which the local corrosion currents around the cathodic center are prominent while the currents emerging away from the cathodic center are negligible by comparison. This suggests that the anodic decomposition process of Mg hydride tends to occur right next to the cathodic center as it is the least resistive for electron transfer.

1.6 Summary

The behavior of nickel (Ni) surfaces under cathodic polarization in an aqueous electrolyte is a key concern in several technologically important scenarios. Ni is one of the most effective catalysts for the hydrogen evolution reaction (HER) and is therefore often used as the cathode in hydrolysis applications[22-25]. Because of their low susceptibility to corrosion[26], Ni-base alloys are frequently deployed in chemically aggressive environments, such as sour wells[27, 28]. To further protect them against oxidation, they are maintained at a negative (cathodic) potential with respect to their environment[29, 30]. In both of these examples, changes in Ni surface composition and structure induced by cathodic charging are thought to cause an eventual breakdown in performance. In hydrolysis on Ni surfaces, the HER is observed to deactivate progressively over time[3, 4]. Cathodic polarization of Ni causes uptake of hydrogen (H) into the material resulting in embrittlement and cracking[13, 14]. Under some conditions, cathodic charging also leads to the onset of localized intergranular corrosion[15]Cathodic charging has long been suspected to change the surface structure as well as properties of Ni surface. However, remarkably little about the surface of Ni under cathodic charging is known. The only crystallographic structure has been studied by using XRD that they claimed the discovery of new surface phases on Ni surface during cathodic charging, other information such as its elemental composition, mechanical and electrochemical properties remain unknown.

Therefore, to fully understand the evolution of Ni surface under cathodic charging and how it affects the properties and performance of Ni in various technological application scenarios, more in-depth and complete investigation is urgently needed. The investigation includes many aspects such as surface characterization on crystallography, elemental composition, surface morphology and measurements of hydrogen content, electrochemical properties as well as mechanical properties.

2. EXPERIMENTAL METHODS

2.1 Sample preparation

All experiments were performed using 50µm-thick, 99.98% pure, annealed Ni foils from Alfa Aesar. Table 1 is the composition information of the foil reported by the supplier. The foils were cut into rectangular samples of 4 cm (1.5 cm) in length. One end of the Ni foil is soldered to a wire, which is then inserted into a glass tube, which serves as electrolyte insulation for the wire during cathodic charging. Only nickel foil makes contact with the electrolyte during charging, thus the end of the glass tube is likewise covered with epoxy. By completing these steps, the potentiostat's measured potential, current, and charge are identical to those on the sample, ensuring accuracy.

The as-received foil has a roughness of about 100 nm on the surface. The foils were polished to a roughness of 5 nm to aid in the EBSD investigation. They were then charged cathodically with 1M H2SO4 and 1g/L NaCl to increase conductivity.

Element	Ni	Fe	Mn	Si	C	Cu	Co	S	Other
Weight %	99.34	0.13	0.262	0.082	0.014	0.006	0.005	0.0003	Balance

Table 1: Chemical composition of as-received Ni foil.

2.2 Cathodic charging

The cathodic charging system is a conventional 3-electrode setup based on the multiport corrosion cell kit from Gamry connected to a VersaStat 3F potentiostat from Ametek. The Ni foil is the working electrode while a platinum wire acts as the counter electrode. The reference electrode is a saturated calomel electrode inserted into a lugging capillary to make sure the distance between the reference electrode and the working electrode is as small as possible.

All samples were rinsed and ultrasonicated in acetone before being immersed into the electrolyte. Charging was conducted at room temperature and pressure under a 400mV constant overpotential for times ranging from 15 minutes to 20 hours. The relationship between open circuit potential (OCP), overpotential η, and total applied potential E can be described by the following equation: $E = OCP + \eta$. Figure 2 shows potential history from one of the cathodic charging experiments to illustrate how using this periodic charging method to maintain constant overpotential.

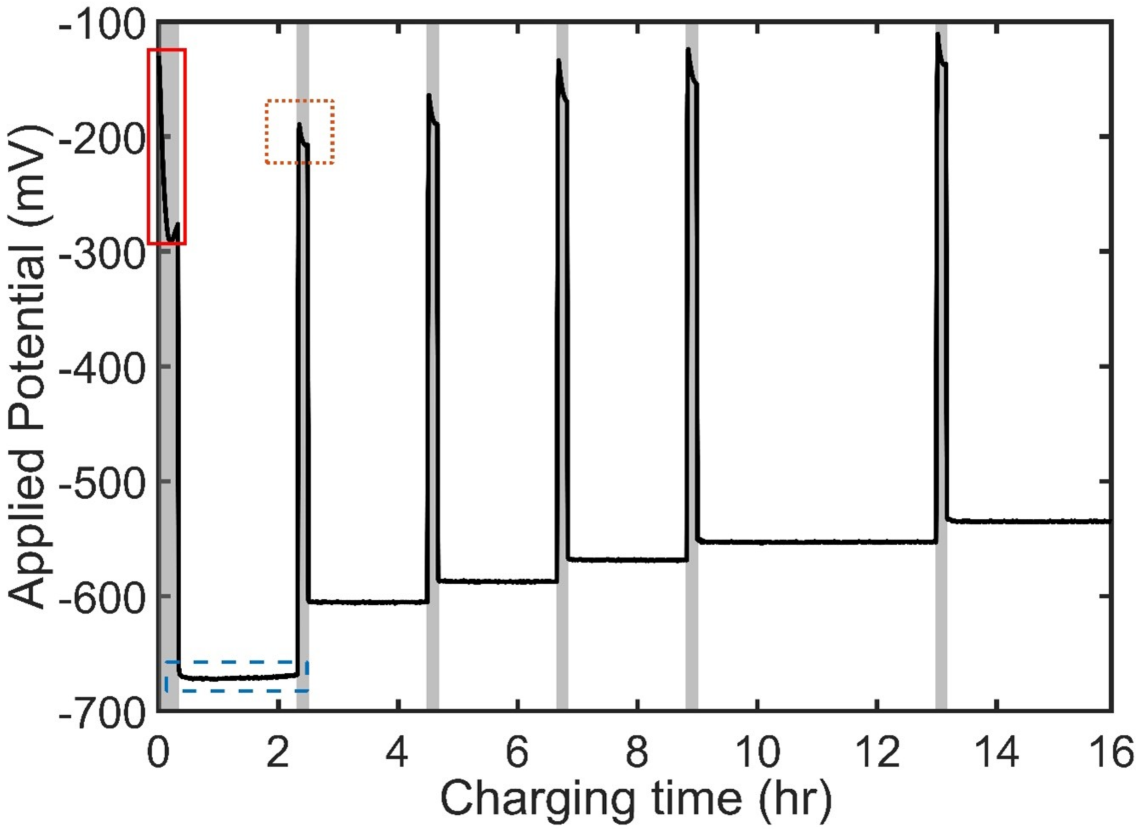

Figure 2: Applied potential during a typical charging run. The shaded areas represent moments when there is no external potential applied. As a result, the open circuit potential is measured during those times (OCP). The solid red box depicts the initial 10 minute immersion period with the potentiostat turned off. The initial charging period under 400mV overpotential is depicted by the blue dashed box. The first interruption of the applied potential to measure the change in OCP is shown in the orange dotted box.

Constant overpotential was maintained throughout the entire charging process by measuring the open circuit potential every two hours and updating the total applied potential applied on the sample accordingly. To assess the influence of periodic interruptions on Ni surface structure, charging experiments under constant current density without any interruption are also conducted. The state of the Ni surface was comparable for both of these charging protocols. After charging, samples were taken out and gently dried by using kimwipes. Selected samples were further rinsed in deionized water and ultrasonicated in acetone. After H charging, samples were taken out and gently dried by using kimwipes. Selected samples were further rinsed in deionized water and ultrasonicated in acetone.

2.3 Surface characterization

2.3.1 X-ray Diffraction (XRD)

Although previous studies on the Ni surface under cathodic charging have used XRD to characterize the crystallographic structure of the Ni surface, its accuracy, detection limit, and resolution are limited due to the capabilities of the XRD instruments. Besides, the scanning 2θ values are pretty narrow, from ~40° to ~55°. These limitations would somehow cause some other cathodic charging-induced structure changes that fall outside this range to be overlooked. Which means they might lose the whole forest just for the trees.

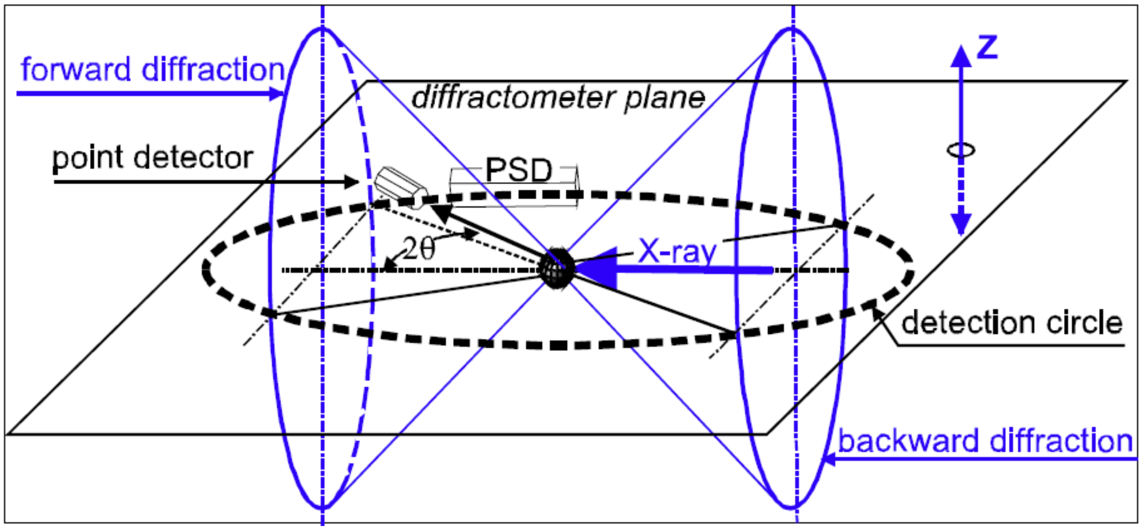

Figure 3: Comparison of the 2-D XRD and conventional XRD.

For conventional XRD, the point detector only moves in the detection circle within the diffractometer plane. This technique uses a diffractometer with a two-dimensional detector, which makes the diffractor itself no longer being confined within the diffractometer plane. The 2-D detector itself can be considered as a moving plane along the detection circle, which intersects with the forward or backward diffraction cones to form a conic section. These conic sections will produce Debye rings that have different shapes based on the detector swing angle. Therefore, the 2-D diffraction pattern can carry much more information than the conventional diffraction pattern, including PhaseID; Percent crystallinity; particle size and shape; texture; and stress. As 2-D detectors can collect diffraction data in a large 2θ range simultaneously without sample or detector movement, they can have much higher information throughput. Therefore, it can also give better intensity so that it can distinguish those small changes of the diffraction peaks which conventional XRD is unable to distinguish. The scanned range of 2θ values is from 12° to 70° and the scanned sample area is 100mm^2. The value of the angle that represents the rotation of the sample holder with respect to the axis normal to the sample, ϕ, was maintained at a constant optimum value. The optimal value is determined by performing a series of scans with different ϕ ranging from 0° to 90°and choosing the one that gives the strongest XRD signal.

2.3.2 Kelvin Probe Force Microscopy (KPFM)

Kelvin probe force microscopy (KPFM) analysis is performed using the KPFM mode in the Dimension Icon atomic force microscope (AFM) from Bruker. A 2500um^2 area is scanned, consisting of 256 line-by-line scans with a scan rate of 0.3 Hz. All the KPFM measurements were performed at room temperature and in the air. There is some convention regarding surface potential worth being explained here. In KPFM, the probe tip and sample surface are electrically connected to form a parallel plate capacitor. With no external potential applied, an electrical current flows through the circuit to equalize the Fermi levels of the sample surface and probe tip. As charge accumulates at the tip and in the sample, a potential difference develops between them, known as the contact potential,

V_c. The operating principle of KPFM is to apply a counteracting voltage V_b on the probe tip so that this charge difference is nullified. Therefore, when V_b equals $-V_c$, the charge difference disappears. The potential map shows V_b. Therefore, positive values in the potential map correspond to negative values of V_c. Moreover, when comparing any two V_b values on the map, the one that is more cathodic is the one with a higher V_b value.

2.3.3 Atomic Force Microscopy (AFM)

Atomic force microscopy (AFM) analysis is performed using the AFM mode in the Dimension Icon atomic force microscope (AFM) from Bruker. A $2500\mathrm{um}^2$ area is scanned, consisting of 256 line-by-line scans with a scan rate of 0.3 Hz. All the AFM measurements were performed at room temperature and in the air.

2.3.4 Energy-dispersive X-ray spectroscopy (EDX)

Scanning electron microscopy (SEM) was performed using an LYRA FIB-SEM. EDS characterization was done using an Oxford Instruments detector integrated into the LYRA FIB-SEM. The scanned area is 180 μm×140 μm and the interval between each sampling point is 0.5 μm. Elements that were selected for detection using the EDS included O, S, Na, Cl, Ni, and C.

2.3.5 Electron Back-Scattered Diffraction (EBSD)

EBSD measurements were performed using an Oxford Instruments detector integrated into a FERA FIB-SEM. The scanning parameters are the same as for EDS.

EBSD data were analyzed to identify the orientation of pure Ni grains. Surface phases with crystal structures and lattice parameters different than that of pure Ni, therefore, show up as dark, un-indexed regions in our EBSD maps.

2.3.6 Secondary Ion Mass Spectrometry (SIMS)

SIMS measurements were run using a custom-built instrument with a C_{60} buckminsterfullerene effusion source[33]. C_{60} particles are accelerated individually to 50 keV and impact within a 200μm-diameter region on the target at an angle of incidence of 25 ° from normal with a repetition rate of 1000 impacts/s. Each impact generates secondary ion ejecta from a region approximately 100nm^2 in the area and 5nm in depth. The mass spectra of ejecta created by each impact are acquired separately. Therefore, this technique enables the assessment of variability in local compositions over distances of ~10nm on the analyzed surface, albeit without position information. Moreover, the mass spectrometer may be polarized to filter out either positively or negatively charged ions. This capability was used to filter out Ni^+ ions, which are expected to make up the majority of ions ejected from the surface and would otherwise have created a substantial background signal in our measurements. The spectra reported here contain negatively charged, S- and O-bearing atomic clusters, exclusively. Thus, the SIMS measurement is specific to the surface phases of interest in the present study.

2.3.7 Attenuated Total Reflection-Fourier Transform InfraRed (ATR-FTIR)

To test for carbon(C)-based surface contaminants, ATR-FTIR measurements were performed using a TENSOR II FTIR Spectrometer with an ATR attachment. Prior to testing the Ni samples, a background measurement against air was run and compared with previous background measurements to verify proper calibration. Surfaces of as-received samples were carefully cleaned to ensure they are free of C contaminants prior to ATR-FTIR measurements. H charged sample surfaces were gently dried using kimwipes without rinsing or ultrasonication.

2.3.8 Inductively-Coupled Plasma Mass Spectrometry (ICP-MS)

These ICP-MS measurements were run using a Perkin Elmer NexION 300D instrument. 10ug/mL Ni standard solution was used for calibration before the measurements. 25mL samples of electrolyte were extracted after 0, 5, 16, and 20 hours of charging. This measurement has a detection limit of 0.006μg/L and uncertainty of 3% at 1s (68% confidence level).

2.4 Hydrogen content measurement

The hydrogen content of Ni samples was determined using the G8 Galileo ON/H analyzer from Bruker which operates based on melt extraction methods. Fig. 4 is a diagram illustrating the melting extraction method.

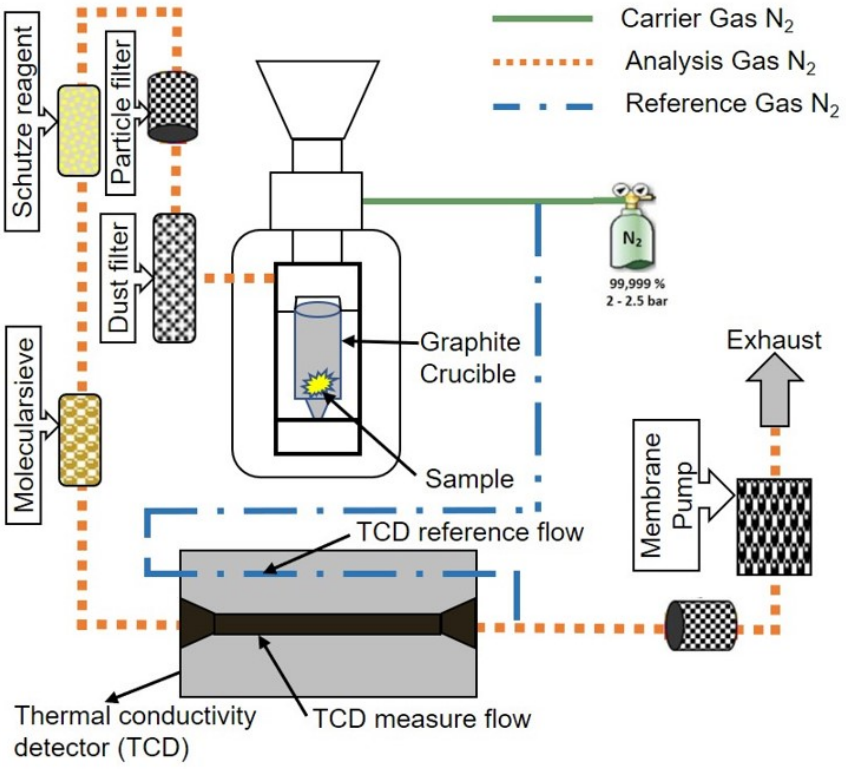

Figure 4: Schematic diagram of G8 Galileo ON/H analyzer

Sample with required dimensions will be inserted via the funnel on top of the chamber. Once it is dropped inside the crucible which has been purged to remove all the moisture and impurities before, a high current will be applied through the crucible to raise the temperature above the melting temperature. A sample will be melted inside the chamber in dozens of seconds and a carrier gas flow (pure N_2 for H, pure He for O and N) will be pumped into the chamber to carry all the elemental content released from the sample through several chemical filters. These filters will further remove the residual moisture and impurities to assure measurement accuracy. Carrier gas flow will eventually go through a thermal conductivity detector (TCD) which can measure the conductivity variation caused by the ON/H content. In the meanwhile, a reference gas flow that has the same composition as the carrier gas flow except it does not carry any elemental content from the sample, will also go through the TCD. By knowing the difference of conductivity between carrier gas flow and reference gas flow, the ON/H content can be determined. Each measurement takes 2-3 mins and is performed in 5 mins right after the charging is complete and extraction of the sample from the electrochemical cell. Therefore, although outgassing of hydrogen in this period can be compensated by using the 1-D diffusion solution for H in Ni, the amount of the outgassing H is negligible compared to the H content inside the Ni sample.

The instrument is calibrated using ASTM standard samples from Alpha Resources at regular intervals.

2.5 Surface current distribution measurement

Surface current distribution measurement was conducted based on the VersaSCAN scanning electrochemical systems from AMETEK. The Scanning Vibrating Electrode Technique (SVET) uses a sharp conductive tip to measure the voltage drop of a very small vicinal space. This voltage drop is a result of the local currency at the sample surface. Therefore, the voltage mapping of the Ni surface under cathodic charging can be transformed into current mapping by using the as-tested polarization curve of the Ni foil. Figure 5 shows an example of the potential map output directly from the instrument.

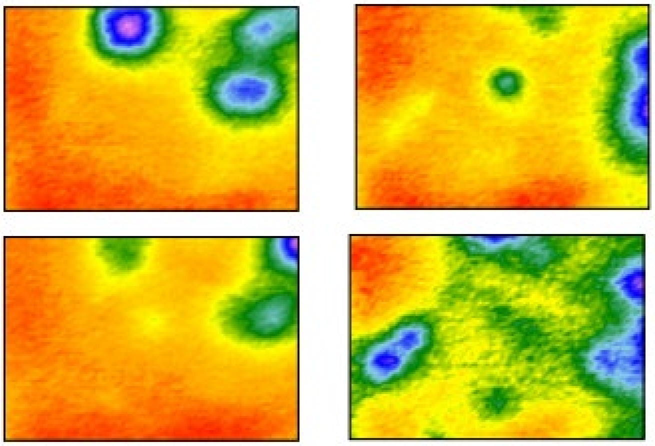

Figure 5: Time-resolved S-VET mapping of the same area of a continually corroding sample taken at the different times being exposed to the electrolyte.

The diameter of the detection tip is ~10 µm, therefore, the instrument can distinguish voltage variation with a spatial resolution down to 10 µm. As each point scan will take dozens of seconds and the Ni surface is large. The total scanning time will be very long if the scanning is running every 10s, this can cause the state of the surface at the beginning of the scanning to differ greatly from the state of the surface at the end of the scanning. Therefore, the scanning interval of the measurement has been set to 20 µm and the total scanning area is 200 µm x 200 µm.

3. FORMATION OF NI-O-S-H SURFACE PHASES DURING CATHODIC CHARGING[*]

3.1 Introduction

As mentioned in the previous introduction section, cathodic charging has long been suspected to change the surface structure of Ni. Previous studies reported cathodic charging-induced surface structures on Ni, including lattice expansion determined by Ni peak shift to lower 2θ and new surface phase formation indicated by new XRD peaks. However, all these studies were lack of other characterizations than just XRD and SEM. Besides, the XRD detection range is pretty narrow, only from 40° to 56°). With this narrow detection range, some other cathodic charging-induced structure changes may be overlooked. Which means they might lose the whole forest just for the trees.

To further understand the surface structure evolution of cathodically charged Ni, in this study, further and more complete characterization of the surface structure and properties of Ni is conducted. This includes using a more advanced, thin-film specialized 2D-XRD with better sensitivity and a much wider 2theta range (up from 40°-50° to 20°-70° based on Cu Ka X-ray source) and other site-specific surface characterizations like EBSD, EDS, SIMS, AFM, and KPFM. Additionally, a phase formation mechanism based

---

[*] Part of this chapter was reprinted with permission from "Formation of Ni-O-H-S surface phases on cathodically charged Ni" by Jiang, L.; Verkhoturov, S.; Schweikert, E.; Demkowicz, M. J., 2021, *Corrosion Science*, Vol 185, 109424, Copyright © 2021, Elsevier Ltd.

on the oxidation reaction of some Ni surface hydride with electrolyte is proposed in answering the new phases discovered in this study.

3.2 Cathodic charging experiments

To develop a complete view of the formation and stability of surface phases on cathodically charged Ni, various measurements were carried out on samples prepared in several different ways:

- As-received Ni foils. These samples provide a baseline for comparison against all other samples.
- Ni foils charged cathodically over durations ranging from 15 minutes to 20 hours. To retain the resulting surface phases intact, these samples were only gently dried after extraction from the electrolyte and before characterization.
- Ni foils charged cathodically over durations ranging from 1 to 7 hours and cleaned by ultrasonication upon extraction from the electrolyte. As will be shown, these samples are free of surface phases. They enable us to assess the state of the bare Ni foils after charging while excluding the effect of the surface phases.
- Ni foils charged cathodically over durations ranging from 3 to 20 hours, gently dried upon extraction from the electrolyte (leaving surface phases intact), and left in air for up to 48 hours before characterization. These samples allow us to assess the stability of the surface phases in air.

In the following sections, findings on the crystallography, composition, topography, and electron work function of surface phases formed on cathodically charged Ni are presented.

3.3 Surface characterizations

The first surface characterization technique being used is 2-D XRD, which gives an overall determination of whether new phases with the distinctive crystallographic structure were formed on the Ni sample surface during cathodic charging. However, since the Braggs diffraction peaks from the XRD are collective average signals coming from the scanning area, the result does not contain any positional and distributional information about the new phases. In order to know how these new surface phases distribute at the Ni sample surface and what is the extent of the coverage, EBSD measurements were performed. Indexing only the pure FCC Ni is enough to distinguish the new surface phases from the Ni substrate.

After confirming the existence of new phases and acquiring information about the distribution on the Ni surface, EDS measurements were then performed in order to characterize the elemental composition of these new phases. As the probing depth of EDS is relatively deep and it is unable to detect hydrogen, ToF-SIMS measurements were also applied as a complimentary compositional characterization technique. Hydrogen was also detected by using the ToF-SIMS, but quantitative information of H requires very complicated calibration and configuration of the instrument. Therefore, the melting extraction method by using the G8 Galileo ON/H analyzer came in handy to obtain quantitative information about the hydrogen content in the new phases. ATR-FTIR technique was applied to exclude the influence of any organic contaminants on the aforementioned measurements.

Finally, AFM and SKPFM measurements were conducted to characterize the surface topography and work function of new phases as well as the H-charged Ni surface.

3.4 Results

3.4.1 Phase crystallography and distribution

Fig. 6 compares XRD patterns obtained from an as-received Ni foil, a foil that had been charged for 5 hours and only dried before characterization, and one that had been charged for the same time (5 hours) and ultrasonicated before characterization. The 2θ range, 12° - 41° , was selected to exclude Ni reflections, which have a much higher intensity than reflections from charging-induced surface phases. The as-received Ni sample shows no peaks within the selected 2θ range, as expected for pure Ni. The H charged sample has several clear new peaks, consistent with the presence of surface phases with crystal structures distinct from that of Ni. These peaks lie in a lower 2θ range than ones reported in previous studies on cathodically charged Ni and attributed to hydrides[1, 34]. Finally, the H charged and ultrasonicated samples do not exhibit any of the aforementioned new peaks, indicating that the new phases formed during charging are easily removed by ultrasonication.

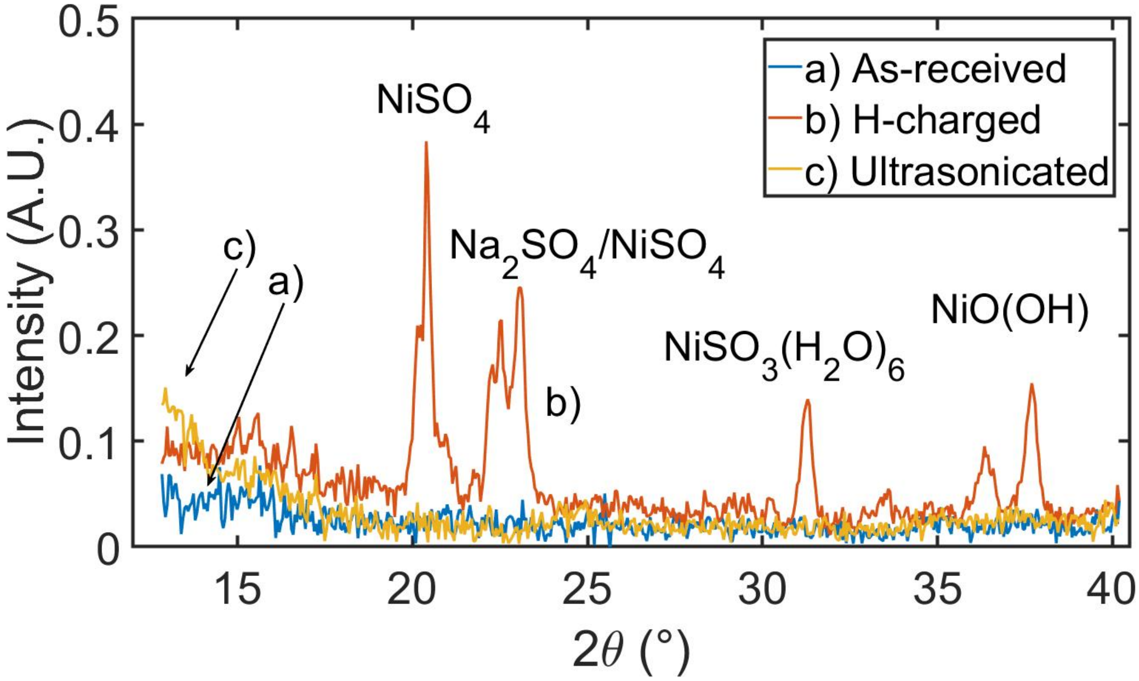

Figure 6: Comparison of XRD patterns from as-received samples, H charged samples with no ultrasonication, and samples ultrasonicated after H charging.

EBSD is used to determine how the charging-induced phases are distributed on sample surfaces. Fig. 7 presents EBSD images of representative areas of three samples: one as-received, one charged, and another charged and ultrasonicated. To perform EBSD analysis, the as-received foil had to be polished to ~5nm surface roughness. Regions that were successfully indexed as pure face-centered-cubic (FCC) Ni are colored by inverse pole figure (IPF) Z-coloring. The colormap in Fig 7.d) shows the relationship between color and the Miller index of free surface facets. As illustrated in Fig. 7.a), this foil is polycrystalline Ni with an average grain size of ~20 ± 1 μm, determined using the average grain intercept method[35].

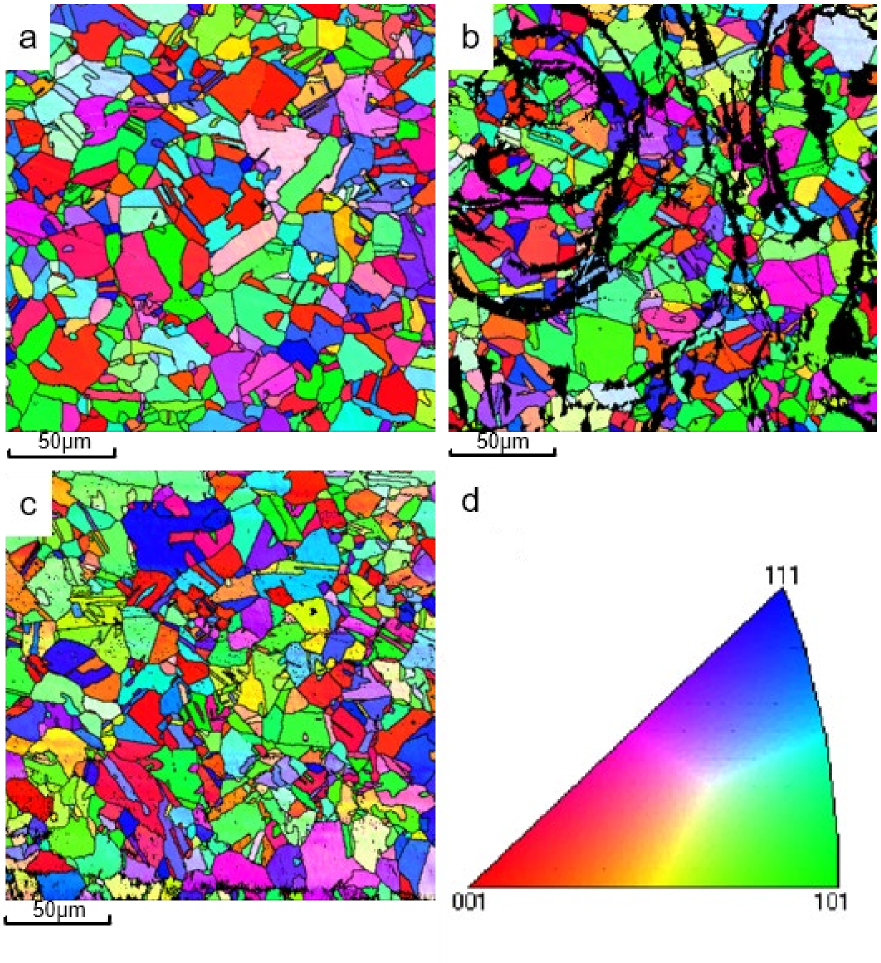

Figure 7: EBSD analysis of a) as-received Ni foil after polishing, b) H-charged and dried Ni foil and c) H-charged and ultrasonicated Ni foil. d) Correspondence between colors in a), b), and c) and Miller indices of free surface facets.

Fig. 7.c) shows the Ni surface after 18 hours of charging and subsequent ultrasonication. This sample presents a clean, polycrystalline Ni surface, comparable to the surface of the as-received foil shown in Fig. 7.a). In particular, Fig. 7.c) contains no regions that cannot be indexed as pure FCC Ni. This finding reinforces our conclusion that ultrasonication removes the surface phases that are formed during cathodic charging. The

average grain size in Fig. 7.c) is also 20 ± 1 μm, indicating that charging and ultrasonication do not affect the microstructure of the Ni foil.

To gain further insight into the structure of the charging-induced surface phases, the TOPAS[36] software was used to index the new XRD peaks in Fig. 6. The peak at 20.4° has been indexed to $NiSO_4$ with orthorhombic structure and Cmcm space group while the grouping of peaks around 22.8° has been indexed to a mixture of $NiSO_4$ and Na_2SO_4, the former with orthorhombic structure and Cmcm space group and the latter with orthorhombic structure and Fddd space group. The peak at 31.3° has been indexed to $NiSO_3(H_2O)_6$ with trigonal structure and R3 space group and the two peaks at 36.4° and 37.6° have been indexed to NiO(OH) with trigonal structure and P3m1 space group. This indexing of XRD peaks should be treated with caution as each of the aforementioned compounds also predicts peaks that were not observed in XRD. Furthermore, XRD is sensitive to crystal structure but not to composition. As a consequence of the indexing data, we may conclude that the surface phases are a combination of hydroxides, sulfates, and other chemicals, rather than a single crystallographic type.

Fig. 8 shows how the intensity of the distinct peaks identified in Fig. 6 changes as a function of charging time. For each charging period displayed in figure 8, separate Ni samples were charged and tested independently. Peak intensities for all new phases rose over the first 5 hours of charging, then declined for the next 5 to 10 hours before stabilizing with more charging time. After around 10 hours of charging, it appears that these surface phases have matured into a mature, nearly steady state.

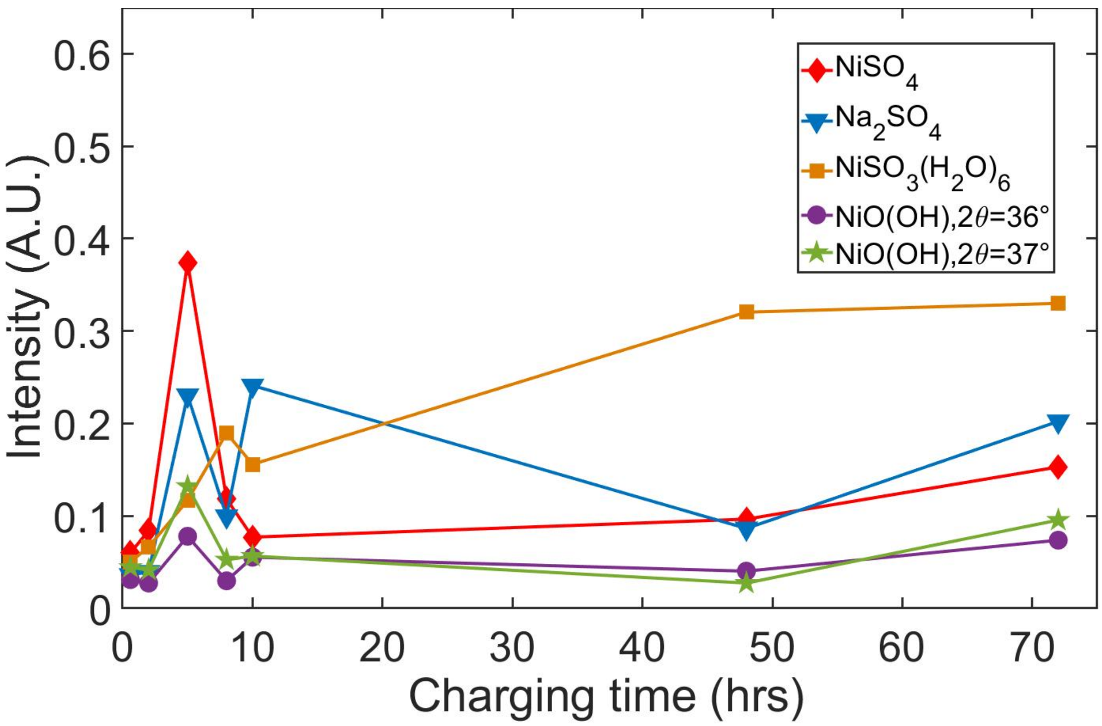

Figure 8: XRD peak intensity of charge-induced phases vs. charging time. The trendline labels correspond to the peak labels shown in Fig. 6.

Finally, XRD measurements on the surface of Ni foils that had been charged for 20 hours and subsequently left to age in the air for up to 48 hours were performed. Fig. 9 plots XRD peak intensities of peaks corresponding to all charge-induced phases as a function of aging time. Intensities of the peaks related to $NiSO_4$, Na_2SO_4, and NiO(OH) remain stable in air at all times. Meanwhile, the peak intensity of $NiSO_3(H_2O)_6$ diminishes more than 80% within the first 5 hrs of exposure to the air environment and then remains stable. Therefore, it appears that the charging-induced phases are long-lived and may be thermodynamically stable in air. The 80% decrease in intensity of the $NiSO_3(H_2O)_6$ peak suggests that the thermodynamic equilibrium state in the air of $NiSO_3(H_2O)_6$ may differ substantially from its driven steady-state during electrochemical charging.

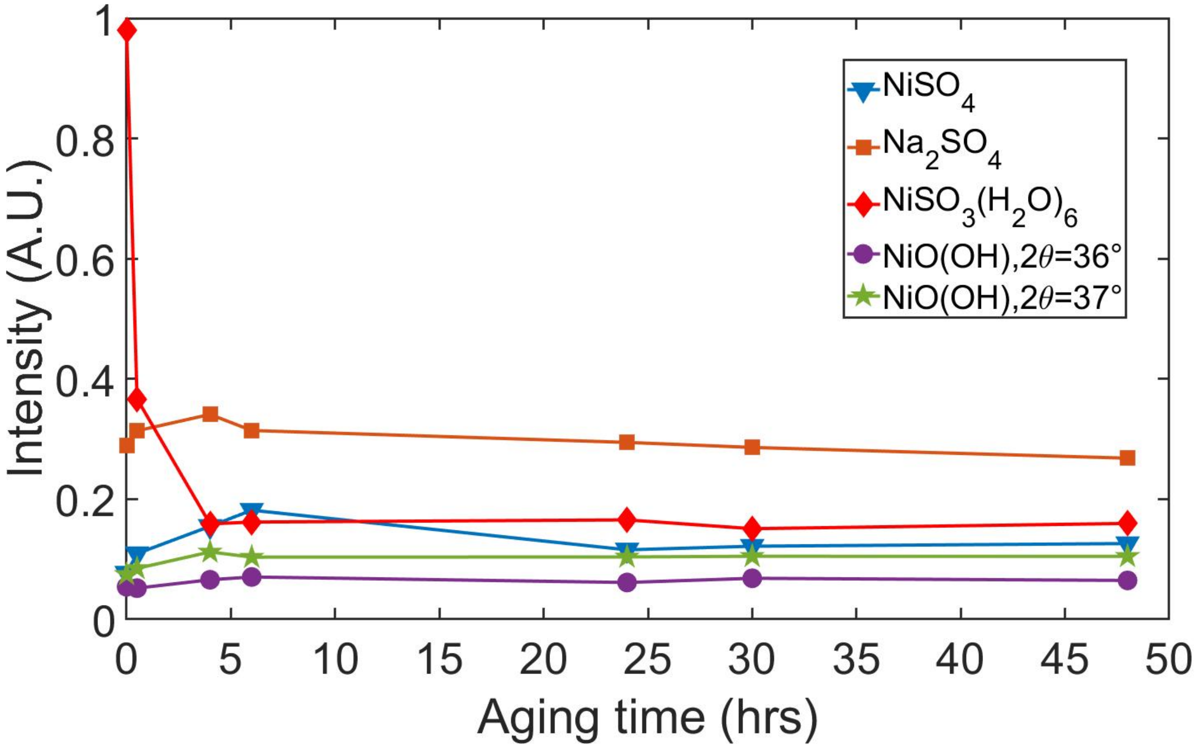

Figure 9: XRD peak intensity of charge-induced phases vs. aging time. The trendline labels correspond to the peak labels shown in Fig. 6.

3.4.2 Phase composition

Several complementary techniques were used to characterize the composition of the newly formed surface phases. Fig. 10 shows EDS scans of the surface of an as-received Ni specimen. As expected, the sample consists primarily of Ni, albeit with some evidence of uniformly distributed S and O surface impurities. Fig. 11 shows a corresponding EDS scan after 18 hours of cathodic charging and without ultrasonication. Surface O and S in this sample are clearly concentrated into elongated filaments ~5 µm in width. These filaments also appear to be slightly depleted of Ni, compared to the surrounding Ni surface.

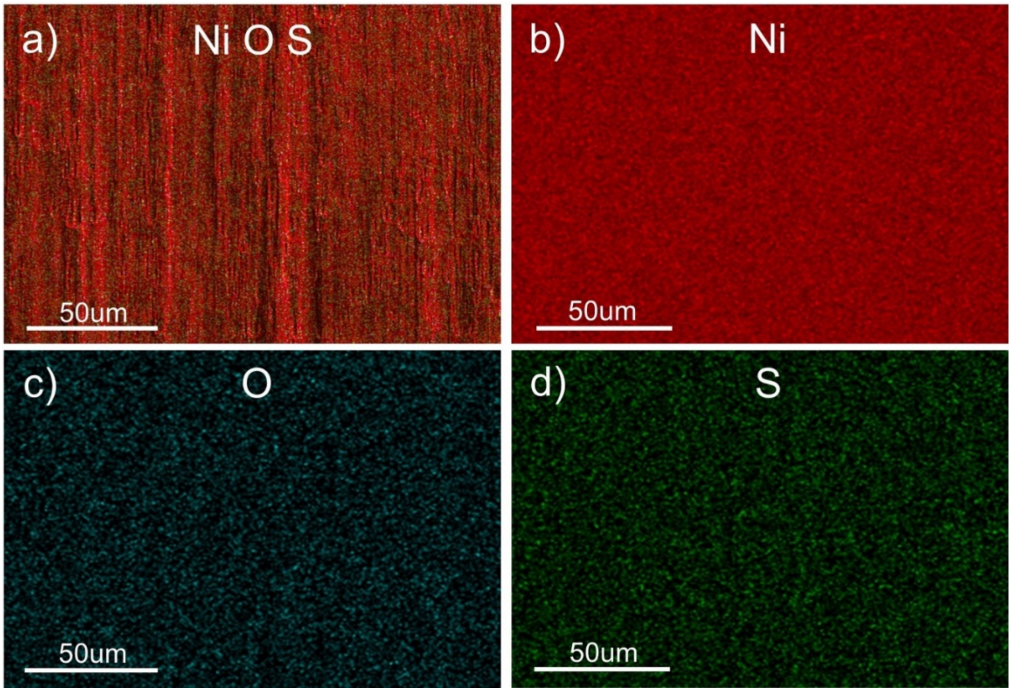

Figure 10: EDS mapping of an as-received Ni sample.

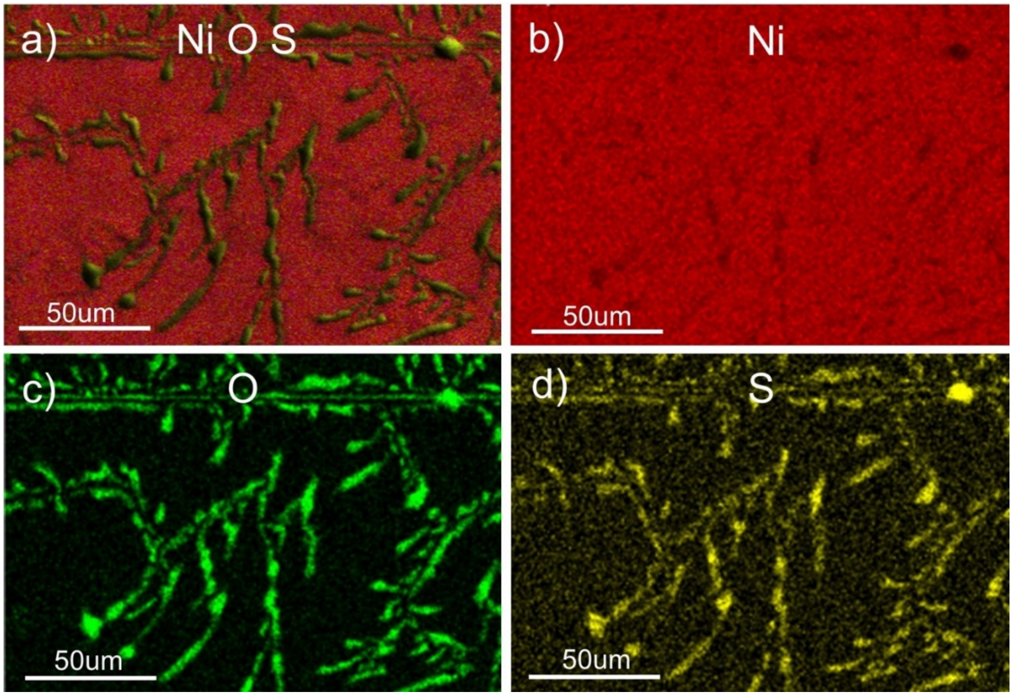

Figure 11: EDS mapping of a Ni sample after 18 hours of charging and no ultrasonication.

EDS scans of samples that had been cathodically charged and ultrasonicated (not shown) do not exhibit any of the S- and O-rich filaments shown in Fig. 11. Indeed, the elemental distribution on the surfaces of ultrasonicated samples is comparable to that of the as-received surface shown in Fig. 10, aside from low quantities of isolated S and O impurities uniformly distributed on the surface. Thus, based on their morphological similarity to the black regions in Fig. 7.b) and given their removal from the surface by ultrasonication, the S- and O-rich filaments can be identified in Fig. 11 as the charging-induced surface phases introduced in the previous section.

The signal detected by EDS originates from an approximately 1μm-thick layer on the sample surface. Meanwhile, as will be shown in section 3. c), the charging-induced surface phases are only about 100nm thick. Thus, while Fig. 11. b) shows a Ni signal on the surface area occupied by these phases, it is not clear whether any part of it originates from the phases themselves or whether all of it arises from the pure Ni metal underneath the phases. Consequently, EDS cannot determine unambiguously whether the charging-induced phases contain Ni, in addition to S and O.

SIMS measurements were carried out to confirm the presence of Ni in the charging-induced surface phases. As explained in the previous experimental section, the custom-built SIMS instrument used probes within ~5nm of the sample surface, filters out the background of Ni^+ ions originating from bare Ni surfaces, and collects mass spectra of ejecta created by impacts of individual 50 keV C_{60}^{2+} particles. Thus, this tool allows us to characterize the Ni content of the charging-induced phases unambiguously.

A representative example of the SIMS negative ion spectra is shown in Figure 12. Of particular note are the peaks due to S_2^-, SO_2^-, NiS^-, NiO_2^-, $NiSO_4OH^-$. A sequence of ~10 M impacts (at the rate of 1000 impacts/s) amounts to probing 10 M emission areas each of 10^2 nm^2. The individual spectra reveal co-emitted ions, i.e. It enables the identification of impacts that resulted in the emission of S or O-bearing ions and correlated species. These individual spectra may be analyzed to reveal correlations in the emission of pairs of species, A and B. The analysis is carried out by computing homogeneity coefficients, $H_{A,B}$, following Eller *et al.* [37]:

$$H_{A,B} = \frac{Y_{A,B}}{Y_A}. \qquad (1)$$

Here, Y_A is the total yield of A, defined as the number of counts of A in the complete spectrum divided by the total number of impacts, N, while $Y_{A,B}$ is the coincidental yield. To compute $Y_{A,B}$, the N_B impacts that resulted in the emission of at least one B cluster are found. The total number of A clusters emitted during just these N_B impacts is then found and divided by N_B. If there is no correlation in the emission of species A and B, then $H_{A,B} \approx 1$. If A and B tend to be co-emitted during the same impacts, then $H_{A,B} > 1$. Finally, $H_{A,B} < 1$ indicates anti-correlated emission: emission of A occurs preferentially during impacts that do not involve emission of B. Note that $H_{A,B} \neq H_{B,A}$.

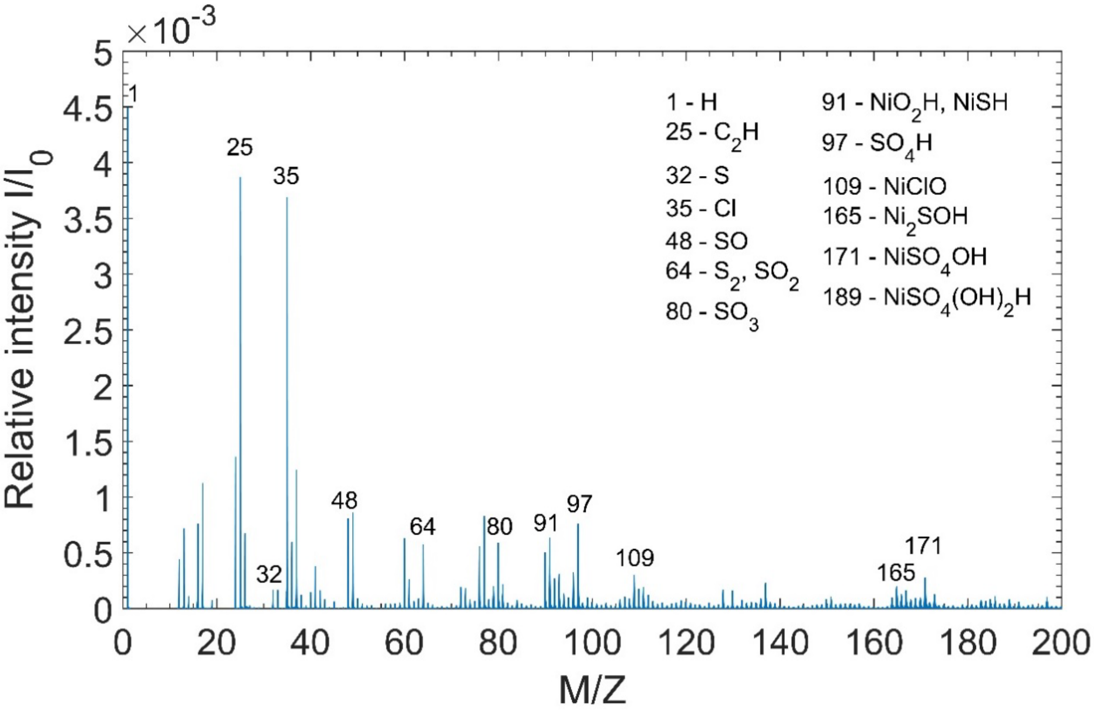

Figure 12: Total mass spectrum of an H-charged sample obtained using SIMS.

Fig. 13 presents homogeneity coefficients computed for pairs of the most prominent peaks in the SIMS emission spectrum in Fig. 12. Columns represent the measured ion (corresponding to A in equation 1) while rows represent ions used for impact selection (corresponding to B in equation 1). The table shows that S-bearing species, such as S, S_2, SO, SO_2, SO_3, and SO_4H, tend to be co-emitted along with Ni-bearing species, such as Ni_2SOH, NiO_2H, NiSH, NiS, and NiO_2, as evidenced by the fact that homogeneity coefficients computed for pairs of these species are greater than unity. We conclude that S- and Ni-bearing compounds tend to be co-located on the surface, likely within the charging-induced surface phases. Fig. 13 also shows that all homogeneity coefficients involving H, C_2H, and Cl are near unity, indicating that these species are uniformly distributed across the surface, with no correlation to the location of other species.

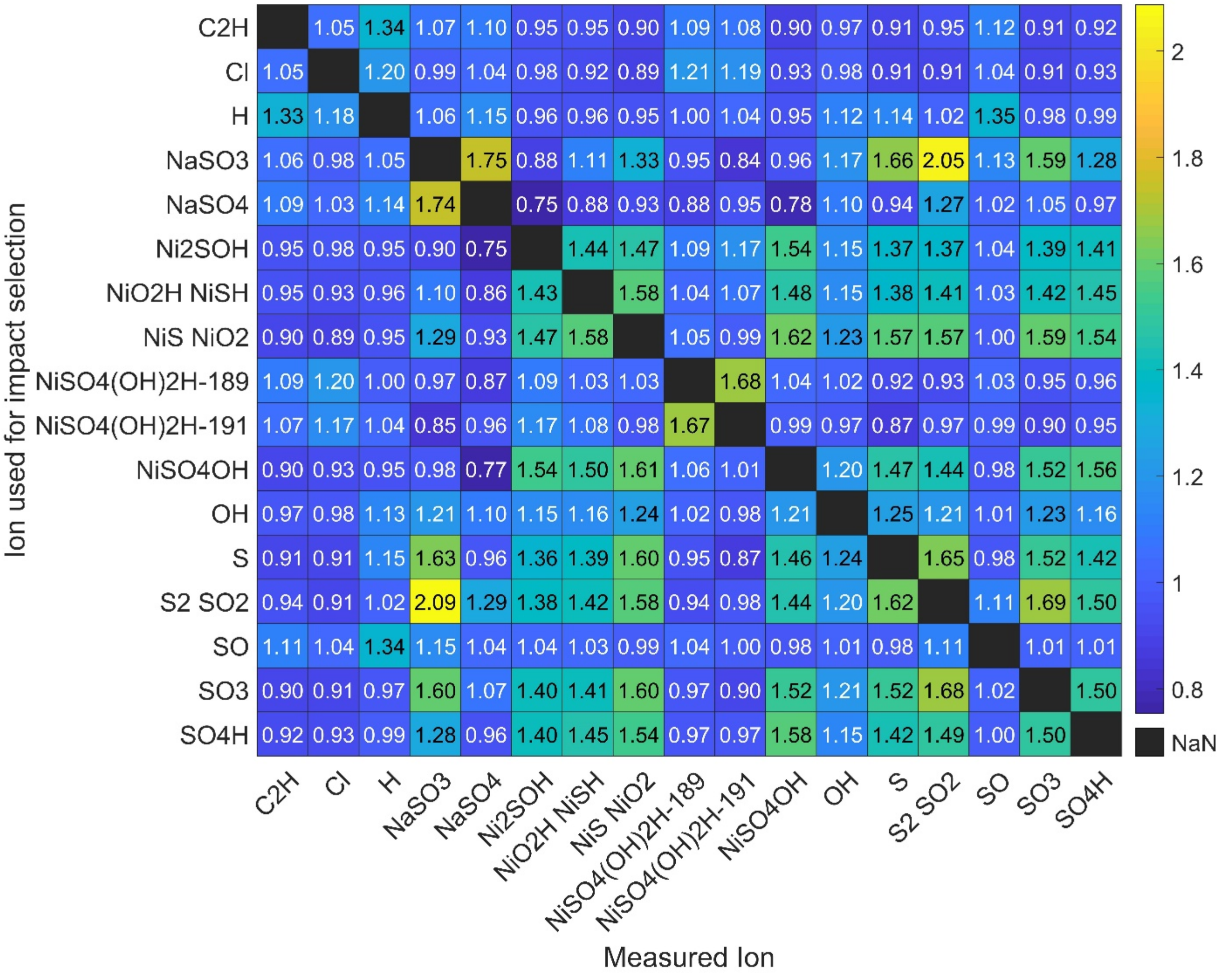

	C2H	Cl	H	NaSO3	NaSO4	Ni2SOH	NiO2H NiSH	NiS NiO2	NiSO4(OH)2H-189	NiSO4(OH)2H-191	NiSO4OH	OH	S	S2 SO2	SO	SO3	SO4H
C2H		1.05	1.34	1.07	1.10	0.95	0.95	0.90	1.09	1.08	0.90	0.97	0.91	0.95	1.12	0.91	0.92
Cl	1.05		1.20	0.99	1.04	0.98	0.92	0.89	1.21	1.19	0.93	0.98	0.91	0.91	1.04	0.91	0.93
H	1.33	1.18		1.06	1.15	0.96	0.96	0.95	1.00	1.04	0.95	1.12	1.14	1.02	1.35	0.98	0.99
NaSO3	1.06	0.98	1.05		1.75	0.88	1.11	1.33	0.95	0.84	0.96	1.17	1.66	2.05	1.13	1.59	1.28
NaSO4	1.09	1.03	1.14	1.74		0.75	0.88	0.93	0.88	0.95	0.78	1.10	0.94	1.27	1.02	1.05	0.97
Ni2SOH	0.95	0.98	0.95	0.90	0.75		1.44	1.47	1.09	1.17	1.54	1.15	1.37	1.37	1.04	1.39	1.41
NiO2H NiSH	0.95	0.93	0.96	1.10	0.86	1.43		1.58	1.04	1.07	1.48	1.15	1.38	1.41	1.03	1.42	1.45
NiS NiO2	0.90	0.89	0.95	1.29	0.93	1.47	1.58		1.05	0.99	1.62	1.23	1.57	1.57	1.00	1.59	1.54
NiSO4(OH)2H-189	1.09	1.20	1.00	0.97	0.87	1.09	1.03	1.03		1.68	1.04	1.02	0.92	0.93	1.03	0.95	0.96
NiSO4(OH)2H-191	1.07	1.17	1.04	0.85	0.96	1.17	1.08	0.98	1.67		0.99	0.97	0.87	0.97	0.99	0.90	0.95
NiSO4OH	0.90	0.93	0.95	0.98	0.77	1.54	1.50	1.61	1.06	1.01		1.20	1.47	1.44	0.98	1.52	1.56
OH	0.97	0.98	1.13	1.21	1.10	1.15	1.16	1.24	1.02	0.98	1.21		1.25	1.21	1.01	1.23	1.16
S	0.91	0.91	1.15	1.63	0.96	1.36	1.39	1.60	0.95	0.87	1.46	1.24		1.65	0.98	1.52	1.42
S2 SO2	0.94	0.91	1.02	2.09	1.29	1.38	1.42	1.58	0.94	0.98	1.44	1.20	1.62		1.11	1.69	1.50
SO	1.11	1.04	1.34	1.15	1.04	1.04	1.03	0.99	1.04	1.00	0.98	1.01	0.98	1.11		1.01	1.01
SO3	0.90	0.91	0.97	1.60	1.07	1.40	1.41	1.60	0.97	0.90	1.52	1.21	1.52	1.68	1.02		1.50
SO4H	0.92	0.93	0.99	1.28	0.96	1.40	1.45	1.54	0.97	0.97	1.58	1.15	1.42	1.49	1.00	1.50	

Figure 13: Homogeneity coefficients computed for pairs of prominent peaks in the SIMS spectrum of cathodically charged Ni.

EDS is not sensitive to H while SIMS requires calibration to return quantitative estimates of H content. Therefore, to estimate the H content of the charging-induced surface phases, melt extraction was used to determine and compare the H content of samples that had been ultrasonicated to that of samples that had been charged for the same time, but not ultrasonicated. Figure 14 shows the total H content of both sample types as a function of charging time. In both cases, the H content increases monotonically with charging time, consistent with continuous uptake of H into the Ni foils during charging[38, 39]. Moreover, the H content of ultrasonicated samples is consistently lower than that of the as-charged samples. The difference in H content between these two sample types is ascribed to the surface phases.

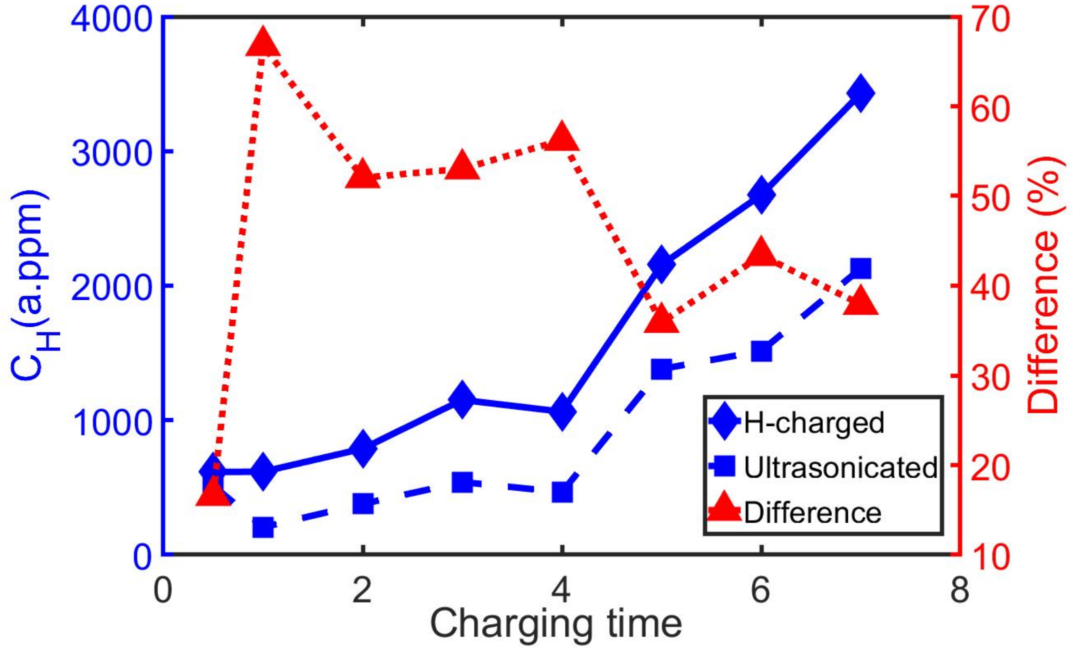

Figure 14: H content vs. charging time of as-charged Ni samples (solid blue line) and samples ultrasonicated after charging (dashed blue line). The % difference between the blue lines is shown with the red dashed line.

To estimate H concentration in the surface phases, the difference in the H content of the as-charged and ultrasonicated samples, ΔN_H, is computed and divided this quantity by the estimated total volume of the surface phases, V_s. The % difference in H content is plotted as a function of charging time in Fig. 14. Consistent with the rapid growth of the surface phases deduced from XRD (see Fig. 6), this difference increases rapidly within the first hour of charging. Subsequently, it stabilizes at around 5 hrs with a slight tendency to decrease with continued charge time.

To find V_s, multiplied by the surface area of the charging-induced phases—estimated in section 3.1 to be ~30% of the total sample surface area—by their thickness. As will be shown in section 3.3, these phases have a thickness of approximately 200 nm. Thus, $V_s \approx 2.7 \times 10^4\ \mu m^3$ giving an inferred H concentration of approximately 22 H atoms/nm^3. This H concentration is comparable to that in nickel sulfate hydrate (NiH_2SO_5, 23 H atoms/nm^3), less than that in nickel sulfite hexahydrate ($NiSO_3(H_2O)_6$, 60 H atoms/nm^3), and greater than that in nickel oxide hydroxide ($NiO(OH)$, 7 H atoms/nm^3).

Finally, neither EDS nor SIMS gave evidence of any significant surface contamination with C or C-bearing substances. To further support this finding, ATR-FTIR measurements were carried out on as-received and as-charged Ni foils. Organic contaminants are expected to present distinct peaks in infra-red absorbance spectra measured by this technique. However, as shown in Fig. 15, there are no major differences in the spectra of the investigated samples for wavelengths between 600 cm^{-1} and 4000 cm^{-1}.

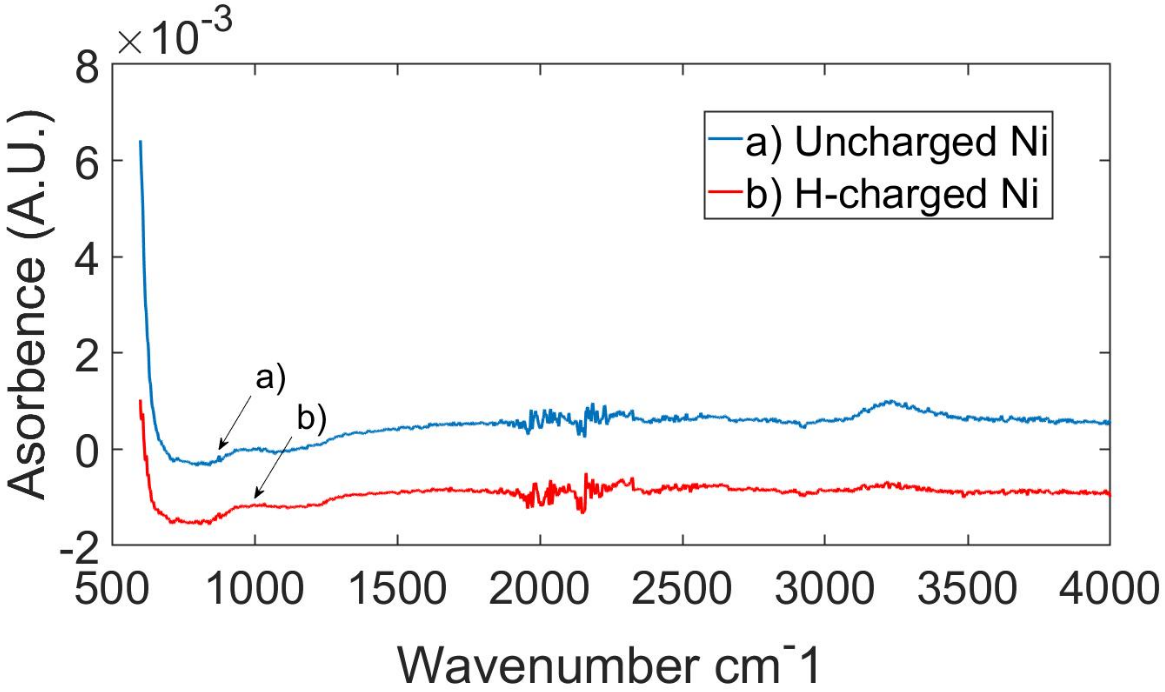

Figure 15: ATR-FTIR spectrum of as-received Ni sample and H charged Ni sample.

The small peaks near 2100 cm^{-1} originate from the ATR diamond crystal, which is part of the instrument. The weak and broad absorption peak around 3200 cm^{-1} could not be attributed to any specific contaminant. It can be concluded that the charging-induced surface phases are not organic contaminants.

3.4.3 Surface topography and potential

Figure 16 shows the surface elevation and surface potential (electron work function) of as-received and as-charged Ni samples measured by AFM and SKPFM. The work function is defined as the difference in potential between the sample surface and the detector tip. Therefore, the higher the value shown in the figure, the lower the surface potential (i.e., the more cathodic the surface). The as-received foil exhibits variations in surface topography reminiscent of surface faceting along crystallographic planes[40].

However, the surface work function of this foil shown in Fig 16. b) is nearly uniform, with no apparent influence of topography on work function. By contrast, the surface of the as-charged sample exhibits elongated islands protruding by ~200 nm over the surrounding area. These islands are shown in Fig 16.d) also exhibit a 120mV higher surface potential from the pure Ni substrate, meaning that they are cathodic with respect to the surrounding material.

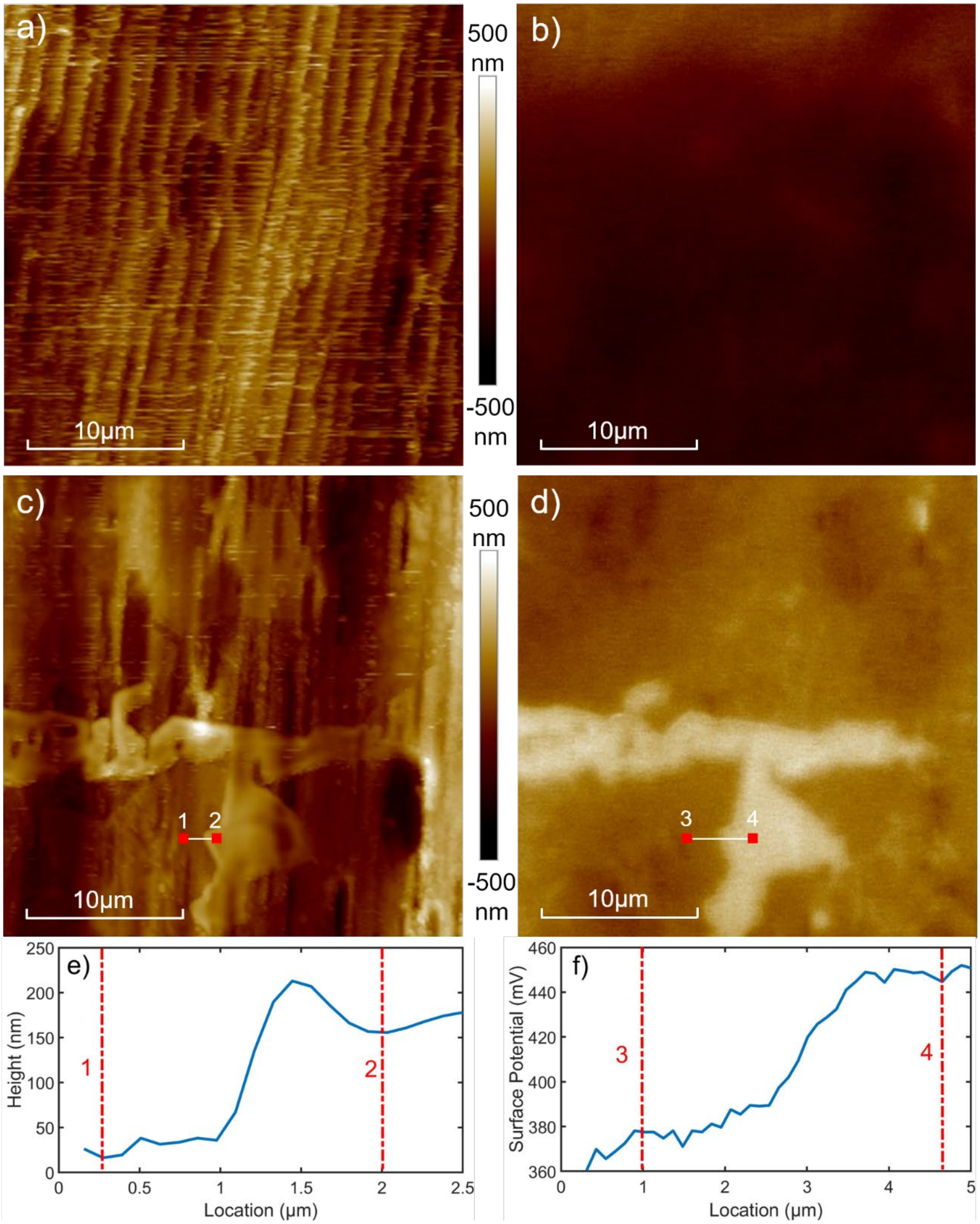

Figure 16: a) AFM and b) KPFM measurements on as-received Ni sample. c) AFM and d) KPFM measurements H-charged Ni sample. e) Height profile for line scan 1-2 shown in c). f) Surface potential profile for line scan 3-4 shown in d).

Samples that had been ultrasonicated after charging (not shown) do not exhibit the distinctive topographical features shown in Fig. 16. Moreover, their work functions are nearly uniform, as in the case of the as-received foils. Nevertheless, the ultrasonicated surfaces have an overall 100mV higher average surface potential than the uncharged Ni even after all the surface phases have been removed. This difference may be attributed to H uptake into the Ni matrix and the consequent elastic expansion[41]. Given their removal by ultrasonication, the aforementioned islands were identified to be the charging-induced surface phases, which the thickness was concluded to be ~200 nm and cathodically polarized by about 120mV with respect to the surrounding Ni surface.

3.4.4 Evolution of surface coverage

To study the time-variation of the coverage of the sample surface by the phases reported here, we carried out a series of EDS measurements on Ni samples after different charging times and without ultrasonication. Surface coverage for each was determined through analysis of EDS maps of oxygen content using the ImageJ software[42]. Fig. 17 shows the surface coverage as a function of charging time. The surface coverage increases in the first 12 hours, achieving ~30% coverage. Subsequently, the coverage reaches a time-invariant value and no longer increases with continued charging. These findings are consistent with the XRD results reported in Fig. 6. The surface phases maintain a filamentary shape throughout the charging process.

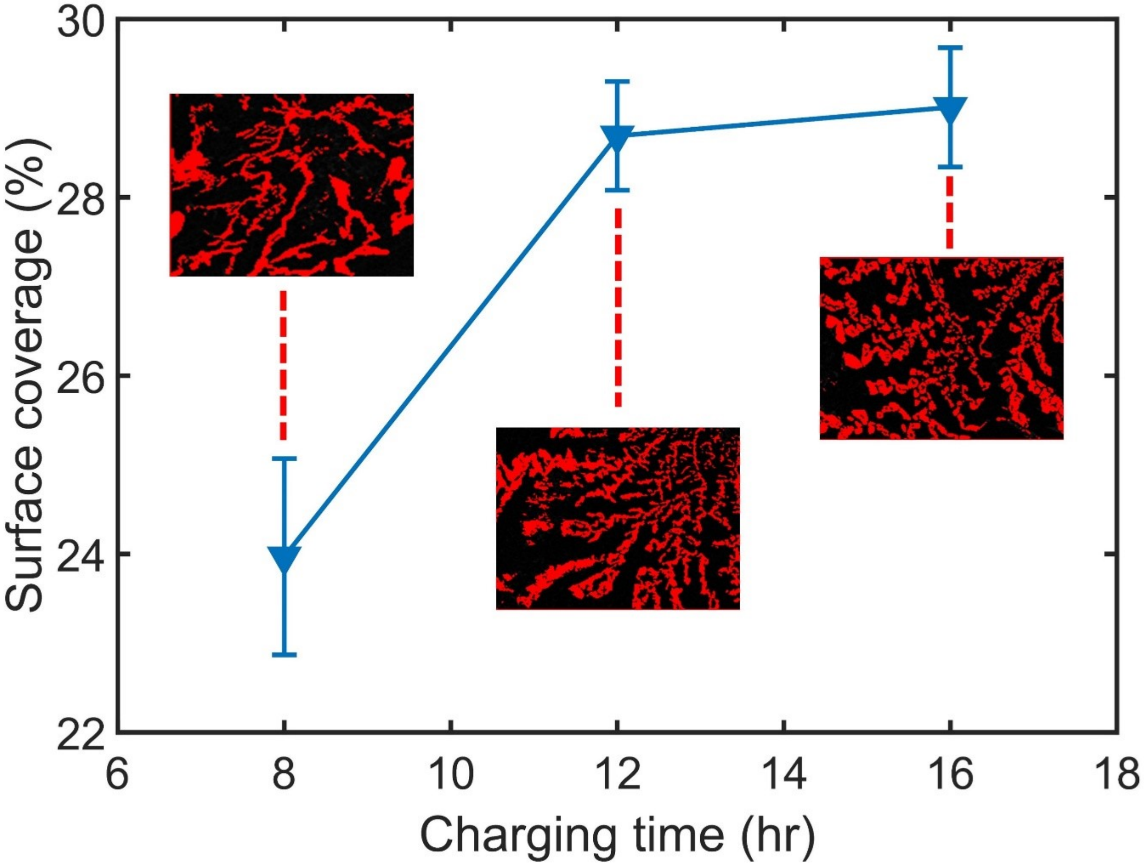

Figure 17: Surface coverage as a function of charging time.

The nature of the time-invariant state reached after 12 hours is further elucidated by ICP-MS measurements of electrolyte Ni content as a function of time, shown in Fig. 18. Unlike surface coverage, the Ni concentration in the electrolyte increases monotonically with time, without reaching a time-invariant state. This result indicates that Ni is continually dissolving from the sample and suggests that the time-invariant surface coverage illustrated in Fig. 17 is actually a dynamic steady state achieved when the rate of formation and dissolution of the surface phases balance.

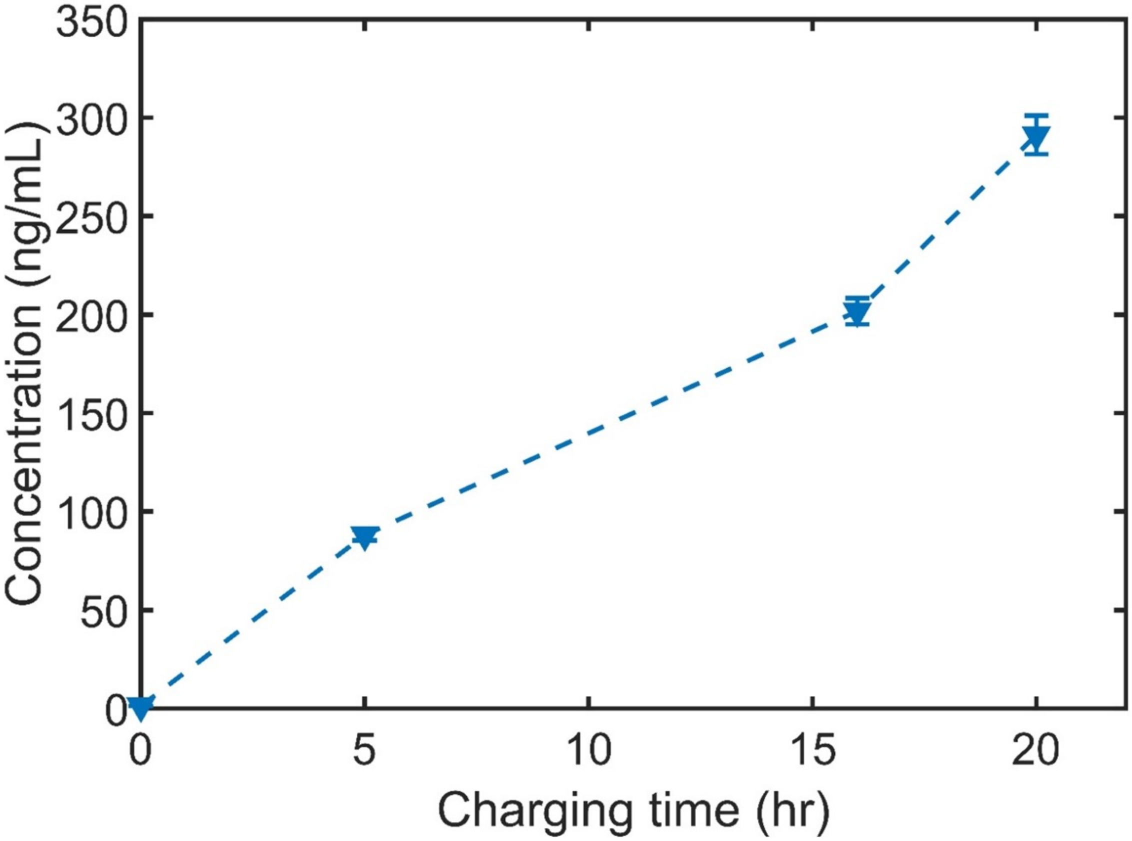

Figure 18: Ni concentration in the electrolyte as a function of charging time.

Assuming that all the dissolved Ni originates from the surface phases, the data in Fig. 17 allow us to infer the rate of phase formation needed to balance the measured Ni loss. Considering that the total electrolyte volume is 1L and the total sample surface area is 6cm^2, we find that the surface coverage must grow at a rate of ~3.3% per hour to balance the observed Ni loss under steady-state conditions. This calculated rate of formation is in good agreement with the initial growth in surface coverage shown in Fig. 17 (~24%/8hours $\approx$ 3%/hour). This finding supports the conclusion that the steady-state coverage represents balancing rates of phase formation and dissolution, both of which proceed continually throughout charging.

3.5 Discussion

In this work, we demonstrate the formation of distinct surface phases on cathodically charged Ni foils. Our analysis shows that these phases are composed of Ni, O, S, and H. After reaching steady-state during cathodic charging at a 400mV overpotential, they are about 150nm thick and cover approximately 30% of the surface area. Ultrasonication removes the surface phases, indicating that they are not strongly bound to the Ni surface and may be mechanically fragile themselves. However, they persist in the air. Finally, the surface electronic potential of these phases is cathodic with respect to the surrounding Ni by about 70 mV.

Based on their compositions and XRD spectra, the charging-induced surface phases likely include Ni hydroxides, sulfates, and oxyacid salts. With the exception of Ni oxyacid salt ($NiSO_3(H_2O)_6$) [43], these compounds are thermodynamically stable in the air [44, 45] consistent with the XRD data in Fig. 6. However, when placed in aqueous electrolytes, they are only stable at high pH or under anodic polarization [44, 45] They are thermodynamically unstable under cathodic polarization and in highly acidic electrolytes. Thus, their occurrence in our experiments is unexpected and requires explanation.

We propose a mechanism for the formation of the reported surface phases that recognizes their inherent thermodynamic instability under cathodic charging at low pH. Indeed, the electrolyte composition data in Fig. 18 suggests that the observed surface phases are continually dissolving into the electrolyte, as would be expected for thermodynamically unstable compounds. The variations in open circuit potential (OCP) shown in Fig. 2 also suggest the dissolution of these phases into the electrolyte. The rapid drop in OCP highlighted by the solid red box in Fig.2 indicates that the sample initially possesses a thin, passivating film—likely a Ni oxide or hydroxide [44, 45] that dissolves upon immersion in the electrolyte. The gradual rise in OCP after prolonged cathodic charging is consistent with the re-passivation of the surface by the surface phases reported here. However, every time the applied potential is removed, the OCP is once again observed to drop, as illustrated by the orange dotted box in Fig. 2.

In view of the thermodynamic instability of the observed surface phases and their continual dissolution into the electrolyte, we propose that they form from the decomposition of other, even higher-energy phases, namely superstoichiometric Ni hydrides. Previous studies have proposed that Ni hydrides may form under cathodic charging [16, 46-48]. However, given that we do not observe any diffraction peaks attributable to them, the proposed hydrides likely form as surface films that are too thin to be detected by XRD. Indeed, we hypothesize that the sample surface area that appears to consist of bare Ni may be coated with a thin layer of superstoichiometric Ni hydride.

First-principles computational studies indicate that superstoichiometric NiH_x, with $x>1.25$, has higher energy than bare Ni (by up to 150 kJ/mol, in the case of NiH_3) [49]meaning that such hydrides are likely to undergo exothermic reactions, forming lower-energy products. Indeed, many metal hydrides, such as LiH, KH, NaH, as well as dihydrides, including MgH_2 and CaH_2, are reported to be highly reactive, including with water [50, 51]. Therefore, we propose that the surface phases reported here form *via* the reaction of NiH_x with the electrolyte. For example, its reaction with water yields $Ni(OH)_2$, which is one of the compounds identified in our study:

$$\boldsymbol{NiH_x + 2H_2O \rightarrow Ni(OH)_2 + \left(\tfrac{x}{2} + 1\right)H_2.} \qquad \text{(2)}$$

Figure 19 presents a schematic of how the reaction in Eqn. 2 may occur on the sample surface. Hydroxide ions from the electrolyte are preferentially transported to the NiH_x layer as it is anodic, relative to the surface phases reported here (as shown in Fig. 16). The reaction of these ions with the hydride yields $Ni(OH)_2$ and concurrently releases H_2 from the decomposition of the surface hydride as well as electrons from the oxidation of Ni into the Ni^{2+} valence. Hydronium ions from the electrolyte are preferentially transported to the surface phases, which are cathodic relative to the hydride layer. The electrons released from the oxidation of Ni are conducted through the Ni substrate, carrying the charge needed to neutralize hydronium at the surface phases and leading to the eventual evolution of H_2 from them, as well.

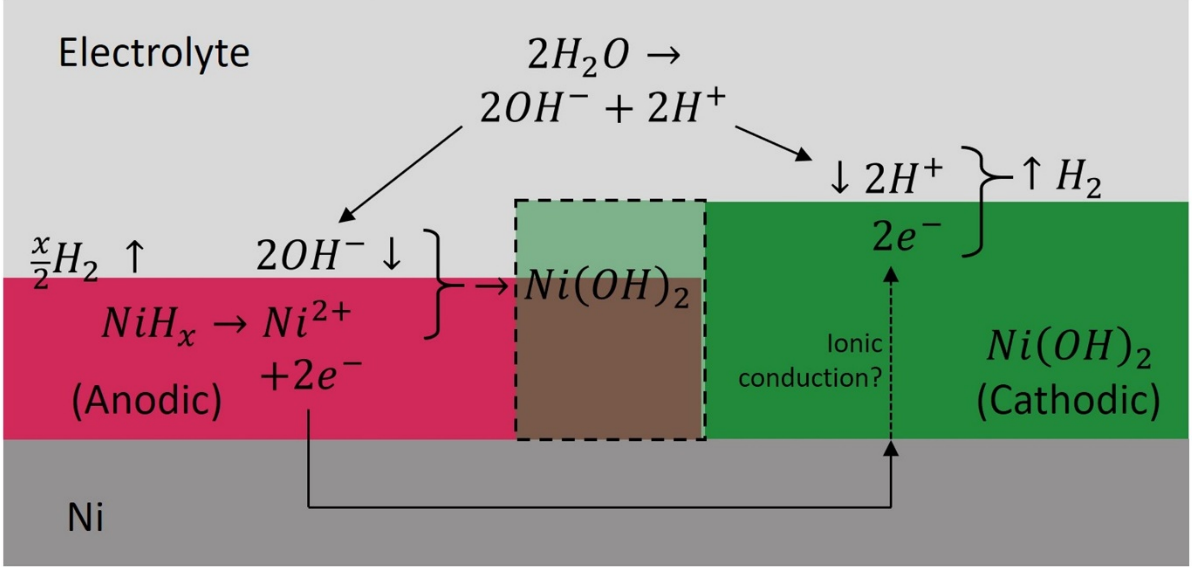

The proposed reaction does not involve any net change in charge. Therefore, in principle, it may occur under any externally applied polarization, both cathodic and anodic. However, as illustrated in Fig. 19, it generates local surface currents and therefore implies a non-uniform surface potential, which is consistent with our findings. The electrical resistivities of both the hydride (e.g., NiH [52] and product phases (e.g., $Ni(OH)_2$ [53] are substantially higher than that of Ni. Thus, we expect these currents to pass mostly beneath the immediate sample surface. This fact explains why the proposed reaction occurs preferentially in the vicinity of pre-existing cathodic locations, rather uniformly across the sample surface. Since the total resistance experienced by the electrons increases with the distance traveled, the most active sites are those close to the hydride/product phase interface.

Several previous studies informed our interpretation of the results presented here. Conway *et al.* [54] studied Raney Ni-Al electrodes under cathodic polarization in 10M NaOH at pH 14. They observed continuing evolution of H_2 even after cathodic charging ceased. They attributed this evolution to the decomposition of a surface hydride through a reaction with water. However, they did not determine whether any product phases remained on the surface. Similarly, Song *et al.* [19] studied Mg-based alloy AZ91 in 1N NaCl at pH 11 under both cathodic and anodic polarization. They proposed that the reaction of a surface hydride with water is responsible both for anodic H_2 evolution and cathodic Mg dissolution. Chen *et al.* [20] reached comparable conclusions in a study on AZ91 in 3.5 wt% NaCl solution at pH 7. Additional insight into hydride decomposition was provided by Williams *et al.* [21], who used the in situ scanning vibrating electrode technique (SVET) to characterize localized corrosion on unpolarized Mg in 5% wt NaCl electrolyte at pH 6.5. They observed a cathodic center of Mg hydroxide encircled by an anodic ring, possibly of Mg hydride. They argued that the anodic decomposition of Mg hydride occurs adjacent to the cathodic center as it is the least resistive location for the electron transfer.

Beyond purely electrochemical investigations, Binns *et al.* [55] studied cathodically polarized Mg-base ZEK100 alloy in 0.1 M NaOH at pH 13. They argued for the existence of MgH_2 based on XRD data and for $Mg(OH)_2$ based on SIMS. In their view, Mg hydrides are metastable and react with water to form $Mg(OH)_2$. They propose that this formation mechanism is responsible for the filiform morphology of the corrosion features they observed. Finally, Adhikari *et al.* [56] reported hydride formation on unpolarized pure Al in 1M NaOH solution at pH 14, based on SIMS and AFM characterization. Moreover, they observed nm-scale surface particles, which they suggest consist of Al hydride with Al hydroxide. They concluded that the emergence and dissolution of these particles are due to the decomposition of Al hydride into Al hydroxide and the subsequent dissolution of the latter. These foregoing studies suggest that the formation of surface hydrides and their subsequent decomposition via reactions with the electrolye may be common to many metals.

While Eqn. 2 leads to the formation of $Ni(OH)_2$, several of the surface phases identified in our study contain S. To ascertain the origin of the S, we estimate the total S content in the phases and compare it to the S impurity content in the as-received foil (see Table 1). The volume of surface phases has already been estimated in section 3.b) as $V_s =$

$(5.4 \pm 1.8) \times 10^{-5} cm^3$. Assuming a nominal surface phase composition of $NiSO_4$ and using the density (4g/cm^3) and molar mass (154.75g/mol) of $NiSO_4$, we estimate that the total S content of the surface phases is $(1.4 \pm 0.51) \times 10^{-6}$ mol. Meanwhile, based on the reported S impurity concentration in the as-received Ni foil (~3 w.ppm), each of our samples is initially expected to contain $(2.5 \pm 0.85) \times 10^{-8}$ mol of S.

Thus, the S content of the surface phases far exceeds the amount of S initially present in our samples. It is therefore likely that the S in the surface phases originates predominantly from the H_2SO_4 in the electrolyte. For example, instead of reacting with hydroxide ions, the hydride layer in Fig. 19 may react with SO_4^{2-} present in the electrolyte, resulting in the formation of $NiSO_4$, which is one of the surface phases identified in our study. It follows that the composition of surface phases formed under cathodic charging depends on the composition of the electrolyte.

While the proposed mechanism for the formation of Ni-O-H-S phases is consistent with the available data, it assumes the presence of a superstoichiometric NiH_x layer. If, as we expect, such a layer is too thin to detect by conventional techniques, then experimental confirmation of its presence would likely require neutron reflectometry (NR). NR is sensitive to hydrogen and capable of detecting Angstrom-thick surface layers [57]. Moreover, since the hypothesized NiH_x is expected to be thermodynamically highly unstable, its detection may have to be carried out *in situ* in an electrochemical cell: a challenging proposition, but not unprecedented [58]. Finally, the formation mechanism of the proposed NiH_x layer is also unknown. Under the cathodic charging conditions of our experiment, its emergence may be due to the high electric current being driven through the Ni cathode.

For example, since NiH has a much higher resistivity than Ni [59], the charge transfer reaction at the cathode may require partial ingress of H^+ ions into the Ni, giving rise to a near-surface H supersaturation.

As shown in EBSD and EDS, the new phases are aggregated into filamentary networks and occasionally exhibit dendritic-like morphologies. Several previous studies have reported similar surface phase morphologies and proposed a variety of mechanisms to explain them. Binns *et al* observed filiform corrosion products on magnesium and attributed them to the synergic effect of enhanced cathodic activity catalyzed by magnesium hydride and formation of corrosion-suppressing magnesium hydroxide [55]. Others suggest that filiform surface phase morphologies may be due to the underlying material microstructure [60, 61]. Filiform morphologies are also reminiscent of the "Brownian trees" often seen in studies on diffusion-limited aggregation [62], wherein atomic species execute a random walk until they attach to a pre-existing aggregate and are immobilized, e.g., in electrodeposition [63]. Our present study does not permit us to conclude which, if any, of these mechanisms is responsible for the distinctive surface phase morphologies observed on cathodically charged Ni. The question, therefore, awaits further investigation.

Much is already known about the Ni hydroxides, sulfates, and oxyacid salts, which are thought to be present in the surface phases reported here. For example, these compounds have resistivities of $2.60 \cdot 10^{-4}$ ($\Omega \cdot m$) to 10^6 ($\Omega \cdot m$) [64, 65], i.e., substantially higher than pure Ni ($6.99 \cdot 10^{-8}$ ($\Omega \cdot m$)). Density functional theory (DFT) calculations show that the elastic constants of these phases are generally lower than those of pure Ni by approximately a factor of two [66, 67]. They also have a lower Vickers hardness of 250-400MPa [68], compared to 700MPa for Ni[69]. Nevertheless, numerous follow-on studies may be conducted to elucidate their properties. For example, the hardness and elastic moduli of the phases relative to the Ni surface may be further investigated by peak force quantitative nanomechanical mapping (PFQNM): and AFM-based technique that maps these mechanical properties as a function of location on the sample surface.

Electrochemical impedance spectroscopy (EIS) may also be carried out to further characterize the interaction of these phases with aqueous electrolytes. The non-uniform distribution of the surface phases complicates the interpretation of such measurements, necessitating the use of specialized analysis methods, such as the constant-phase-element (CPE) model by Brug *et al.* [70], or localized EIS microelectrodes capable of probing the local impedance [71]. The outcome may be compared to the Mott-Schottky analysis for electrolyte/semiconductor junctions, providing insight into the electronic nature of the surface phases.

The formation of Ni surface phases during cathodic charging has potentially important technological consequences. Metal hydrides and hydroxides are thought to be responsible for the activity loss of Ni during electrochemical H charging [3, 4]. They are also thought to increase the electrode overpotential for the H evolution reaction (HER) [47]. The formation of surface phases may therefore be deleterious for the efficiency of electrolytic H production. However, it may be beneficial in cathodic protection as it may lead to a reduction of H uptake into the Ni and therefore a lower risk of H embrittlement. The surface phases may also act as barriers for H diffusion into Ni.

The differing potentials and electrical resistivities of the charging-induced phases and the surrounding surfaces give rise to the emergence of localized galvanic couples. This scenario may lead to the onset of localized corrosion, even on cathodically polarized Ni surfaces. We did not observe any localized corrosion in our experiments. However, Liu *et al.* report deep corrosion pits on pure Ni surfaces after cathodic charging at much higher current densities than were used in our study [15]. Surface phases may play a role in the initiation of such pits. For example, since $Ni(OH)_2$ is an ionic conductor [72], charge transfer across it may be mediated by Cl^- ions, which are known the play a role in pitting [73-75]. Such cathodic corrosion processes have yet to be investigated in detail.

Finally, charging-induced surface phases may have a role to play in crack propagation. Based on multi-scale simulations incorporating atomistic and discrete dislocation methods, Song and Curtin proposed that stress fields at crack tips promote the local formation of hydrides in Ni [76] and Fe [77]. These crack-tip phases then embrittle the material by suppressing the emission of dislocations from the crack tip. Moreover, they may be brittle themselves, as others have observed [1, 13, 78], leading to easier cleavage. Our study leads us to infer the presence of hydrides on cathodically charged Ni surfaces, potentially lending support to these hypotheses. Moreover, the arguments of Song and Curtin would appear also to hold if the crack tip phases were not hydrides, but rather more compositionally complex phases, such as the Ni-O-S-H compounds investigated here. It would therefore seem valuable to investigate whether such phases form within cracks, in addition to flat surfaces, and—if so—whether they affect crack propagation.

4. H UPTAKE OF NI UNDER CATHODIC CHARGING

4.1 Introduction

Findings from section 3 suggest the necessity of the existence of some surface hydride, as the precursor to the Ni-O-S-H surface phase formation. As such hydride phases usually have high energy and thus, thermodynamically unstable, they are not supposed to be observed easily via ex-situ, postmortem surface characterization. Additionally, the hydrogen of the surface hydride, due to it just having only one electron, the electron density is too weak that it can not emit X-rays that can be detected by conventional surface characterization such as X-ray diffraction. The hydrogen atoms in coupling with the much heavier metal can make things even worse as the strong Fourier truncation ripples can completely overshadow the rather weak electron density contrast from the hydrogen atom.

Therefore, there is not much option when it comes to detecting hydrogen atoms directly. One feasible way to observe atomic hydrogen is using atom probe tomography[79, 80] but it provides depth distribution profile rather than planar distribution. It also requires delicate sample preparation and the sample is extremely susceptible to volatile environments that it only works for ex-situ observation. The other way to directly detect hydrogen atoms is neutron reflectometry, which due to its isotopic sensitivity and ability to study covered interfaces (the interface between Ni and electrolyte in this case), is a mature and promising experimental technique for such investigation. It is also non-destructive and due to the high penetrability of the neutrons through various matter or media, it is also suitable and capable for in situ studies.

However, although we did try to conduct such investigation in the Lujan center at Los Alamos National Laboratory, it eventually did not work out due to several technical difficulties with the dissolution of deposited Ni thin film from the quartz substrate being the biggest issue.

Despite all these challenges for conducting direct measurement on the Ni surface under cathodic charging, there are some indirect ways to achieve the same goal. When a sample has been saturated with hydrogen, there is not any more net change of the adsorbed hydrogen atoms diffusing in or out from the sample. At this equilibrium state, the measured average hydrogen concentration, therefore, equals the equilibrium hydrogen concentration C_H as the hydrogen distribution in the sample interior is uniform everywhere. As a result, the surface hydrogen concentration or surface hydrogen coverage θ can be inferred based on C_H. This inspired the second main part of my research work, the hydrogen uptake of Ni under cathodic charging.

4.2 Charging experiments and electrochemical measurements conducted

The samples we conducted charging experiments on are the same as mentioned before. 50 μm thickness enables us to successfully charge the samples to an equilibrium state with hydrogen within 12 hours, which is critical as our concentration measurement is ex-situ that the saturation process requires several data points from the same numbers of individual charging and hydrogen concentration measurement. All charging experiments are conducted based on two parameters, t, charging time and η, overpotential. Charging time, t, ranging from 1 hr up to 24 hrs to ensure Ni is saturated with hydrogen.

Overpotential $\eta = U - U_0$. U is the applied potential between the working electrode and the reference electrode while U_0 is the open circuit potential (OCP) which depends on the choice of the reference electrode. However, we found that the open circuit potential (OCP) changes during the first 4-5 hours of charging (Fig. 2), which we believe is due to the change of surface condition[81, 82] during charging. Therefore, applied potential has to be adjusted regularly to keep overpotential constant.

Here we chose a single charging period to be 1 hour, after that power is cut off for 10 mins to let the open circuit potential rest and get stabilized. Then a new open circuit potential (OCP) is measured for the determination of the applied potential for the next charging period. The plot highlighted by red circles shows that open circuit potential (OCP) stabilizes asymptotically after power switch off for 10 mins, that is why we think e result 10 mins wait time will be enough to obtain an accurate OCP measurement.

EIS scan was also used to investigate the dynamics change of charging reaction as well as the diffusion process on the sample surface during charging. Results show that electrolyte resistance and double-layer capacitance have minimal change throughout the whole charging process, which means the aqueous environment and the interphase between electrolyte and sample are stable and consistent during charging. However, the EIS results should not be taken into consideration too seriously and draw a conclusive claim from that, simply due to the fact the surface phases introduced from section 3 has a non-uniform distribution which will also yield a capacitative response that may obscure the interpretation and results. The charge transfer resistance which is a measurement of the resistance for transferring electrons from the electrode to the hydrogen ions in the liquid phase decreases by about 30% in the first 5-hours of charging and stays almost the same after that. This means the surface of the sample went through a transient state in the first 4-5 hours and became fully polarized and stabilized after that.

To sum up, all the Ni samples were charged in the following ways:

- Different total applied potential: 400mV vs SCE, 500mV vs SCE, 600mV vs SCE, 700mV vs SCE. These charging experiments are conducted to see if H uptake content has a dependence on the total applied potential provided to the system.
- Different overpotential: 0mV; -250mV, -300mV, -400mV, -450mV, -500mV, -600mV. With the sample dimension introduced previously, charging under overpotential larger than -600mV will result in the onset of localized corrosion and current shot-off that will exceed the current limitation of the potentiostat and eventually interrupt the charging. Constant overpotentials were maintained thoroughly all the charging by using the periodic charging method introduced in the method chapter. The purpose is to see if there is a relationship between H uptake and overpotential.
- For each total applied potential and overpotential, a series of charging experiments were conducted with different charging times ranging from 1hr up to 24hrs. Time-resolved H content profile can be obtained and up to 24 hrs charging can make sure the Ni samples reach their equilibrium state of H uptake.

4.2 Hydrogen content measurement

We used the melt extraction method in the G8 Galileo ON/H analyzer from Bruker to measure the hydrogen concentration inside the nickel foil after hydrogen charging. The instrument has been calibrated using the standard sample from Alpha Resources before measurement to ensure accuracy.

After charging, the sample will be removed from the cell, detached from the glass tube and wire to be ready for cleaning. The sample will first be rinsed with DI water to remove residual electrolyte and other impurities and deposits formed at the surface of the sample during charging. Then the sample will be immersed into acetone for ultrasonication, which is to remove further deposits formed at the surface. After 3 mins of ultrasonication, the sample will be wiped dry and ready for hydrogen concentration measurement.

The melting extraction measurement for hydrogen concentration takes about 2 mins, coupled with the cleaning procedures which is around 5 mins; the sample will be outgassing for around 7 mins until the concentration is measured. This loss of hydrogen concentration has been compensated in our calculation which will be discussed later.

4.3 Results

4.3.1 H content profile without ultrasonication at constant potentials

We started with a series of charging experiments at different applied potentials (400, 500, 600, and 700 mV) for different time lengths up to 16 hours, and the concentration has been measured without surface cleaning, which is just rinsed with DI water. Fig 20 shows the plot of hydrogen concentration after various hours of charging at various applied potentials.

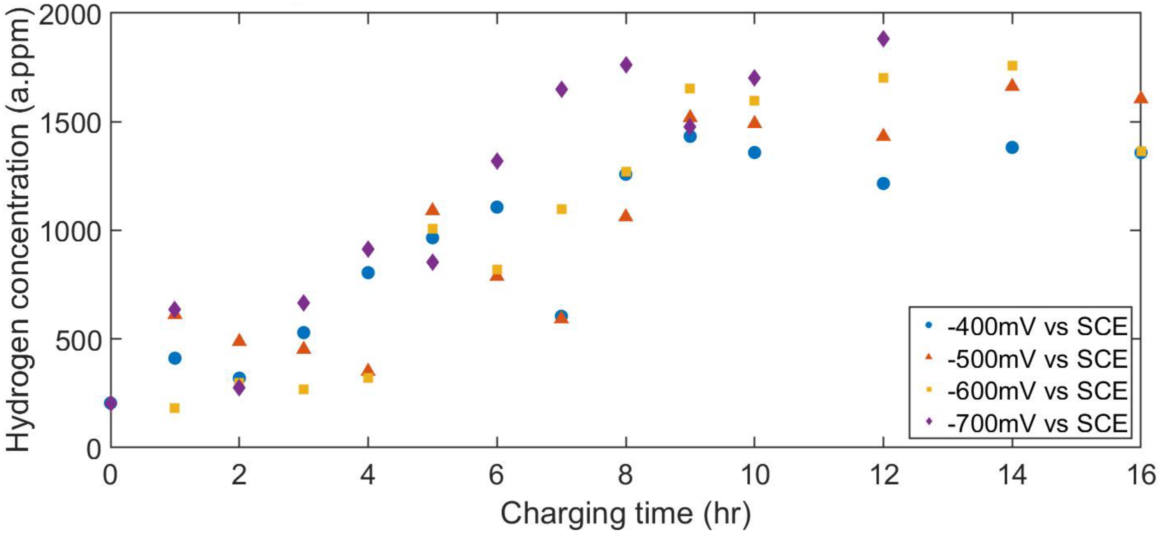

Figure 20: Plot of C_H vs charging time at different applied potential without surface cleaning.

C_H at t = 0 hr is the average concentration from the baseline measurements of 10 as-received nickel foils, which is 205 a.ppm. Even though all plots at different applied potential show a positive correlation between charging time and hydrogen concentration, the data are very scattered and there is no clear plateau which represents hydrogen inside the sample is saturated and achieves its equilibrium state. Given that the thickness of the sample is 50 um, T = 25℃ and using a hydrogen diffusion coefficient in nickel $D_0 = 6.87 \times 10^{-7} m^2/s$, activation energy $Q_0 = 40.52\text{kJ/mol}$ determined by Völkl and Alefeld[39, 83]. We can expect the plateau appears at around 6.4 hours using the formula: $t = \frac{l^2}{2D_0 \cdot exp(-\frac{Q_0}{RT})}$. Therefore, charging at constant applied potential and measured without surface cleaning can not control the saturated hydrogen concentration and obtain reproducible, unscattered data.

4.3.2 H content profile with ultrasonication at constant potentials

Given that the foil is very thin, which is 50 μm thick, surface contaminants and deposits such as hydride will affect the accuracy of hydrogen concentration measurement. For this reason, surface cleaning using ultrasonication is necessary to remove the excess hydrogen at the surface of the sample in the form of hydride and other composites. We then conducted the same charging experiments but with surface cleaning. Fig 21 is the plot of hydrogen concentration measured after surface cleaning.

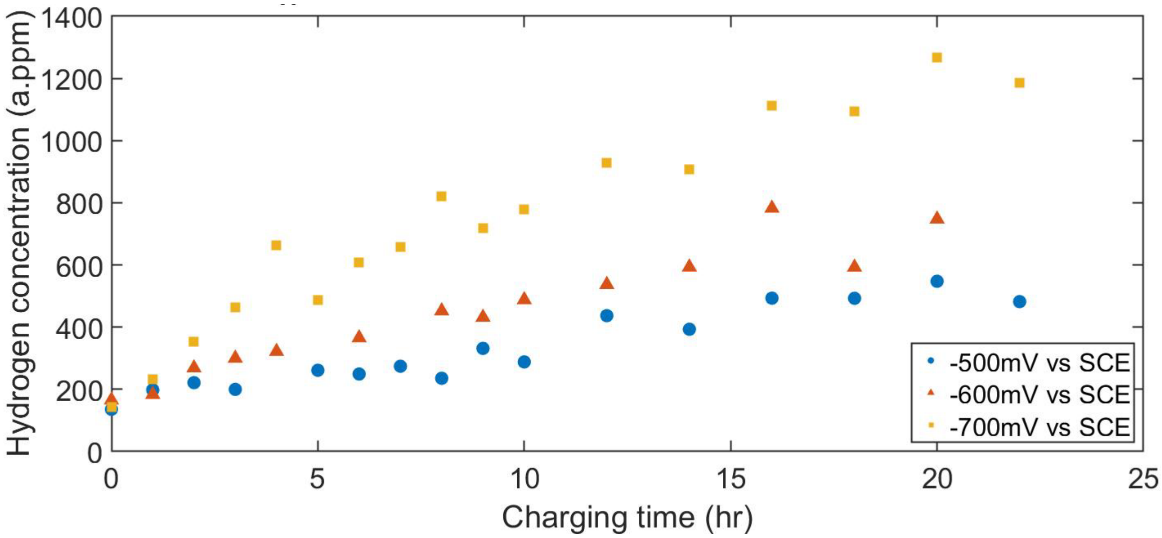

Figure 21: Plot of C_H vs charging time at different applied potential with surface cleaning.

The data is less scattered than the data without surface cleaning because of surface cleaning. Notice that the hydrogen concentration with the same charging condition is all decreases by about 500 a.ppm compared to the data without surface cleaning. Assuming this amount of hydrogen all evenly distributed at the surface of the sample and a simple "back-of-the-envelope" calculation can rationalize it: $\frac{\mathrm{N_H}}{2S} = \frac{\Delta \mathrm{C_H} \cdot \mathrm{N_{Ni}}}{2S} = \frac{\Delta \mathrm{C_H} \cdot \rho_{Ni} \cdot V_{foil}}{2S \cdot V_{Ni}} \approx 10$ ($\Delta \mathrm{C_H}$ is the hydrogen concentration difference after cleaning, V_{Ni} is the volume of a single nickel atom, S is the sample's surface area). That means there are 10 excess hydrogen atoms per square angstrom, which is reasonable. Therefore, using ultrasonication can effectively remove the excess hydrogen on the surface of the sample after charging, which enables us to have an accurate measurement of the hydrogen concentration inside the sample.

4.3.3 Evolution of Open Circuit Potential (OCP) at constant potentials

Even though using the proper surface cleaning method benefit us to have better hydrogen concentration data, concentration plateaus that represent samples are fully charged are still missing. By monitoring the change of open circuit potential (OCP) during charging, which is illustrated by Fig 2, we found that the open circuit potential (OCP)

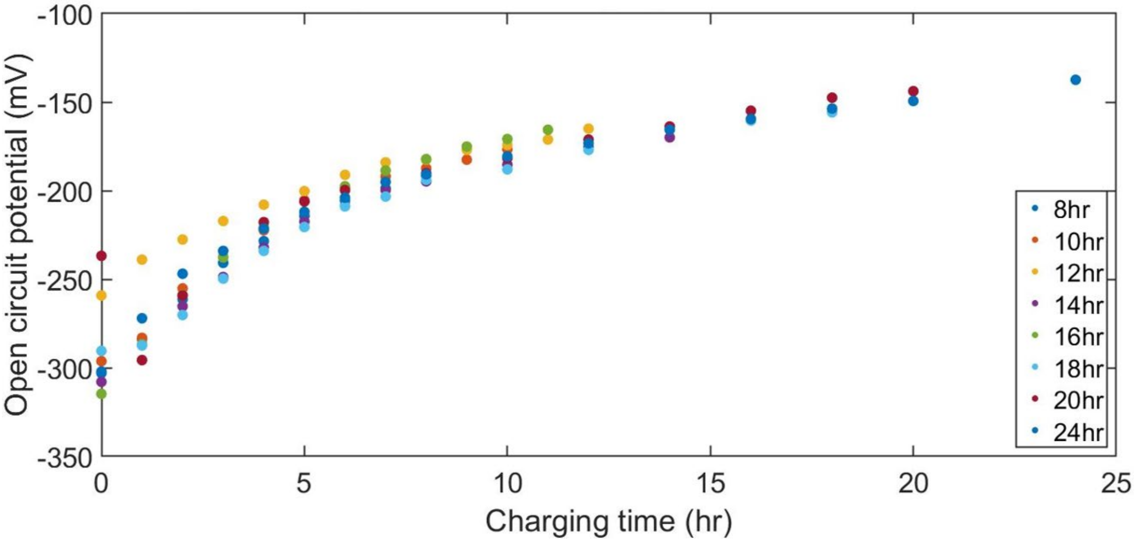

Figure 22: Open circuit potential change with charging time.

Therefore, if samples are charged at constant applied potential E, the overpotential will gradually increase due to the change of open circuit potential. It also explains why the concentration curves keep increasing with increase charging time and it gradually slows down after 10 hours of charging, which matches perfectly with the open circuit potential curves in Fig 22.

4.3.4 The upper limit on equilibrium H concentration

In light of the situation described above, we decided the cathodic charging should be at constant overpotential and measure hydrogen concentration after surface cleaning. Fig 23 is the plot of hydrogen concentration versus charging time with surface cleaning at different constant overpotentials. The data is much less scattered than the data measured without surface cleaning. Besides, all concentration curves reach a plateau after being charged for around 6-8 hours. This also accords with the calculation for saturation time described previously, samples should be fully charged after 6-7 hours. Therefore, by charging at constant overpotential and measuring hydrogen concentration after surface cleaning, we can obtain hydrogen concentration curves with plateaus as expected.

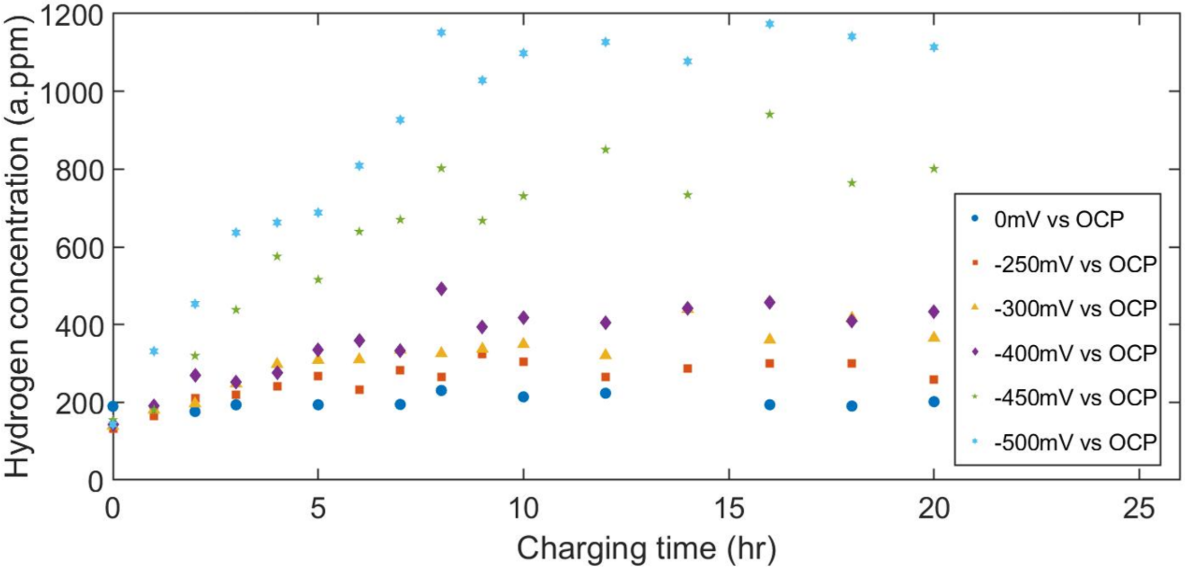

Figure 23: Hydrogen concentration vs. charging time at different η measured after surface cleaning.

The plateaus appear after around 7 hours of charging and there is always a positive correlation between the saturated concentration and overpotential, as expected. Equilibrium concentration on different overpotentials can be determined by finding where those plateaus at.

Recent studies by Kirchheim and Pundt[84] proposed a quantitative relationship between hydrogen pressure and the voltage difference under electrochemical loading (Eqs 3). Combining this with Sievert's Law (Eqs 4)[85, 86], which describe the relation between hydrogen concentration in metal and the gas pressure, $c_H \sim \sqrt{p_{H_2}}$, a quantitative relationship between hydrogen concentration in metals at thermodynamic equilibrium and electrochemical potential can be derived (Eqs 5):

$$U - U_0 = -\frac{RT}{2F} ln \frac{p_{H_2}}{p_0} \tag{3}$$

$$C_H = \sqrt{\frac{p_{H_2}}{p_0}} exp\,(-\frac{\Delta H_H^{M-gas} - T\Delta S_H^{M-gas}}{k_B T}) \tag{4}$$

$$C_H = exp\,(-\frac{(U - U_0)F}{RT} - \frac{\Delta H_H^{M-gas} - T\Delta S_H^{M-gas}}{k_B T}) \tag{5}$$

Here the equilibrium H concentration reached at charging times beyond ~7 hours varies with the overpotential, as shown in Fig. 24.a). To validate the relationship mentioned above, we can plot $-kBTlnC_H$ vs overpotential η based on the experimental results as shown in Fig. 24.b), and compare the slopes and intercepts with the theoretical prediction of Kircheim and Pundt[84] based on Eqn (5):

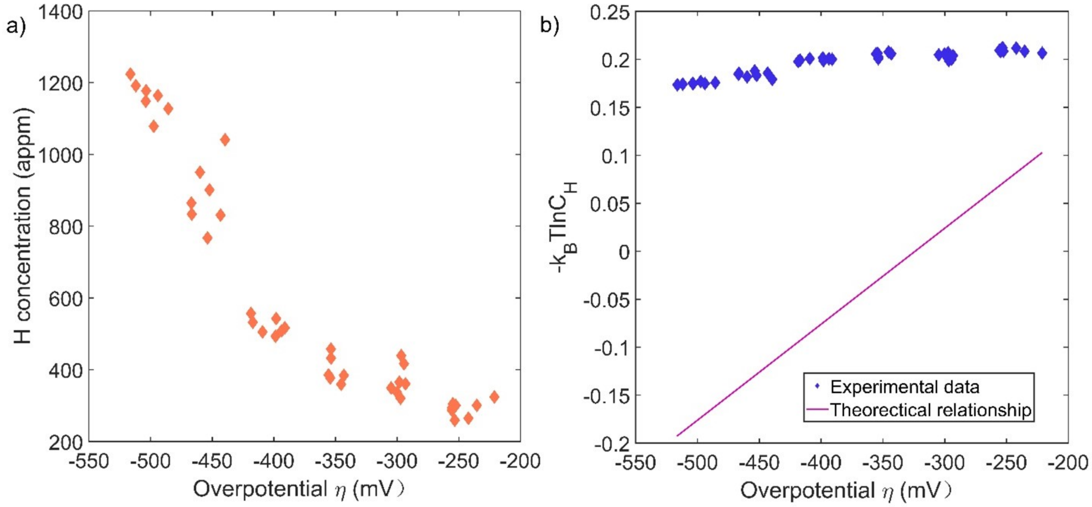

Figure 24: a) Equilibrium H concentration vs overpotential as measured in the experiments and b) comparison of the measured H concentration with predictions from the theoretical relationship proposed by Kirchheim and Pundt.

4.3.5 Hydrogen content vs current at different overpotentials

We monitored current density during charging at different overpotentials and found it insightful to plot against measured hydrogen concentration, which is shown in Figure 25.

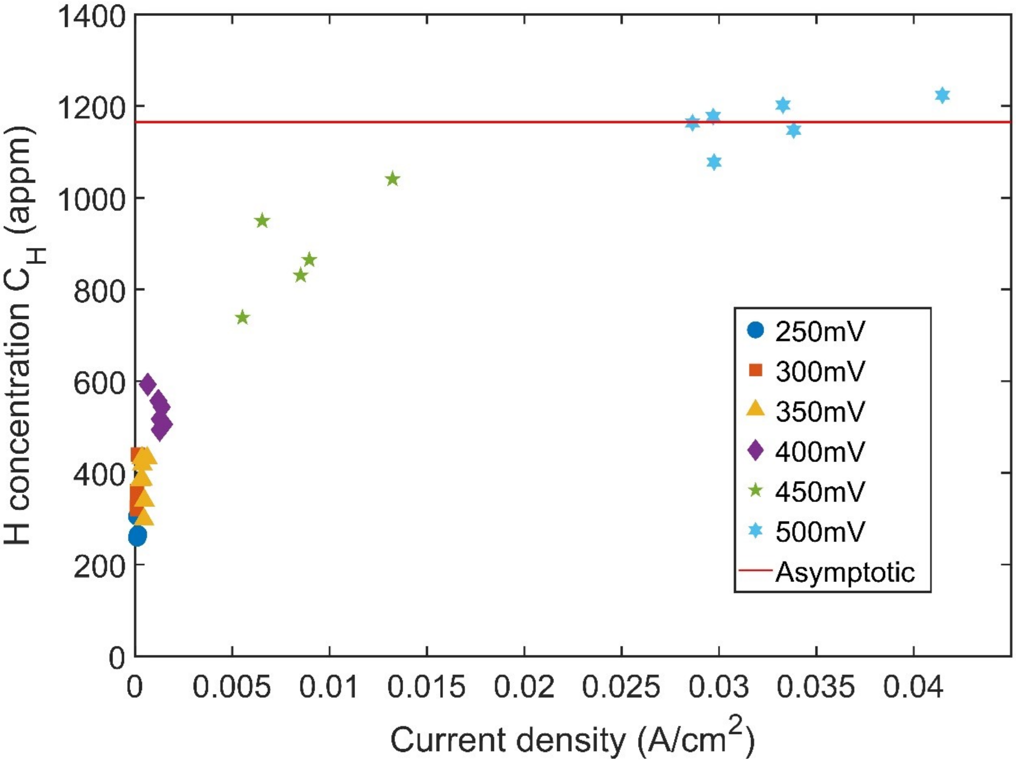

Figure 25: Hydrogen concentration vs. steady-state current density at different overpotentials η measured after surface cleaning.

influence on surface H activity, however. The rest of this section elucidates a theoretical explanation for these results.

4.3.6 Surface coverage of hydrogen limits H uptake

To better rationalize the findings regarding the limited H uptake presented in the above sections, here is a proposed model of H concentration absorbed into the Ni cathode based on the detailed balance between H within the cathode and H adsorbed onto the cathode surface, i.e., that thermally-activated ingress of H from the surface into the interior proceeds at the same rate, r_{in}, as the thermally-activated egress of H from the interior onto the surface, r_{out}. This condition obtains when the cathode surface and interior are in thermodynamic equilibrium with each other, as shown in Fig. 26.

The H surface activity, on the other hand, is not a thermodynamic equilibrium state because it is not dictated by precise balance. Rather, following Turnbull[89], It is a non-equilibrium stable state formed by a balance of electrochemically driven processes that produce atomic H near the cathode surface (at a rate r_{elec}) and recombination of atomic H into H_2 molecules, which agglomerate and bubble off irreversibly from the cathode surface (r_{bub}), as shown in Fig. 26. In this scenario, H surface activity is limited by the activation of a surface H removal pathway whose rate increases rapidly with H surface coverage, allowing the current density to increase even as surface H activity remains unchanged. The following subsections provide a quantitative discussion of the qualitative model proposed in Fig. 26.

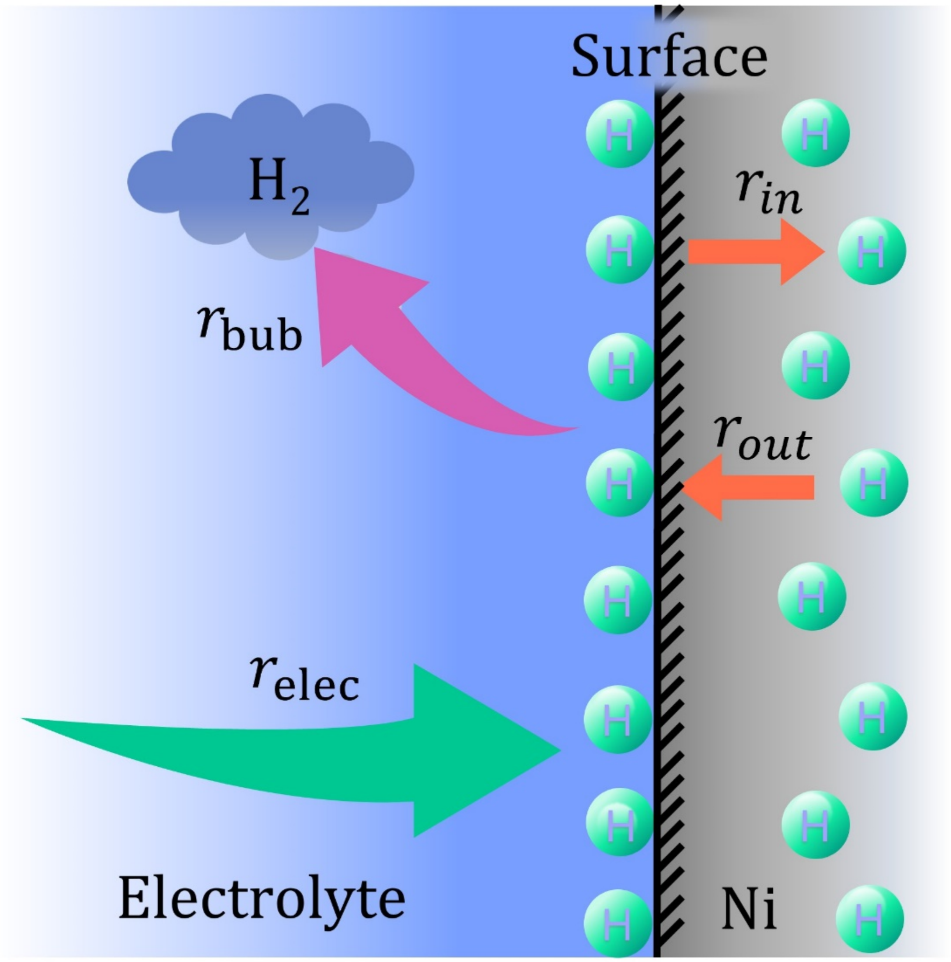

Figure 26: Detailed balance holds between H adsorbed at the Ni cathode surface and that absorbed inside the cathode interior. It does not hold true, however, between H adsorbed on the Ni cathode surface and H in the electrolyte.

Figure 7 shows a schematic of the relative free energies of H when adsorbed onto the cathode surface and when absorbed into the cathode interior. All energies are measured relative to that of H_2 gas at zero pressure. The rate of H ingress from the surface may therefore be written

$$r_{in} = \nu\theta e^{-(\Delta E' + E_a)/k_B T} \qquad (6)$$

where ν is the transition attempt frequency, θ is H surface activity, $\Delta E'$ is the energy difference between H in the interior and on the surface of the cathode, and E_a is the activation energy barrier for H egress, as illustrated in Fig. 7. The rate of H egress from the interior is

$$r_{out} = \nu c_H e^{-E_a/k_B T} \qquad (7)$$

where any discrepancies in entry and egress attempt frequency are expected to be ignored. There is no net H exchange between the surface and the inside of the body when it is in thermodynamic equilibrium, i.e., $r_{in} = r_{out}$, so

$$c_H = \theta e^{-\Delta E'/k_B T} \qquad (8)$$

Thus, if the energy, $\Delta E'$ is known, we can calculate the activity, θ, from the experimentally observed H concentration, c_H.

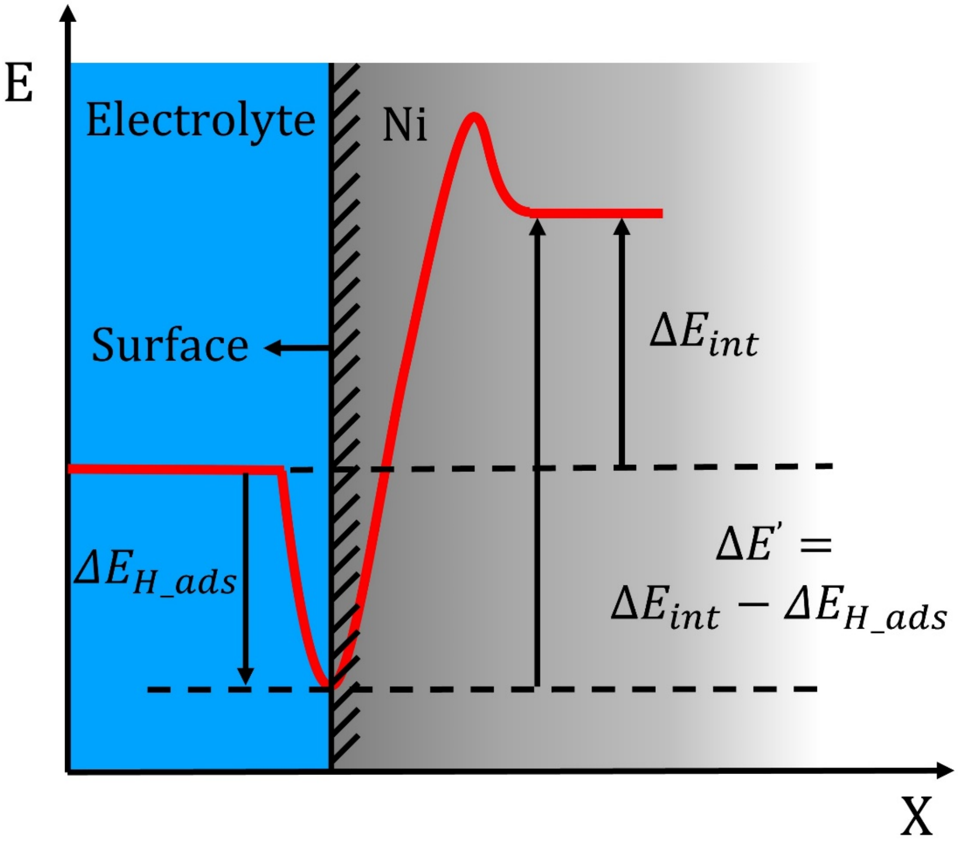

Figure 27: Energy diagram of H adsorbed on the Ni cathode surface and H absorbed inside the Ni cathode interior.

Following Fig. 27, we write

$$\Delta E' = \Delta E_{int} - \Delta E_{ads} \qquad (9)$$

Here, $\Delta E_{int} = h_H^M - TS_H^M$ is the formation of free energy of H interstitials in Ni ($\Delta E_{int} = 0.3389eV$ at $T = 298K$ [86]) and ΔE_{ads} is the adsorption energy of H atoms on the surface of Ni. Previously published density functional theory (DFT) research provide estimates for the latter. The adsorption energy of individual H atoms on Ni surfaces has been reported by a number of researchers[90-92]. However, we are aware of only three that reported ΔE_{ads} as a function of pre-existing H surface coverage[93-95]. All three studies considered adsorption of individual H atoms onto singular, [111]-type surface facets exposed to vacuum. Surface coverage is defined as the ratio of H atoms per unit surface area to Ni atoms per unit surface area of a single [111] atomic monolayer.

The findings of these studies are summarized in Fig. 28. All three predict negative adsorption energy at zero coverage, implying that the transition from H_2 molecular gas to atomic H adsorbed on a bare Ni surface is exothermic. Two researchers believe that as coverage grows, absorption will become less exothermic. There are, nonetheless, significant quantitative disparities between them. While Greely and Mavrikakis[94] and Yatsymyrskyi[95] *et al.* and both report comparable adsorption energies at zero coverage (-0.57eV and -0.61eV, respectively), Shirazi *et al.* report a value of -0.32eV[93]. Furthermore, according to Shirazi *et al.*, the adsorption process switches from exothermic to endothermic beyond the coverage of 0.8. By contrast, all the adsorption energies reported by Yatsymyrskyi *et al.* as well as Greely and Mavrikakis are negative, meaning that H adsorption is exothermic relative to H_2 gas at all reported coverages. In a comprehensive review of first-principles simulations of H adsorption onto metal surfaces, Faglioni and Goddard[96] argue that discrepancies such as these are to be expected when comparing studies that use different DFT settings (as is the case for the three aforementioned studies). As a result, we believe that these inconsistencies reflect the inherent errors of DFT modeling.

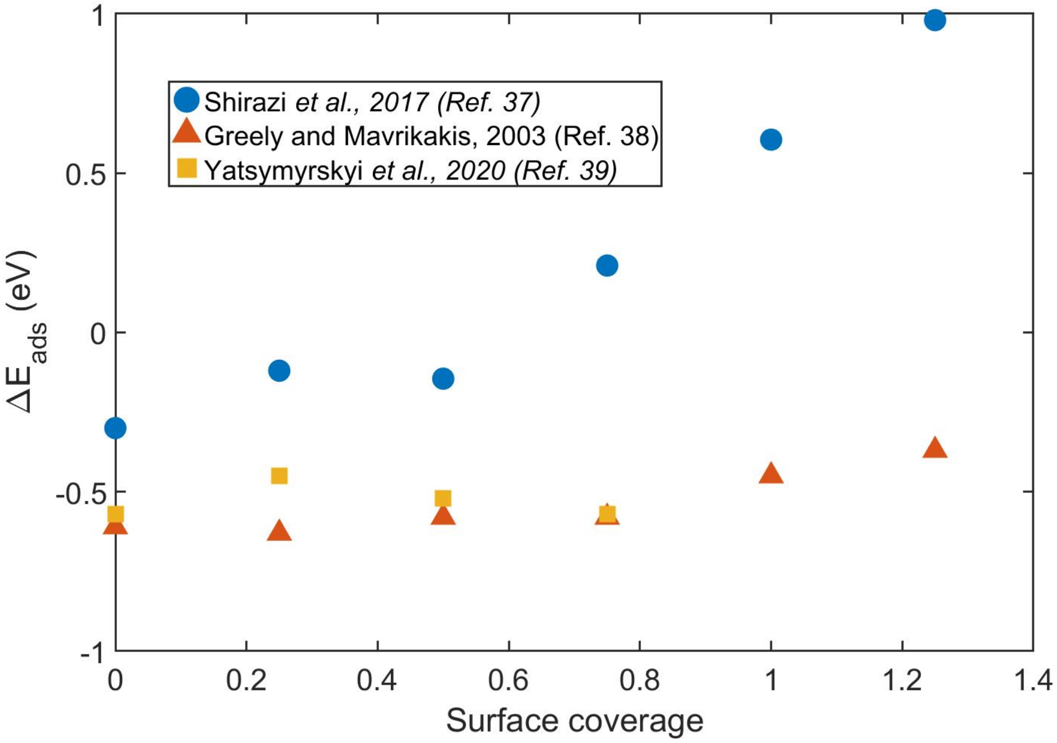

Figure 28: Adsorption energy ΔE_{ads} of H onto vacuum-facing Ni {111} surfaces as a function of surface coverage.

We construct quadratic least-squares fits for the data sets of Greely and Mavrikakis[94] and Shirazi *et al.*[93], shown in Fig. 27, to obtain numerical expressions for ΔE_{ads} as a function of surface coverage.

$$\Delta E_{ads}(\theta) = p_1\theta^3 + p_2\theta^2 + p_3\theta + p_4$$

	p_1	p_2	p_3	p_4
Greely and Mavrikakis	0.0967	-0.0323	0.0036	-0.6203
Shirazi *et al.*	0.1394	0.3738	0.0035	-0.3126

Table 2: Fitting parameters for Quadratic least-squares fits conducted on the DFT adsorption energy data sets.

The coefficients of these fits are given in Table 2. We do not fit the data of Yatsymyrskyi[95] *et al.* as it spans an insufficient range of surface coverages to capture the reduction of H adsorption energies at high surface coverage seen in the two other data sets. We use the fitted expressions for ΔE_{ads} in conjunction with Eqn. 8 and 9 to compute c_H. If we identify H activity, θ, with surface coverage, we obtain:

$$c_H = \theta e^{-(\Delta E_{int} - \Delta E_{ads}(\theta))/k_B T}. \qquad (10)$$

Since this equation is transcendental, we solve it numerically. Fig. 29 shows the resulting variation in surface coverage, predicted over the range of experimentally observed H concentrations (0 appm -1500 appm). The computed surface coverage based on the date sets of Yatsymyrskyi is not shown in Fig. 29 as their computed adsorption energy is decreasing with increasing surface coverage. Fitting this data set and extrapolating beyond unity coverage gives a further exothermic trend towards higher surface coverage, which eventually results in a diverge surface coverage without limit to the orders of 10 within our experimentally observed hydrogen concentration range. The adsorption energy data set of Greely and Mavrikakis does have a trend towards endothermic with an increasing surface coverage of H. However, their computed data does not capture the crossover from exothermic to endothermic. A further extrapolation of the data yields a crossover point at ~2 surface coverage of H, which explains the surface coverage capped below 2 within the range of our experimentally observed H concentration. The adsorption energy data of Shirazi *et al* has the most complete surface coverage range with the endothermic trend that captures the crossover point around 0.8 H surface coverage. This characteristic predict the H surface coverage converge to ~1 within our experimentally measured H concentrations.

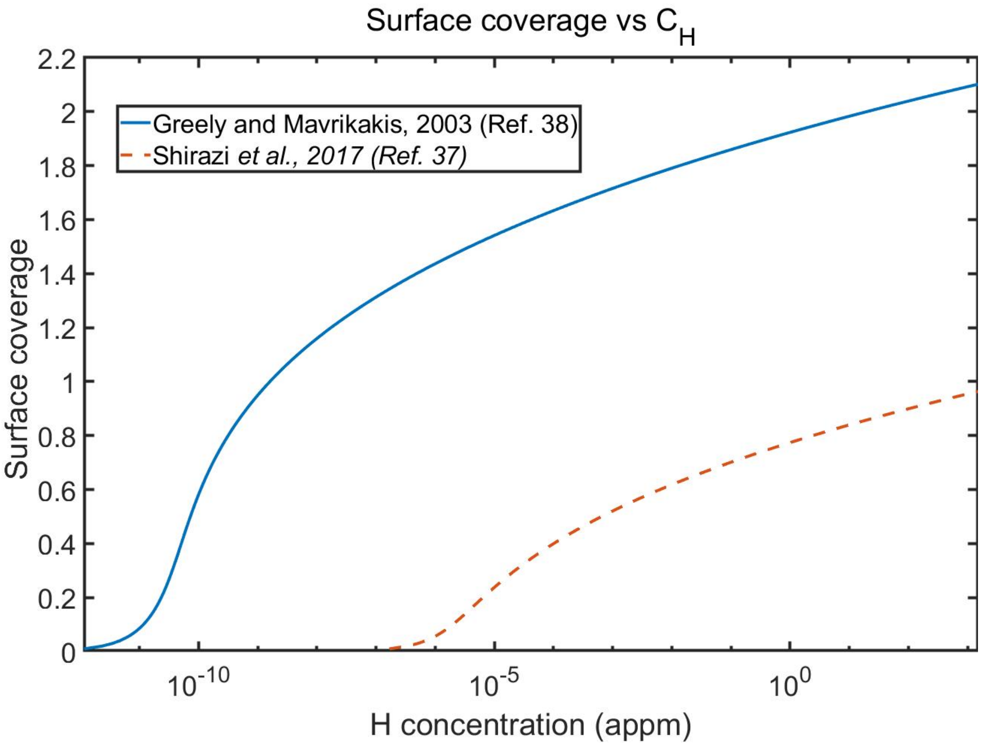

Figure 29: Surface H coverage vs. equilibrium H concentration in the cathode computed by numerical solution of Eqn. 6.

Following the discussion of Fig. 29, we conclude that the asymptotic value of the coverage should correspond to the coverage when the adsorption process switch from being exothermic to being endothermic. Therefore, we choose the study of Shirazi *et al* for all of our calculations since theirs is the only one that has the crossover from exothermic to endothermic with their computed data points without extrapolation.

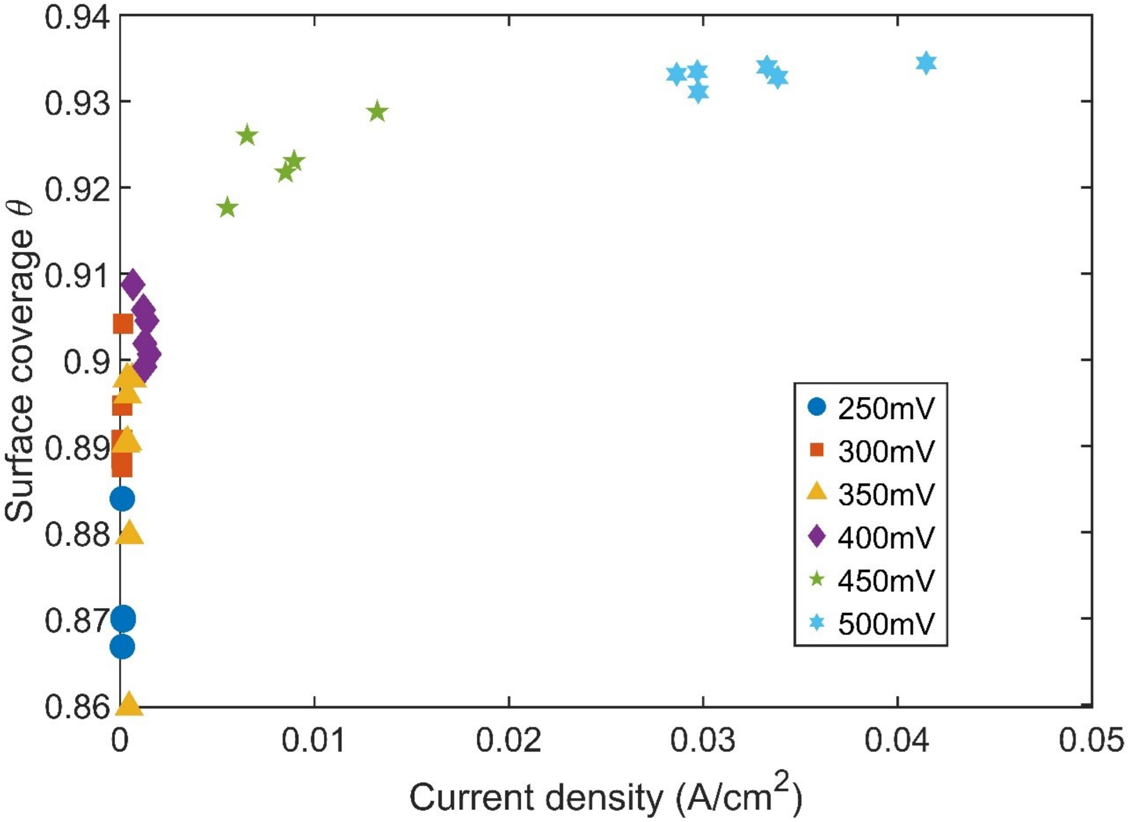

Figure 30: Surface H coverage (obtained using H adsorption data from Shirazi *et al.*[93]) vs. current density.

Fig. 30 shows the calculated H surface coverage of our experimentally H concentration date points over the range of measured current density using the adsorption energy date from Shirazi et al. The surface coverage on the sample is already high even under small current density. This suggests the adsorbed hydrogen covers the Ni sample surface extensively once the charging is on regardless of the current density. However, as illustrated by Fig. 30, the significant increase of the current density does not result in a huge increase in the surface coverage. In fact, the surface coverage eventually approaches some asymptotic value regardless of the increasing current density. This characteristic indicates some mechanisms should be responsible for limiting the surface coverage of H independent of current density, which will be discussed in detail in the next section.

4.3.7 Surface reactions during electrochemical H charging

Because there is no net H exchange between the cathode surface and the interior once a detailed balance is established, electrochemical interactions between the surface and the electrolyte govern the H activity on the surface. The irreversible bubbling off of H_2 gas from the cathode surface, as shown in Fig. 26, is one of the reactions' outcomes. As a result, detailed balance fails, and time-invariant H surface activity is not a thermodynamic equilibrium state. It is a kinetically driven stable state, rather. Furthermore, as seen in Fig. 30, surface activity saturates during cathodic charging while the current increases without bound. The purpose of this section is to explain these findings using surface electrochemical processes as a basis.

We begin by expressing the current density, i, and the rate of change of surface coverage, $\dot{\theta}$, in terms of contributions from the canonical cathodic reactions, namely:

Volmer: $H_3O^+ + e^- \rightarrow H_{ad} + H_2O,$

Tafel: $2H_{ad} \rightarrow H_2,$

Heyrovsky: $H_{ad} + H_3O^+ + e^- \rightarrow H_2 + H_2O.$

Here, H_{ad} denotes H adsorbed on the cathode surface. Since the Tafel reaction does not contribute to charge transfer, the current density may be written

$$i/e = r_V + r_H, \tag{11}$$

where r_V and r_H denote Volmer and Heyrovsky reaction rates (expressed in #/m^{2}s), respectively. The rate of change of surface coverage is

$$\dot{\theta} = 0 = r_V - 2r_T - r_H - r_X. \tag{12}$$

The contribution of the Volmer reaction (r_V) is positive because it involves adsorption of H onto the cathode surface. By contrast, both the Tafel (r_T) and Heyrovsky (r_H) reactions remove H from the cathode surface. The factor of two in front of the Tafel term indicates that every instance of this reaction removes two adsorbed H atoms.

Under steady state, the surface coverage no longer changes with time. Thus, we set $\dot{\theta} = 0$ in Eqn. 12. Solving for r_V and substituting into Eqn. 11, we arrive at

$$i = 2e(r_T + r_H). \tag{13}$$

Therefore, under the conditions of our experiment, current density may be expressed in terms of just those reactions that remove adsorbed H from the cathode surface. We write the reaction rates as

$$\begin{gathered} r_T = k_T\theta^2, \\ r_H = k_H e^{-\beta_H e\eta/k_B T}\theta, \end{gathered} \tag{14}$$

where k_T and k_H are empirical rate constants and $\beta_H \approx 0.5$ is the symmetry factor for the Heyrovsky reaction[97]. Following previous analyses[98, 99], we solely account for forward processes and assume that, given the conditions of our experiment, the rates of the equivalent reverse processes are minimal.

Taking $k_T = 7.8 \cdot 10^{-9}$ mol/cm^{2}s and $k_H = 1.9 \cdot 10^{-10}$ mol/cm^{2}s from Bhardwaj and Balasubramaniam[99] and $\eta \approx -3.613\theta + 2.916$ from a linear least-squares fit to our own data, we arrive at the relationship between surface coverage and current density plotted in Fig. 31. This calculated relationship is in qualitative agreement with our experimental findings. The agreement is further improved if we modify the expression for the Heyrovsky reaction rate to

$$r_H' = k_H e^{-\beta_H\left(e\eta+\Delta E_{ads}(\theta)\right)/k_B T}\theta, \tag{15}$$

where $\Delta E_{ads}(\theta)$ is the coverage-dependent H adsorption energy obtained from fitting the DFT calculations of Shirazi *et al.*[93] (fitting coefficients given in Table 2). The current density is quantitatively consistent with our experiments using this adjusted formulation.

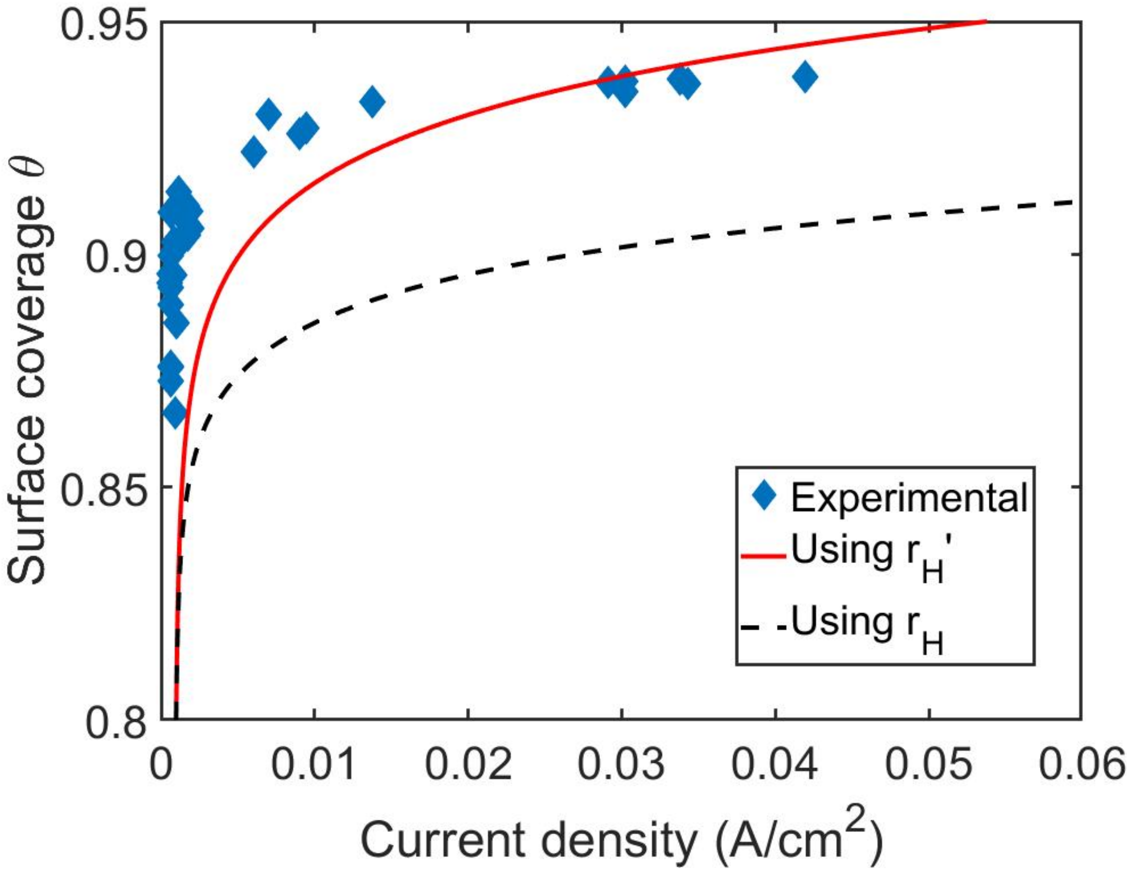

Figure 31: Relationship between surface coverage and current density calculated using Eqn. 13 with the Heyrovsky reaction rate expressed as in Eqn. 14 (r_H) or Eqn. 15 (r_H'). For comparison, we also plotted our experimental results.

The rapid rise in current density with increasing surface coverage is due to the Heyrovsky reaction, whose rate is an order of magnitude greater than that of the Tafel above $\theta \approx 0.9$. According to Eqn. 8, whenever $r_T \ll r_H$, it follows that $r_H \approx r_V$. Thus, no matter the rate of charge transfer, surface coverage remains constant because adsorbed H is replenished by the Volmer reaction as quickly as it is depleted by the Heyrovsky. The foregoing analysis shows that the dominance of the Heyrovsky reaction over the Tafel governs the steady-state surface coverage at high current density and therefore determines the maximum H uptake into the solid.

4.3.8 Derivation of theoretical Tafel slope of different reaction pathways

Further insight into the dominance of Heyrovsky reaction on the electrochemical surface reaction kinetics and its corresponding overpotential/current and H surface coverage can be acquired based on the comparison between experimentally observed Tafel slope and theoretical derived Tafel slopes. The derivation process is demonstrated below:

Volmer-Heyrovsky reaction pathway:

For Volmer reaction, forward reaction and backward reaction have their rate constant based on its rate law. Based on the relationship between overpotential, applied potential, and OCP which previously stated, $\eta = E - E_0$, the reaction rates can be written as:

$$V_1 = k_1[H^+](1-\theta)e^{(\alpha-1)f\eta} \tag{16}$$

$$V_{-1} = k_{-1}\theta e^{\alpha f\eta} \tag{17}$$

Here, E is the applied electrode potential, θ is the surface coverage of adsorbed hydrogen and α is the transfer coefficient.

Similarly, the rate of Heyrovsky reaction is:

$$V_2 = k_2^0[H^+]\theta e^{(\alpha-1)fE} = k_2[H^+]\theta e^{(\alpha-1)f\eta} \tag{18}$$

Generally, the charge transfer coefficient α is taken to be the same for each reaction. For adsorbed H proton, when the steady-state is achieved, yields dθ/dt= 0:

$$\begin{aligned} V_1 - V_{-1} - V_2 \\ &= k_1[H^+](1-\theta)e^{(\alpha-1)f\eta} - k_{-1}\theta e^{\alpha f\eta} \\ &- k_2[H^+]\theta e^{(\alpha-1)f\eta} \end{aligned} \tag{19}$$

And θ is solved as:

$$\theta = \frac{k_1[H^+]}{(k_1+k_2)[H^+] + k_{-1}\theta e^{f\eta}} \tag{20}$$

As the full derivation is rather complicated, here two cases for surface coverage θ of the adsorbed H proton were discussed: $\theta \approx 0$ and $\theta \approx 1$. When $k_{-1} \gg k_1, k_2, \theta \approx 0$ and Eqn (16) can be written as:

$$\theta = \frac{k_1[H^+]}{k_{-1}\theta e^{f\eta}} = K_1 \frac{[H^+]}{\theta e^{f\eta}} \tag{21}$$

Where K_1 is the equilibrium rate constant of Volmer reaction at low H coverage. An electric current can be simply related to the reaction rate V by the following relationship:

$$I = nFAV \tag{22}$$

Where I is the electric current, n is the number of electrons that participate in the reactions, and A represents the surface area of the electrode. Therefore, combining Eqn (18), (21), and (22) with some manipulation yields:

$$\frac{\partial\eta}{\partial \log i} = 2.303 \frac{RT}{(\alpha - 2)F} \tag{23}$$

When transfer coefficient $\alpha = 0.5$, the corresponding Tafel slope is -40mV/dec, which is the criteria for determining the reaction mechanism as Volmer-Heyrosky pathway at low H coverage.

Similarly, when H coverage is high ($\theta \approx 1$), yields:

$$\frac{\partial \eta}{\partial \log i} = 2.303 \frac{RT}{(\alpha - 1)F} \tag{24}$$

Corresponding Tafel slope is -120mV/dec if $\alpha = 0.5$ and also is the criteria for Volmer-Heyrovsky pathway at high H coverage.

Volmer-Tafel reaction pathway:

The derivation for theoretical Tafel slope of Volmer-Tafel reaction pathway is similar and yields:

$$\frac{\partial \eta}{\partial \log i} = 2.303 \frac{RT}{2F} \tag{25}$$

Tafel slope is -30mV/dec if $\alpha = 0.5$ for the case of low H coverage ($\theta \approx 0$). At high coverage ($\theta \approx 1$), $I = Fk_3$ which means the electric current is kinetically limited and no longer depends on pH or overpotential.

4.3.9 Comparison of experimentally and theoretically determined Tafel slopes

Figure 32 is a Tafel plot obtained by performing LSV on a Ni sample after 16 hrs of charging under -400mV overpotential. The cathodic side has three sections with distinct Tafel slopes. The section in the purple dashed box A has a Tafel slope ~30mV/dec, that in the red dash-dotted box B has ~1300mV/dec, and the one in the green dotted box C ~110mV/dec. Analysis of these slopes gives insight into the reaction pathways that govern charge transfer at the cathode. Following the theoretical treatment by Shinagawa *et al.*[100], we conclude that the slopes in the first two boxes (~30mV/dec and ~1300mV/dec) are consistent with charge transfer dominated by the Volmer-Tafel mechanism with the Tafel reaction as the rate-determining step. The range of overpotentials with low or high Tafel slope corresponds to low or high surface coverage by adsorbed H, respectively. The Tafel slope in the third box (~110mV/dec) is consistent with charge transfer dominated by the Volmer-Heyrovsky pathway with the Heyrovsky reaction as a rate-determining step at high H surface coverage.

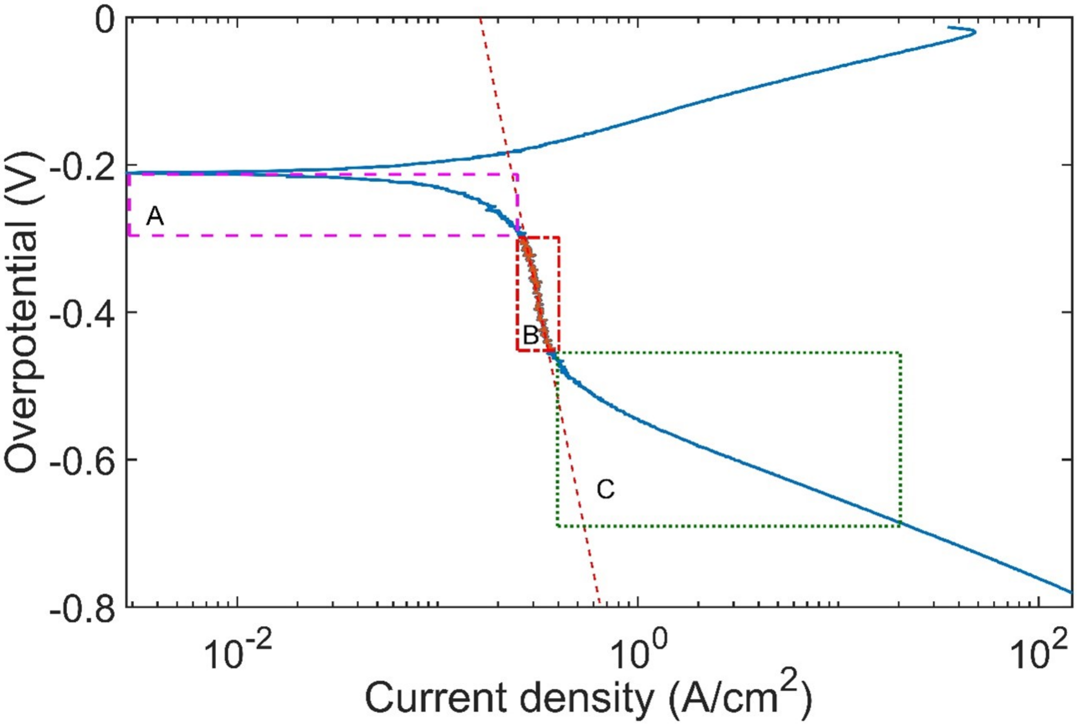

Figure 32: Tafel plot of Ni sample after 16 h of charging under -400mV overpotential.

Therefore, the Tafel slope analysis based on the LSV measurements on the Ni sample under electrochemical charging condition indicates the HER reaction pathway operates via Volmer-Tafel at low overpotential/current density and switch to Volmer-Heyrovsky at high overpotential/current density to accommodate the rapid increase of the current density

4.3.10 Determination of hydrogen diffusivity in Ni

The hydrogen diffusivity of the nickel foil used in the charging was also analyzed and determined using mathematical calculation. Given that our sample for the charging has a dimension of 50mm in length, 20mm in width and 0.05mm in thickness, hydrogen charging can be treated as a 1D thin-film diffusion problem in this scenario. Fortunately, for this specific 1-D diffusion problem, its analytical solution[101] already exists, which is :

$$\frac{C}{C_0} = \frac{4}{\pi}\sum_{n=0}^{\infty}\frac{1}{2n+1} sin[(2n+1)\pi\frac{x}{L}]e^{[-\frac{(2n+1)\pi^2 Dt}{L^2}]} \qquad (26)$$

With boundary conditions: $\begin{cases} C = C_\infty \,,\; 0 < x < L \,,\; t = 0 \\ C = 0 \,,\; x = 0 \; and \; x = L,\; t > 0 \end{cases}$

Here C_0 is initial concentration, x is the location along the thickness direction, L is the thickness and t is the charging time. By integrating over the thickness and dividing by L, we can have the overall average hydrogen concentration in the sample with respect to charging time only. Which is :

$$f(t) = \left[\int_0^L \frac{4}{\pi}\sum_{n=0}^{\infty}\frac{1}{2n+1}\sin[(2n+1)\pi\frac{x}{L}]e^{[-\frac{(2n+1)\pi^2 Dt}{L^2}]}\right]/\mathrm{L} = \sum_{n=0}^{\infty}\frac{8e^{[-\frac{(2n+1)\pi^2 Dt}{L^2}]}}{(2n\pi+\pi)^2} \qquad (27)$$

Since the periodic charging method was used to monitor OCP changes and adjust total applied potential in order to maintain constant overpotential for hydrogen charging, the whole charging process can be viewed as the superposition of each periodic charging. When measuring OCP, the power is off so hydrogen will diffuse out. Therefore when using an analytical diffusion solution to calculate the hydrogen concentration, those power-off periods also need to be taken into account. Therefore, a Matlab script was developed to decompose the overall charging time into many on/off periods (t_{on} and t_{off}), and plugin these t_{on} and t_{off} into Eqs (27) and do the superimposition. This will give us the relationship between concentration and charging time for the periodic charging shown in Fig 33. It's also worth mentioning that the value of n for the summation of Eqs 26 and 27 is 100.

Since the concentration measured by the G8 Galileo ON/H analyzer is the concentration when the sample is taken out from the cell and cleaned ultrasonically, which is happened at where descending part of the concentration plot in Fig 33. Therefore, the lower bound of the concentration plot should be chosen for fitting to determine diffusivity. Given that there are off periods that existed, the C/C_0 can never achieve 1 but a value under 1. Here the concentration ratio after 960 hrs charging has been chosen as the factor to rescale the theoretical data to make an accurate fit. As we only want to study the concentration change concerning charging time, not the overall hydrogen concentration. So all the experimental data should subtract hydrogen concentration from baseline measurement to get the concentration change after charging. The maximum concentration value of the experimental data has been chosen as

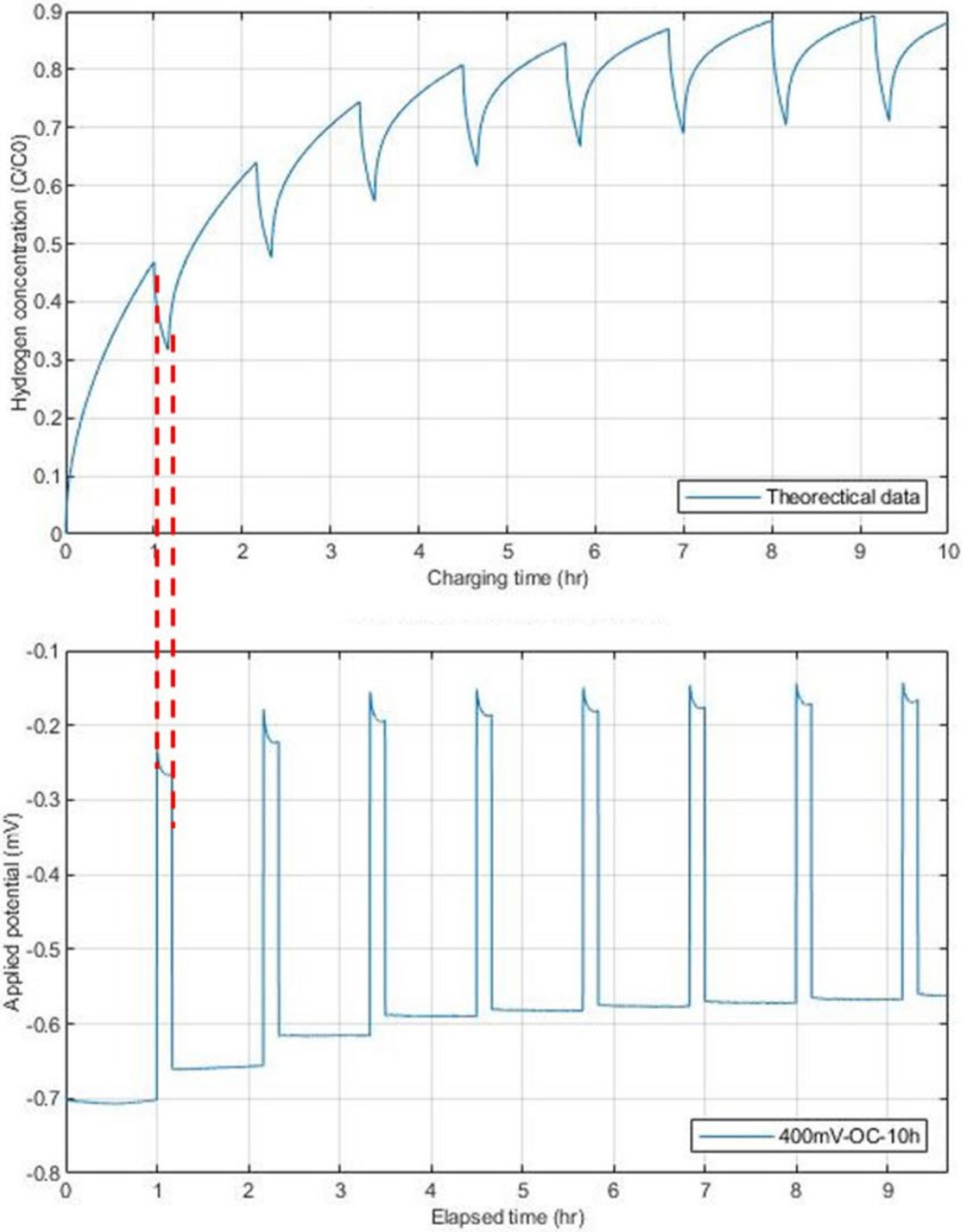

Figure 33: Demonstration of charging time decomposition for concentration calculation.

a factor to scale down all the experimental concentration data to 0-1 in order to do the fitting. Fig 34 shows what the raw experimental data is and how it looks like after being processed based on the method described previously.

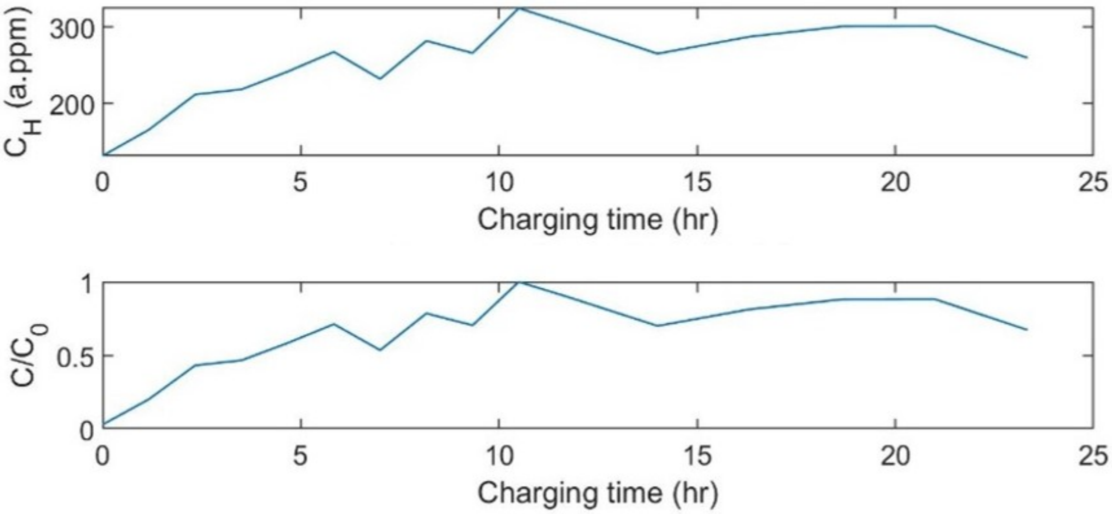

Figure 34: Raw experimental data and processed data of 250 mV overpotential charging.

After all these adjustments for processing the data. The least-square regression method was employed to do the fitting. The objective function that needs to be minimized is: $\mathrm{G}(D) = \sum_1^n (C_{exp} - C_{sim})^2$, n here is the number of the individual experimental data point. Fig 35 is an example of fitting for 500mV charging as well as a plot of experimental data and its fitting result.

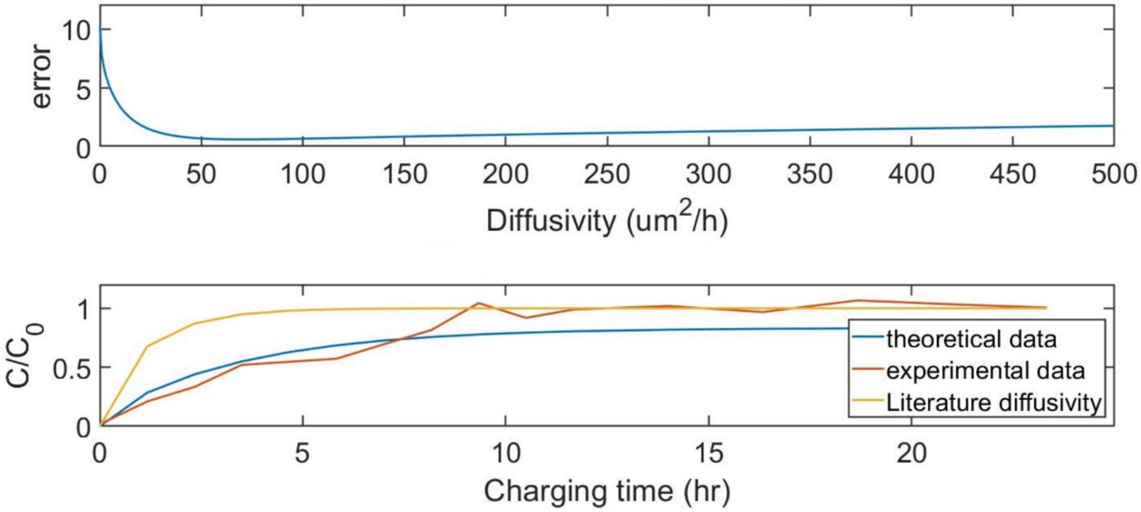

Figure 35: Example of diffusivity fitting (400mV) and comparison of theoretical data, experimental data, and literature diffusivity value

By doing fitting in the way described above, we obtained the hydrogen diffusivity in the pure nickel. However, the diffusivity value is slightly lower comparing to the values in published literature. Table 3 is the result of our fitting, the average is $68 \pm 37\ \mu\mathrm{m}^2/h$, while the published hydrogen diffusivity value in nickel[39] is $119\mu\mathrm{m}^2/h$.

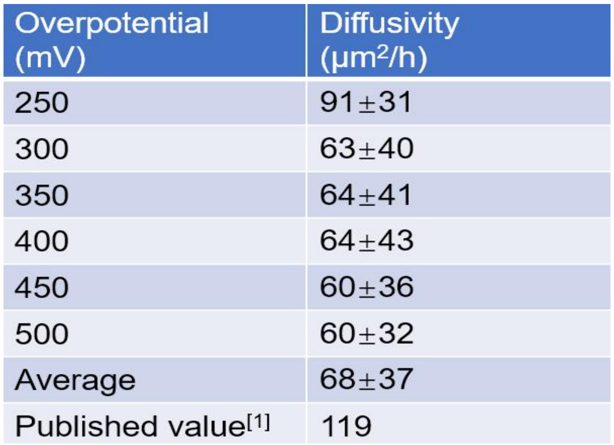

Overpotential (mV)	Diffusivity (μm^2/h)
250	91±31
300	63±40
350	64±41
400	64±43
450	60±36
500	60±32
Average	68±37
Published value[1]	119

Table 3: Diffusivity fitting result for constant overpotential charging.

However, given such a large uncertainty, this method may not be a good way to accurately determine the hydrogen diffusivity of Ni. There are so many factors that come from concentration measurement, 1-D diffusion model assumption, approximation, and the fitting objective function determination and optimization that can make determining diffusivity in this way less reliable. However, the ultimate goal of performing such calculation and prediction is that the predicted concentration profile based on published diffusivity value and this analytical 1-D diffusion solution is comparable to the experimental data, which suggests that the cathodic charging method we introduced can successfully charge the samples to an equilibrium state with hydrogen and the hydrogen concentration measurement is also capable of capturing the hydrogen concentration transient. It also indicates the fact that diffusivity is consistent and independent of overpotential and the hydrogen entry mechanism under cathodic charging is the diffusion process.

4.4 Discussions

The works on cathodic hydrogen charging on Ni foil and hydrogen concentration measurement after charging enable us to have further and a better understanding of hydrogen electrochemistry happen on Ni surface during charging. We first try to validate the relationship between charging overpotential and equilibrium hydrogen concentration which is based on the relation proposed by Kirchheim and Pundt[84] and Sievert's Law[85, 86], described in Eqs (2-4). But it turns out to has a very large discrepancy between the expected value and our experimental data. We tried to come out with some explanation such as a high resistivity surface layer causing a large potential drop during charging so that the effective overpotential on the Ni surface is significantly lower. Based on simple calculation given the resistance of the whole system is $12\,\Omega$ (measured by potentiostat) and assuming the resistance is negligible except for the sample, a 1 μm thick surface layer with a resistivity of $1.5 \times 10^5 \Omega/m$ can cause a 90% potential drop. This results in only 10% of the total overpotential on the sample surface, which lowers the calculated concentration to the same as what we measured. Furthermore, $1.5 \times 10^5 \Omega/m$ is very nearly the same as the resistivity of deionized water. However, this has too many unknown factors and needs further investigation. After analyzing the data we have, a surface coverage-dependent model is proposed. Different from what people used to control during hydrogen charging, such as overpotential or current density, to charge metal samples with hydrogen to different equilibrium concentrations. We found out the surface coverage of hydrogen is indeed the parameter or property that governs how much hydrogen the sample can uptake at equilibrium. This is derived from the fact that at equilibrium, there is no net hydrogen exchange between the Ni surface and its interior. Therefore, the thermodynamic relationship relates the equilibrium hydrogen concentration to hydrogen surface coverage by Eqn 8. Based on the equilibrium hydrogen concentration we measured and published DFT calculation data, the surface coverage profile at Ni surface has been created. The surface coverage of hydrogen can exceed 1, as shown in Fig 29. This may result from a few tetrahedral sites in the Ni FCC lattice are occupied by hydrogen and the site to lattice point ratio for these sites is 2:1 instead of 1:1 for the octahedral site.

Although the hypothesis based on the full H surface coverage and the Volmer-Heyrovsky reaction pathway addresses and explains the limited H uptake and increasing current behaviors pretty well, some other alternative explanations were able to stand a chance to shine but were failed due to all kinds of limitations. One of the candidates is the surface phase dissolution induced limited H uptake.

As mentioned in the previous section, While oxide formation on Ni is only expected under anodic polarization[44], cathodic charging of Ni under the conditions used here causes the formation of surface phases rich in Ni, O, H, and S by a process thought to involve the oxidation of a thin Ni hydride layer. The hydride or H-rick surface layer can then decompose and dissolve from the N sample into the electrolyte. Therefore, by knowing the amount of Ni atoms being dissolved into the electrolyte and assuming the surface phases have a certain H to Ni atomic ratio, the amount of the H atom loss and its corresponding current loss can then be calculated. Fig 32 is the Ni content vs charging time at various overpotentials. The slope of the plot represents the Ni dissolution rate and can be determined using the linear fitting method. The H to Ni ratio is 1.43 based on the hydrogen concentration measurements mentioned in the surface phases study by Jiang et al[102]. If the current loss is similar to the current difference between different overpotentials illustrated by Fig 36, the limited H uptake can then be completely explained by the surface phase dissolution. To validate this hypothesis, we conducted the Inductively coupled plasma mass spectrometry (ICP-MS) measurement to monitor the Ni concentration of the electrolyte during cathodic charging. The current loss due to the H loss from the surface phases dissolution can then be calculated and compared to the current difference across different overpotentials. The calculated current loss is close to the current at the low overpotentials range (0 to -300mV) but is 2 to 3 orders smaller at the high overpotential range (-400 to -600mV). Therefore, the hypothesis of dissolution of Ni surface layer is not sufficient to account for the limited H uptake.

One other explanation is that there may be a low diffusivity surface barrier that slows down the diffusion process of the H atom into the Ni sample. Some studies reported extremely low H diffusivity of surface metal oxide films that can retard the hydrogen embrittlement effect on stainless steel[103]. However, as the surface phases that formed on the sample is about 150nm, such a thin film with low H diffusivity may not have a significant influence on saturating the sample with H given that the Ni samples have been charged up to 24 hours. In fact, we simulated the hydrogen diffusion with consideration of such a low diffusivity layer for different layer thicknesses shown in Fig 37. The characteristic time for the sample to be 90% charged with H decrease with decreasing layer thickness and approaching the time without low diffusivity layer when the thickness is down to nm scale. Therefore, such a low diffusivity layer with nm scale thickness will not have a significant influence on the saturation time and is unable to explain the limited H uptake we observed.

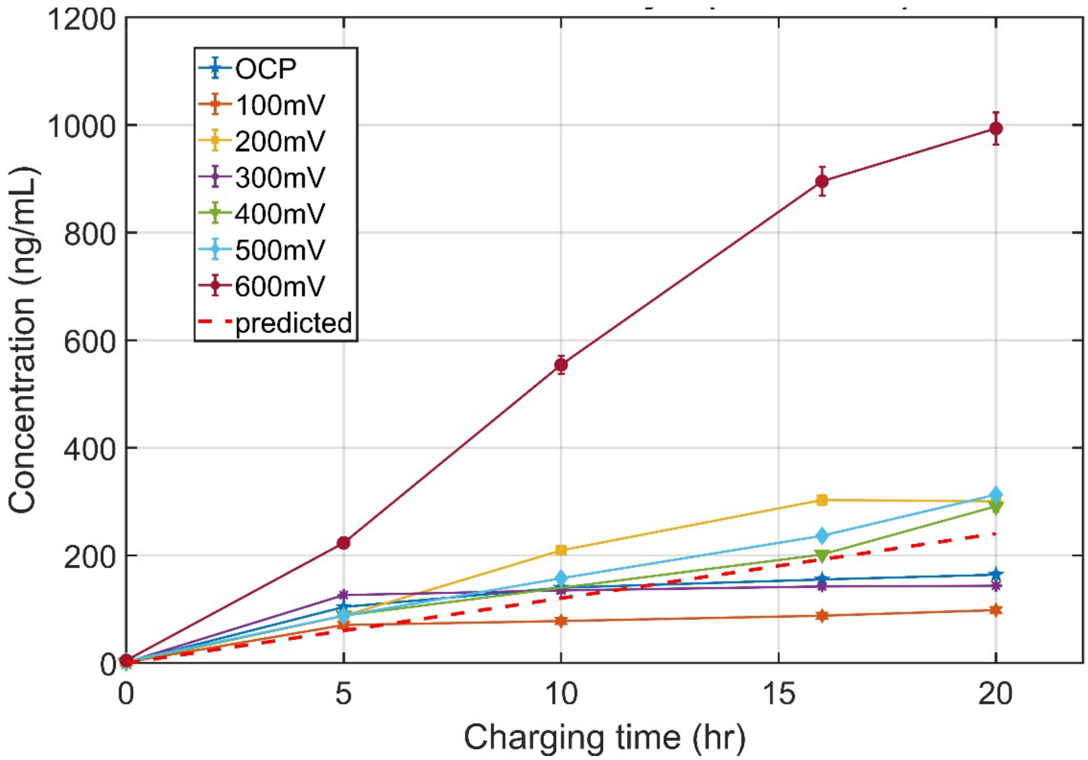

Figure 36: Nickel content vs charging time at various overpotentials. The red dotted line is the predicted Ni concentration vs charging time assuming the formation rate of the Ni-containing phases is equal to the dissolution rate and phases consist of 100% NiH_2SO_5 with 30% coverage and 150nm thickness.

The high resistivity layer could also hamper the HER and the consequent H uptake into the Ni sample by inducing a large IR drop to reduce the effective overpotential at the Ni surface. However, without switching of HER reaction from Tafel to Heyrovsky, increasing resistance for the whole circuit due to the formation of high resistivity layer alone must result in a decreasing current density under constant overpotential, which is contradicting to what we observed. Therefore, a high resistivity layer could be part of the hypothesis we proposed to some extent as the formation of superstoichiometric hydrides requires partial ingress of the atomic hydrogen through the surface layer into the Ni surface that the surface layer needs to be electron resistive and ion conductive.

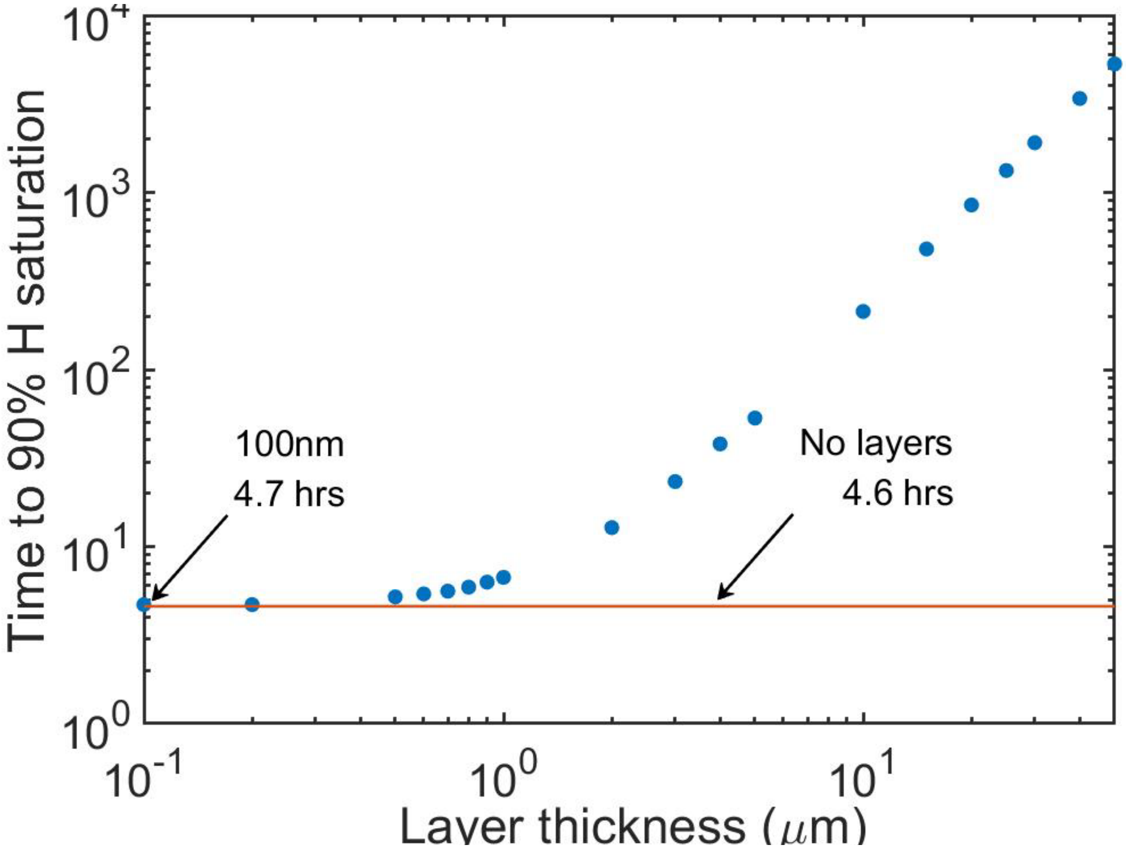

Figure 37: Characteristic time to achieve 0.9 C/C$_0$ with a low diffusivity layer (D = 0.1μm^2/h) vs layer thickness. The time to reach 0.9 C/C$_0$ without the low diffusivity layer is 4.6 hours.

One last alternative is the inhibition effect on HER by halide ions[104, 105] (e.g., chloride[106]) and on H adsorption[107]. This explanation falls apart similarly to the high resistivity layer by itself that the chloride ion inhibits the HER by decreasing the current density with an increase of chloride concentration, but what we observed is a continuing increase in current but limited hydrogen concentration. Therefore, what matters is why the H uptake reaches a ceiling rather than the amount of H being generated and uptake is lower than expected. In a nutshell, an appropriate hypothesis should address the question of where those H^+ ions are being reduced and then being adsorbed into the samples rather than the rate of HER and how much H^+ ion is being reduced.

Hydrogen evolution reaction under cathodic charging in the acidic aqueous environment usually has two possible reaction pathways: Volmer-Tafel and Volmer-Heyrovsky. During charging, electrons carried by the current from anode will first interact with H^+ at Ni surface to reduce it to the adsorbed hydrogen atom, which is the Volmer reaction. After that, if the surface hydrogen coverage is low, there is a possibility that two hydrogens will meet and recombine to form H_2 and escape from Ni surface to atmosphere in the form of the gas bubble, which is Tafel reaction (Illustrated by Fig 38.a). Tafel reaction also creates a new site for the next charge transfer. Therefore, the charge transfer rate will be limited by how fast those adsorbed hydrogen atoms recombine and escape from the Ni surface. Charge transfer and hydrogen recombination happen in a sequence order for the Volmer-Tafel reaction pathway. This further implies that current during charging will finally be limited by the hydrogen recombination rate or the Tafel reaction rate to a certain value no matter how large the potential is. We did not observe this current potential behavior from our charging experiments. On the other hand, for the Volmer-Heyrovsky reaction pathway, the electrons do not have to interact with H^+ at Ni surface to complete the charge transfer. Instead, it can directly interact with H^+ in the solution (Illustrated by Fig 38.b).

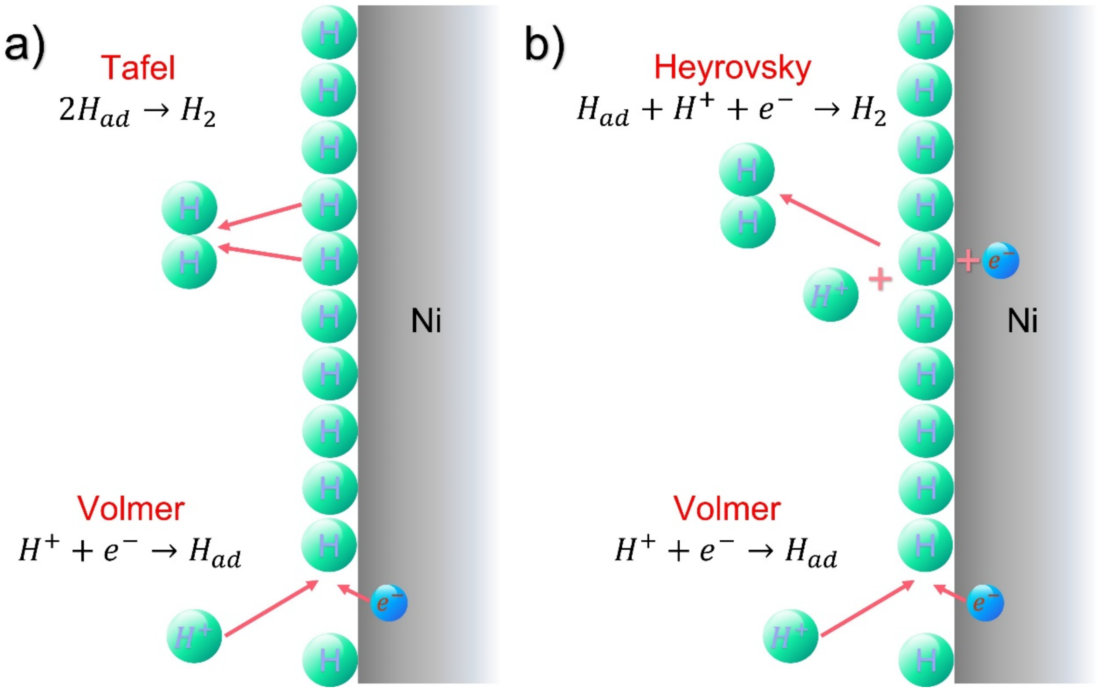

Figure 38: Hydrogen evolution reaction pathways: a. Volmer-Tafel; b. Volmer-Heyrovsky

After charge transfer, it will combine with another H atom to recombine into H_2 and escape, which does not require an open site on the Ni surface. This means hydrogen recombination rate and surface coverage will not limit the current. The current-potential behavior we observed is consistent with it so we propose this hydrogen surface coverage model follows the Volmer-Heyrovsky pathway for the hydrogen evolution reaction. The hydrogen surface coverage of our charging experiments is all very close to 1, which implies the charging is happening with almost full coverage of hydrogen and this again supports that the pathway should be Volmer-Heyrovsky.

Since the Ni surface is fully covered with hydrogen atoms, it is highly possible to form H-rich thin film such as Nickel hydride, Nickel hydroxide under cathodic charging. In fact, a recent study by Jiang et al reports the formation of Ni-O-S-H surface phases on the Ni samples and cathodic charging condition that is identical to what we present here. From Fig 26, we can estimate the hydrogen concentration when the Ni surface is under max H surface coverage is ~2000 a.ppm. Therefore, the corresponding surface H to Ni ratio can be calculated to be 4.5:1 and 72 H atoms/nm^3. Thus, this suggests the formation of a super stoichiometric hydride layer $NiH_{4.5}$. However, there are first principles DFT studies indicate that as the stoichiometric number of the Ni hydride NiH_x, x>1.25, the corresponding super stoichiometric Ni hydride will have higher energy than bare Ni (by up to 150kJ/mol, in the case of NiH_3)[49].

Such a high-energy Ni hydride phase is likely to undergo exothermic decomposition and form products with lower energy. Ni hydride is also reported to have a much higher electrical resistivity than pure Ni[59] while it usually is also an ion conductor[108]. Thus, the formation of such Ni hydride may require some H^+ ion to ingress through the already formed surface Ni hydride layer and participate in the Heyrovsky reaction at the Ni surface as this is a less resistive path compared to the reduction reaction at the surface of Ni hydride which needs electron coming through the hydride layer. So this raises one open question for future study, which is where does the charge transfer process actually occur at different H surface coverage. Although the Tafel slope analysis and derivation can yield theoretical prediction, direct experimental observation is also required to have a further understanding of the charge transfer mechanism.

Besides, as the ingress of the H^+ for the charge transfer process is a less electrical resistive pathway compared to the electron moving through the Ni hydride layer, the charge transfer resistance should reflect these changes. Therefore, further study on the charge transfer mechanism using EIS should be conducted. However, it is worth mentioning that the Ni hydride is unstable and likely to decompose and form other phases with lower energy which can result in some non-uniform distribution of these products covering the Ni hydride. This characteristic of the surface may complicate the interpretation of the EIS measurements, demanding some specialized analysis and measurement methods, such as the constant-phase-element (CPE) model by Brug *et al.*[70], or localized EIS microelectrodes capable of probing the local impedance [71]. Some other techniques based on EIS can also be considered, such as Mott-Schottky analysis for electrolyte/semiconductor junctions, which can provide insight into the electronic nature of the Ni hydride layer.

Our findings also suggest that there is a fundamental limit of adsorbed H atoms or H surface coverage at the Ni sample surface under an electrochemical aqueous environment which may eventually restrict the amount of hydrogen uptake into the Ni-based alloys. Therefore, there is a limit to the extent of HE or other H-induced properties degradation that Ni-based alloys may experience under a similar service environment. Such a limit of the adsorbed H atoms or H surface coverage is ultimately related to the recombination processes that consume the surface adsorbed H atoms to form molecular hydrogen and evolve, instead of diffusing into the metal. Thus, anything that can hinder such processes can increase the H surface coverage and may eventually increase H uptake. On the other hand, enhanced recombination processes would reduce H surface coverage and lower H uptake.

There are a number of groups VA and VIA elements that have been studied to be responsible for inhibiting the H recombination processes, enhancing hydrogen uptake, and are therefore termed as recombination poisons, such as P, As, S, Se, and Te[109-111]. However, the mechanism of such promoting H uptake action is still controversial, not fully understood, and appears to be little agreement on the effect of different elements. For example, Bockris[112] *et al.* studied the permeation rate of electrolytic hydrogen through Armco iron in an acidic and alkaline environment with the effect of cyanide, iodide, naphthalene, and nitrile using electrochemical permeation technique. They reported these compounds to inhibit the HER, increase the H permeation rate but decrease the H surface coverage. They attributed the enhanced H adsorption to the lower energy of $M\text{-}H_{ads}$ bonds and the inhibited H recombination and decreased H surface coverage to the preferential adsorption of those recombination poison on the metal surface that reduce the H adsorption and recombination sites. This proposed mechanism is followed by Dull and Nobe[113] on the study of other poisons on iron as well as the theoretical modeling and simulation by Conway and Jerkiewicz[114]. In a similar but slightly contradicted way, other researchers such as Dafft[81] *et al.* and Radhakrishnan[109] *et al.* reported enhanced H adsorption by the recombination poison due to the inhibition of the recombination reaction which results in higher H surface coverage that facilitates the H adsorption. H_2S is also a common recombination poison that has been studied extensively[109, 115]. While Frumkin[116] and Hickling[117] have used the electrochemical method to characterize cathodic Pt electrode and found that H_2S can decrease the $M\text{-}H_{ads}$ bonding energy and reduce the H surface coverage, a recent study by Fuji et al. showed that although H_2S can drastically improve the hydrogen adsorption, the surface H coverage remains unchanged.

In view of the above, despite the widely accepted fact that recombination poison can enhance the H uptake by inhibiting the recombination reaction, there is still no definite answer to how the poisons will affect the H surface coverage that determines the H uptake limit of the metals fundamentally. In addition, to the best of our knowledge, although there are a lot of the studies regarding the recombination effect on the H uptake rate, such as those mentioned above, there are few studies but the one by Newman and Shreir[118] that has attempted to determine the H uptake limit by saturating the steel sample with hydrogen in the solutions that containing recombination poison. They investigated the saturation solubility of hydrogen in steel in solutions containing various poisons such as S, P, Se, Te, and As and the hydrogen in steel after charging is determined by volumetric estimation based on vacuum extraction. They reported increased hydrogen saturation solubility after the addition of the recombination poisons. However, there is no direct evidence or procedure for guaranteed H saturation nor does the H measurement is adequately accurate. Coincidentally, these two aspects are exactly the strength of our experiments.

In addition to this, there are a number of papers on the study of the influence of alloy composition, microstructure, texture, and defects on H uptake of different metals. Take steels, which have been studied most extensively, as an example. It is reported by Hill and Johnson[119] that the solubility of steels increases with carbon content while other alloying elements such as Cr, Ni, Mo, Si and Cu are found to decrease the hydrogen uptake in iron alloys by Kim[120] *et al*. The hydrogen uptake kinetics of Mg have been shown to improve by reducing grain size and introducing defects of the materials which enable shorter and faster diffusion pathways[121, 122]. Nevertheless, the study of the influence of the above factors on the H uptake is still deficient for Ni and Ni-based alloys, not to mention being systematic. Similar to the studies of recombination poison on the H uptake, the above mentioned studies on H uptake are largely rely on electrochemical permeation methods to characterize the H uptake, which is not ideal for determining the limit of H uptake when comparing to the H saturation charging and direct H content measurement.

Therefore, further investigation into not only the effect of hydrogen recombination poison but also composition, microstructure, texture, and defects on the H uptake limit of cathodically charged Ni-based alloys using accurate hydrogen content determination and saturation H charging like the ones we employed for our experiments is of great interest. It can enable us to better modify the materials to accommodate different needs, from corrosion-resistant applications to H storage applications. This can also be very helpful to further understand the HE susceptibility of these corrosion-resistant alloys and can lead to new strategies when applying cathodic protection to those metals that are in service.

Our proposed mechanism for the HER and H uptake behavior all suggests the existence of an atomic scale thick, superstoichiometric Ni hydride layer at the Ni sample surface during the charging process. Based on the removal of the film via ultrasonication, we also believe that the film is rather fragile and maybe only metastable in the air. Therefore, a fast and Non-vacuum characterization technique is needed to study the thin film. Priority among priorities is how to find and characterize the thin film. Due to its composition are mainly hydrogen, which is very small that common surface characterization technique such as XPS is not capable of characterizing. Neutron reflectometry can be a suitable tool for this interface characterization[57, 123-125] since neutron will interact with the nucleus of hydrogen, not with electrons, which will give a fair strong enough signal even with nickel as substrate. It has angstrom-level depth resolution which is also ideal to detect such a thin film. Due to the high penetrability of neutrons through various materials and media, it is very suitable for *in situ* studies[57]. Therefore, neutron scattering measurement during in situ hydrogen charging will be a very viable option. XRD, due to its fast scan ability and easy sample preparation, is another promising characterization technique to study the thin film at the Ni surface under cathodic charging.

Finally, some other materials, including Ni-base engineering alloys such as Inconel 718, 725 may also be used for future study. Since these alloys are typically designed to resist corrosion, understanding their property and hydrogen uptake behavior under cathodic charging can further improve the development and utilization of corrosion-resisted alloys. These materials have different compositions and microstructures that may affect the surface HER mechanism. For example, the tetrahedral site in the Ni fcc lattice has a site to lattice point ratio of 2:1 while the octahedral site is 1:1. Thus, different microstructures of the sample may result in various combinations of different hydrogen interstitial sites that can eventually affect the maximum H surface coverage as well as the HER mechanism.

5. LOCALIZED CORROSION INITIATION AT NI SURFACE UNDER CATHODIC CHARGING

5.1 Introduction

Cathodic charging is an electrochemical process in that electrons have been driven to flow towards the sample surface and exit from the surface into the electrolyte. This characteristic enables the reduction reaction occurs on the cathode that the surface is being protective globally against corrosion, which is essentially an oxidation reaction process that the electrons are being taken away from the sample. Therefore, it is a common understanding that samples under cathodic charging should be protected against corrosion macroscopically. However, many studies are reporting the observation of localized corrosion under cathodic polarization[21, 126-129], with the work by Liu et.al.[15] being the most recent and relevant one to the condition in this study. These corrosion features are mainly crevice or pitting, which are common localized corrosion types. In our study, we present an experimental observation and investigation on the localized corrosion pittings on Ni surface under cathodic charging. The initiation of the localized corrosion pitting is found to be related to the full coverage of the surface phases as well as the change of the semiconductor behavior with increasing overpotential.

5.2 Methods

The Ni samples are the same 50 μm thick pure Ni foils used in the studies introduced previously. The surface remains unpolished with a surface roughness of ~100nm. The cathodic chargings under constant overpotential are consist of various overpotential (350mV, 400mV, 450mV, 500mV, 525mV, 550mV and 600mV) and different charging time (6hr, 12hr, 18hr). The way to keep constant overpotential has been introduced previously in chapter 2.

To retain the surface phases intact and assess the evolution of surface phase coverage, the charged samples were only gently dried without ultrasonicate after extraction from the electrolyte and before the characterization.

The SEM observations and EDS measurements were all performed using the LYRA FIB-SEM. EDS measurement is similar to the measurement introduced in chapter 3, focusing on the O and S maps to determine the coverage of the surface phases. However, in order to make EDS maps across different charging conditions to be signal quantitatively comparable, all EDS map scanning time is 30 mins and all the other parameters were set to be identical.

The coverage of the surface phases was determined by conducting image processing of the O and S maps from the EDS. The raw output of the O and S maps from the EDS instrument consists of corresponding element signal counts at each scanning point, representing the elemental distribution and abundance. This data was imported into image J and converted into a binary map with a 0-256 intensity range. The same threshold was used to distinguish the surface phases from Ni substrate based on the converted elemental signal intensity. By doing so, the surface phase coverage across different overpotentials and charging time can then be determined with a uniform standard, which is essential for direct comparison.

Mott-Schottky measurements were conducted at different times of the charing (0h, 8h, 18h, 28h) at the same Ni sample that has been charged under 600mV overpotential. The scanning frequency of the Mott-Schottky analysis is 1000Hz with an amplitude of 10mV. The DC scanning potential range is from 100mV.

5.3 Results

5.3.1 SEM observation of surface changes on Ni surface after cathodic charging.

Figure 35 shows the SEM images of a) as-received Ni surface and b) Ni surface after 48 hours of charging at 500mV overpotential. The as-received Ni surface exhibits some directional small scratches with ~5 μm in width, which possibly originate from the manufacturing process. The darker regions should be the carbon-containing surface contaminant.

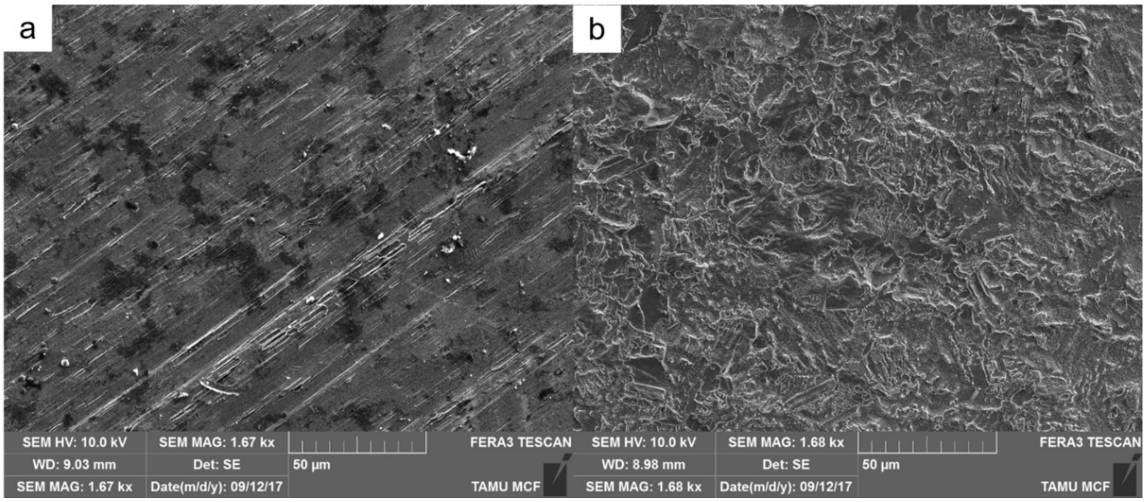

Figure 39: Change of surface condition before and after charging captured by SEM. a) As-received surface of the nickel foil before charging. b) The surface of the nickel foil after 24 hours of charging at 500mV overpotential.

The surface of the Ni foil after 48 hours charging under 500mV overpotential appears to be much rougher compared to the as-received one. The curly, filiform features at the surface should be the surface phases introduced in chapter 3, albeit additional surface characterizations are needed for confirming the features are those Ni-OSH surface phases.

By comparison of figure 39 a) and b), cathodic hydrogen charging, especially at high overpotential and for a long time, changes the surface topography of the sample to be very rough and therefore increase the active surface area, which is accountable for the change of open circuit potential (OCP) shown in figure 2.

5.3.2 SEM observation of Ni surface with localized corrosion pitting.

Figure 40 a) shows the surface of a Ni sample after 6 hours of charging under 600mV overpotential. The surface does not exhibit features similar to figure 39, which appears to be curly and filamentary. Instead, the surface looks more like it consists of many exposed crystal facets with various orientations. There are no features that appear to be distinct from Ni but attached to the Ni surface. Figure 40 b) is the zoom-in section of figure 40 a) which is highlighted by the red circle. It shows a cavity-like pitting with facet-like inner faces. The facet-like inner faces suggest that the localized corrosion pitting appears to be in a junction of several grains with different orientations. The inclusion inside the pitting has a shape similar to an octahedron with a diameter of around 5μm.

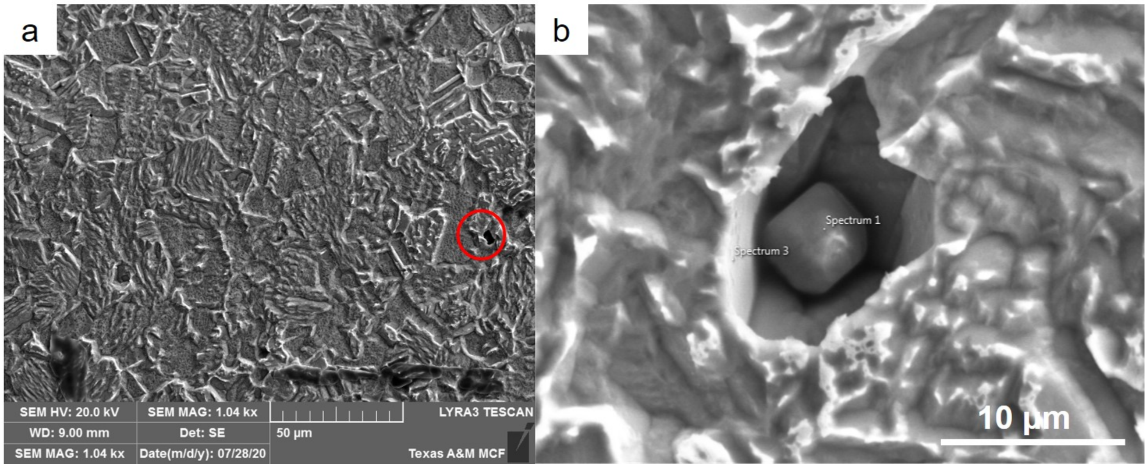

Figure 40: Change of surface condition before and after charging captured by SEM. a) As-received surface of the nickel foil before charging. b) The surface of the nickel foil after 24 hours of charging at 500mV overpotential.

5.3.3 EDS maps of Ni surface with localized corrosion pitting

Figure 41 a) is an EDS layered map with Ni, O, S maps overlayed. We can see the charged Ni surface consists primarily of Ni. The O, S concentrated area only takes a small portion of the surface. Many corrosion pittings similar to the one in figure 40 b) were highlighted by the white circles. These corrosion pittings tend to locate away from the O and S-rich filament based on the Ni, O, and S maps. The surface phases coverage is ~ 10% determined by the image processing method introduced in the methods section.

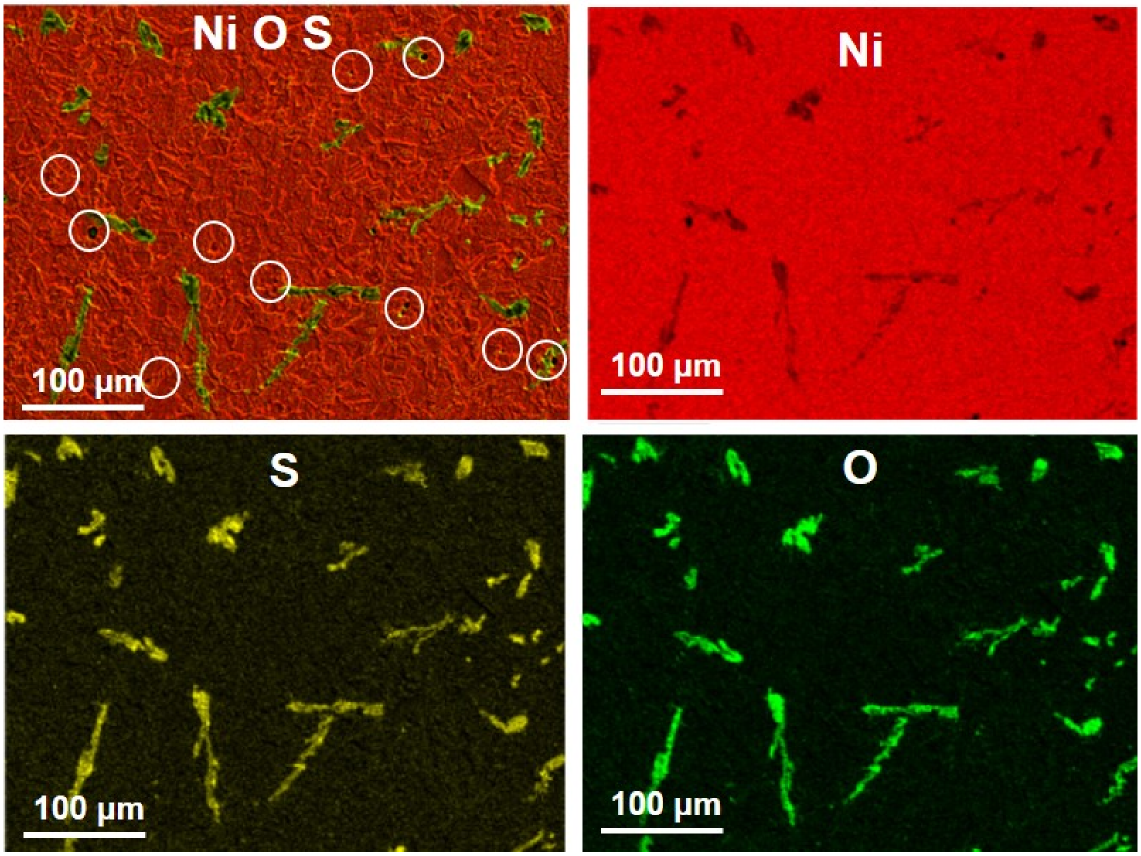

Figure 41: EDS mapping of the Ni sample surface with corrosion pitting under 600 mV overpotential.

5.3.4 EDS maps of impurity inclusion inside corrosion pitting

Figure 42 shows the EDS maps of the impurity inclusion inside the corrosion pitting. The surrounding of the corrosion pitting consists primarily of Ni albeit with evidence of some S and O surface impurities. The Ni and S maps show that there is no Ni and S content inside the pitting while the O and Al maps indicate that the inclusion inside the pitting is rich in O and Al. A point spectrum scan right on the inclusion yields a composition with 51.7 at% in O, 34.2 at% in Al, 14.2 at% in Ni. Therefore, the impurity inclusion inside the corrosion pitting should consist primarily of some Al-oxides.

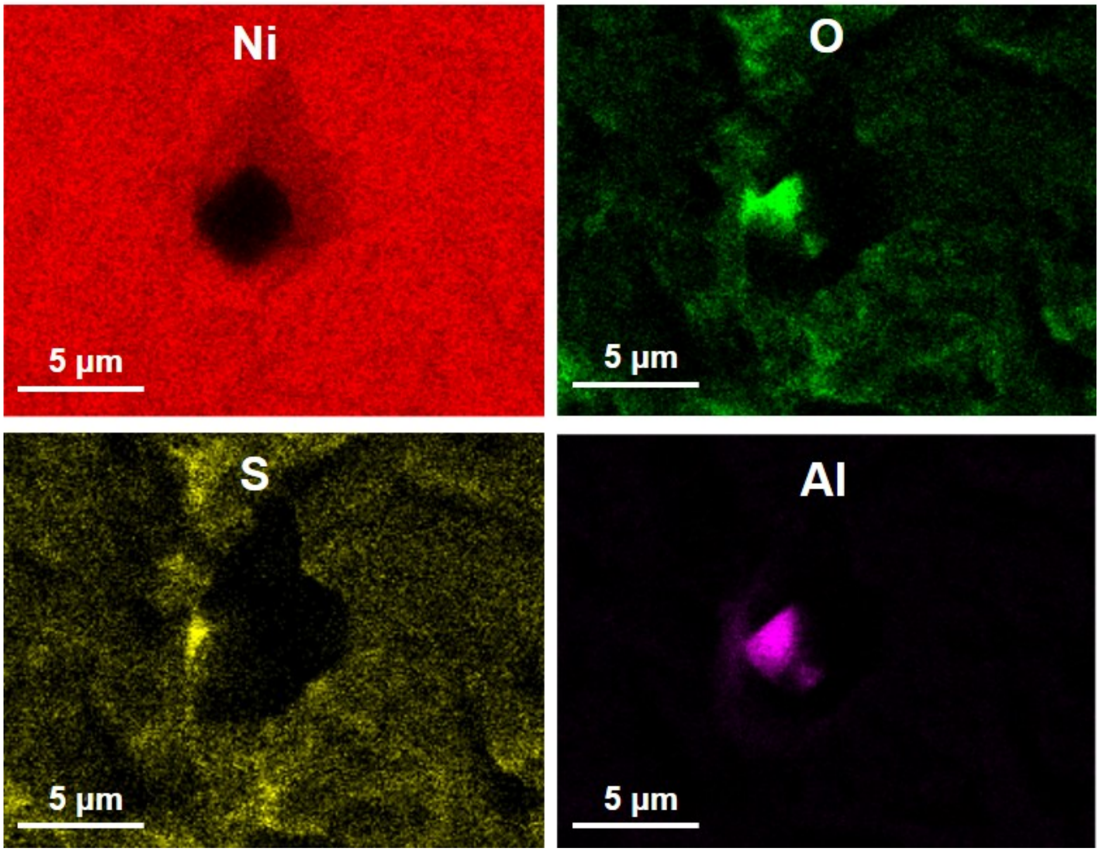

Figure 42: EDS mapping of the impurity inclusion inside the corrosion pitting that formed under 600 mV overpotential.

5.3.5 Evolution of surface phases coverage based on EDS measurements

To investigate how surface phases coverage varies with charging overpotential, a series of EDS measurements on Ni samples that have been charged for the same amount of time (16 hrs) but under different overpotentials were conducted. Using the image processing method introduced previously in the method section, we can obtain the binary maps that distinguish surface phases from surrounding Ni substrate, which is demonstrated by figure 43.

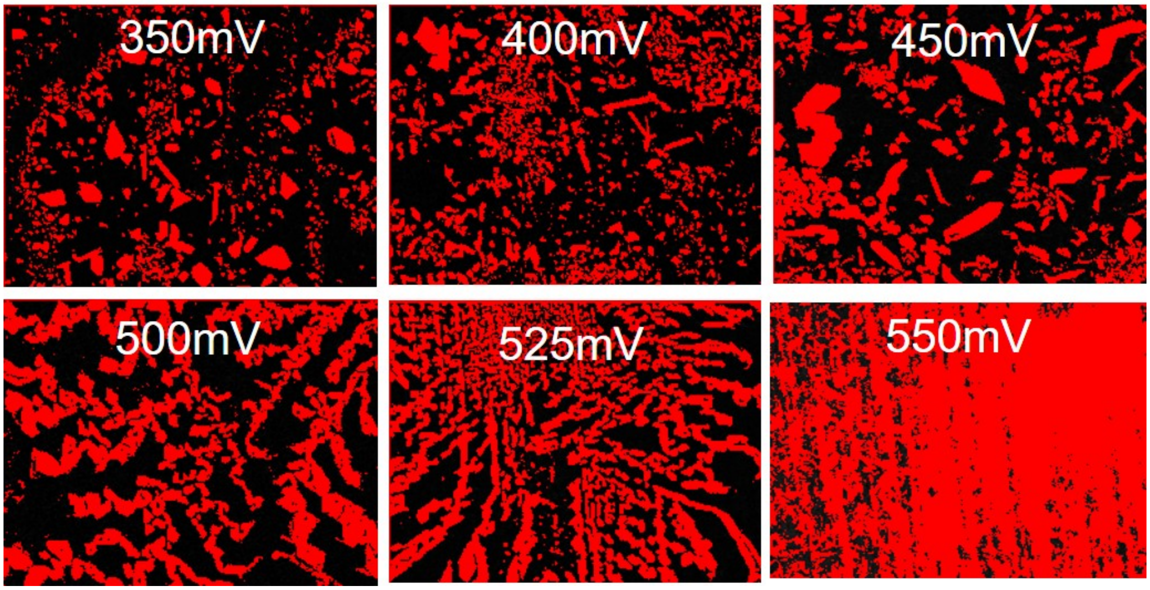

Figure 43: Binary maps of surface phases over Ni substrate determined by EDS at various overpotentials.

We can see the surface phases start from rather dispersive, fragmented distribution at low overpotential, gradually changing to a more connected, filiform-like with increasing overpotential. It finally appears to coalesce and reaches almost full surface coverage beyond 550 mV overpotential.

Figure 44 shows the plot of surface phases coverage vs charging overpotential. From figure 44, we can clearly see that the surface phases coverage, starts at ~20%% under 350 mV overpotential, monotonically increases with increasing overpotential. There is a significant increase in coverage beyond 525 mV overpotential to ~80%. Coverage of 600 mV is not shown here as the charging process was interrupted due to the current surge after just 6 hours of charging, which makes the coverage value not comparable to the other data.

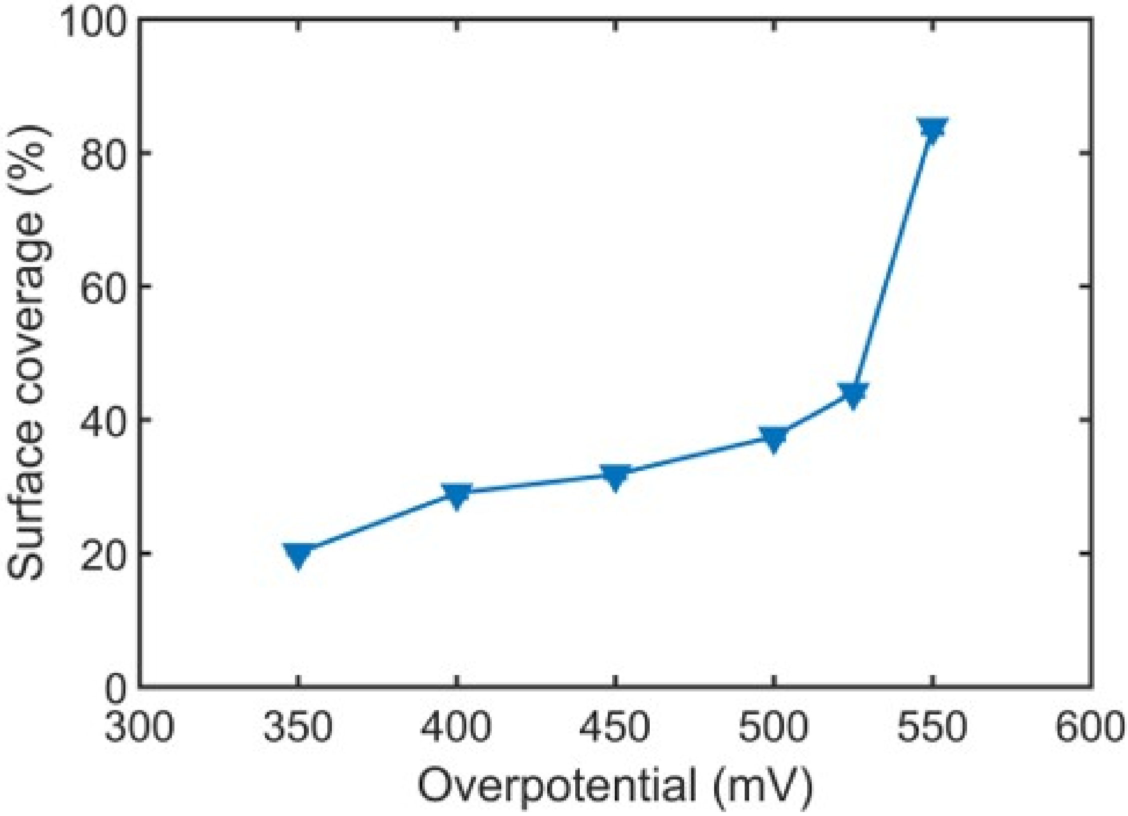

Figure 44: Surface phases coverage vs charging overpotential.

5.3.6 Charging current surge of Ni sample under 600 mV overpotential charging

When the Ni samples are under cathodic charging, the current/current density will take up to 5 hours to get stabilized, which corresponds to the stabilization of the surface condition as the driven steady-state of the surface phases has been achieved, as illustrated by figure 45 a). However, the current behavior of the 600 mV overpotential charging that has the localized corrosion pitting initiated behaves differently. Figure 41 b) shows that the current of the 600 mV charging increased monotonically with charging time and finally exceeded the current limitation of the potentiostat and interrupted the charging.

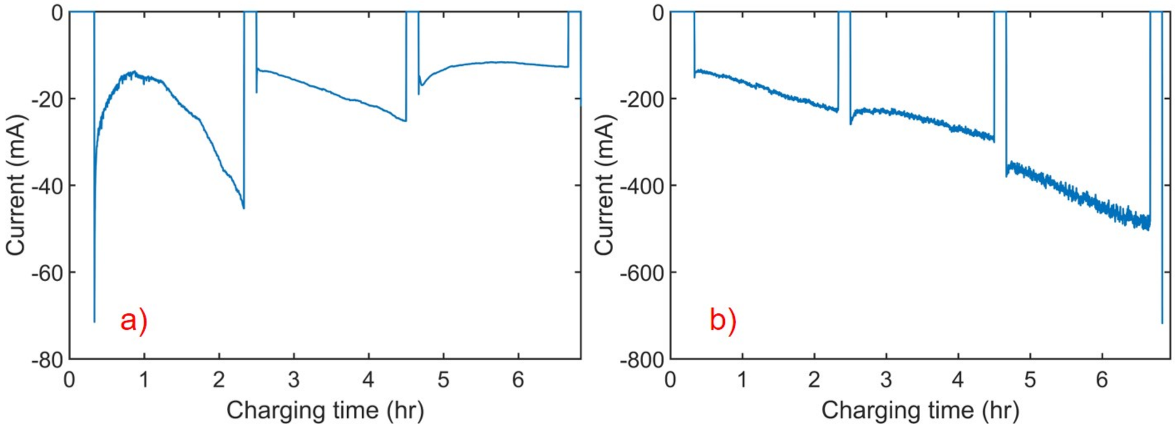

Figure 45: Comparison of the current history of a) 400mV overpotential charging and b) 600mV charging that has localized corrosion pitting formed.

5.3.7 Mott-Schottky analysis of Ni sample under 600 mV overpotential charging

Mott-Schottky analysis was conducted to investigate the evolution of electronic properties of the surface phases under 600mV constant overpotential charging. Here we choose a sample with a much smaller surface area to make sure the total current will not exceed the current limit of the potentiostat and interrupt the charging. The Mott-Schottky measurements were conducted on the same sample at different charging times. Figure 46 shows the corresponding Mott-Schottky plot. By fitting the curves and determining the slope, the type of the semiconductor behavior can then be obtained. The negative slope represents the P-type semiconductor and the positive slope suggests the N-type semiconductor. Figure 42 indicates that regardless of the variation of $1/C^2$ among different charging times, the turning points of the curves are all around -150 mV vs SCE. This suggests that there is a switching of semiconductor behavior at some characteristic potential around ~-150 mV vs SCE.

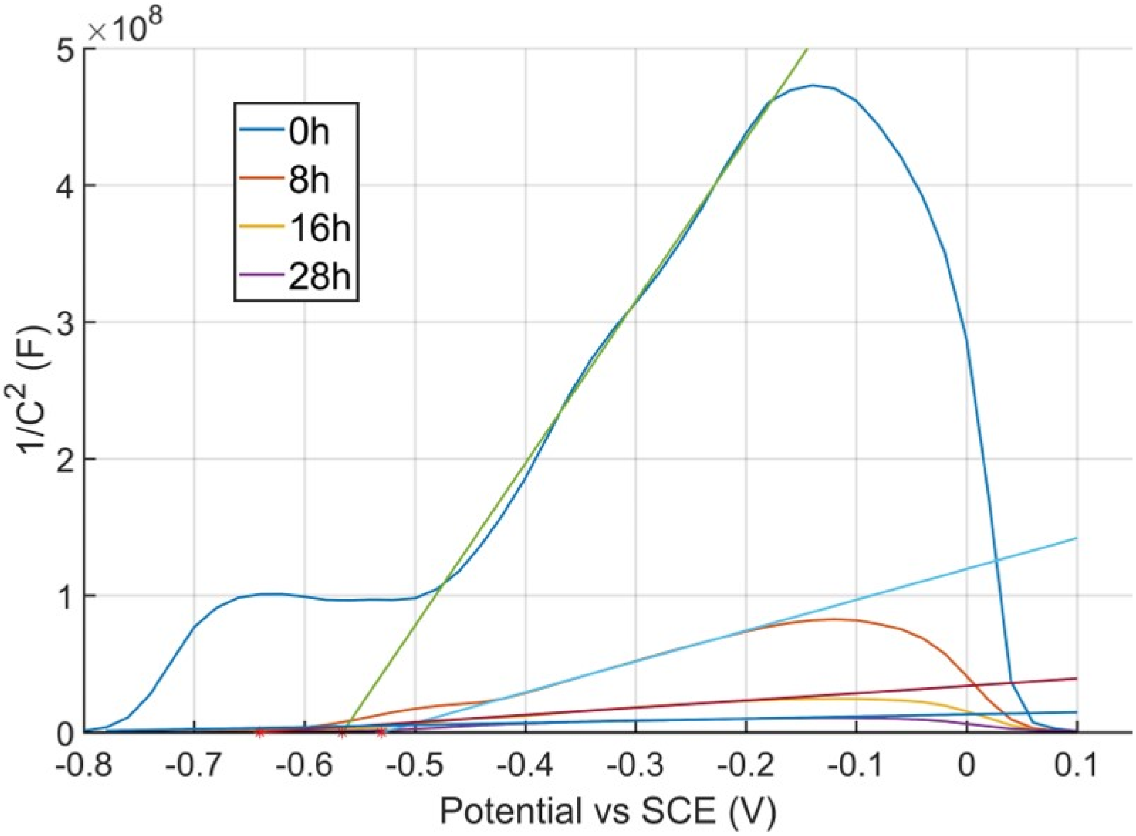

Figure 46: Mott-Schottky plots of 600mV overpotential charging at various charging times.

Further analysis of the Mott-Schottky plot yields the N-type donor density, which is determined based on the slope of the lines that fit the curves. Figure 47 shows the N-type donor density vs charging time. The N-type donor density increases monotonically with charging time, by ~2500% after 24 hours of charging. This suggests that the defect increases dramatically inside the surface phases as the charging time increases.

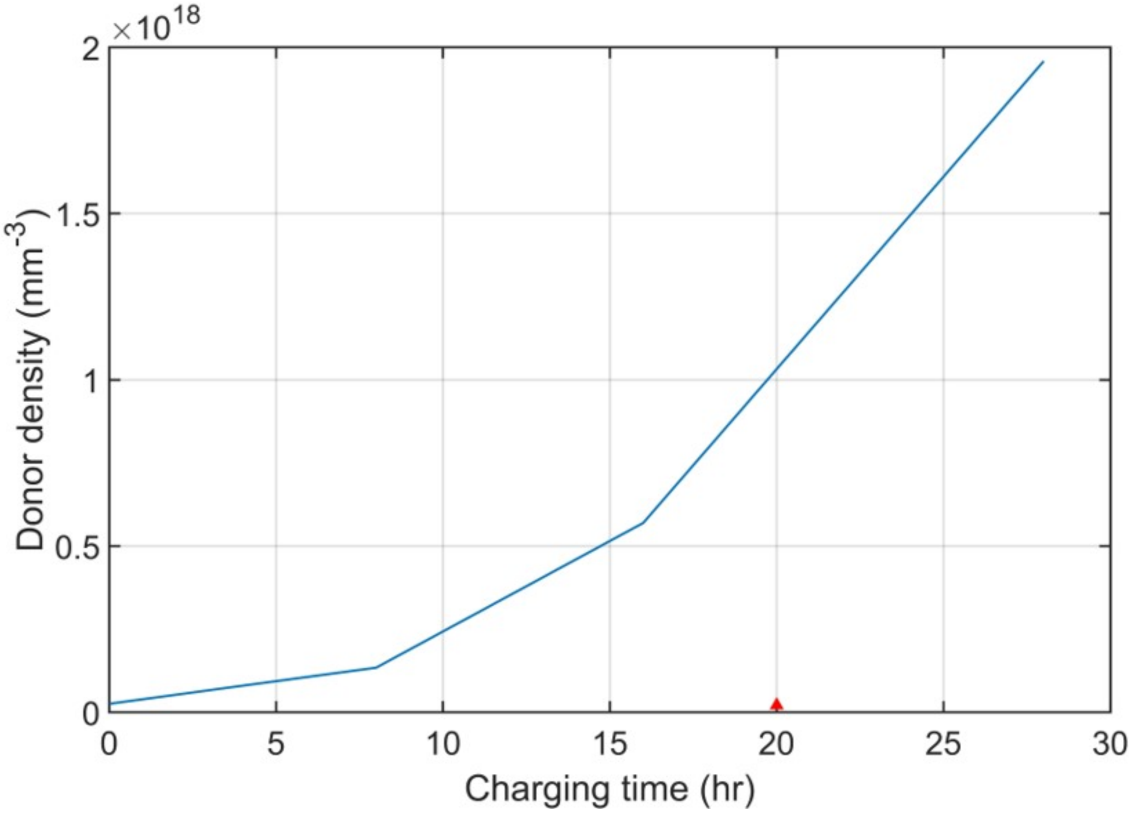

Figure 47: N-type donor density determined from Mott-Schottky analysis vs charging time of 600mV overpotential charging.

5.4 Discussion

In this work, we demonstrate the observation of localized corrosion pitting on Ni surface under 600 mV overpotential cathodic charging. Our measurements show that the localized corrosion pitting appears to be distributed away from the Ni-OSH surface phases introduced in chapter 3. The inclusion particles that were located preferentially inside the corrosion pitting were also observed. Further characterization by EDS indicates that the inclusion particles consist primarily of Al and O. There are several possible sources for the Al impurity, including electrolyte impurities, Ni foil impurities, and impurities introduced by the sealing epoxy. Based on the EDS maps that with these corrosion pitting being captured, the weight percentage of the Al to the Ni sample can then be estimated. Given that there are ~15 pits per 2.5×10^6 um^3, assuming pit depth is ~10 μm by eyeballing and treating particles inside as octahedron that has edges of 4 μm in length, we can calculate the volume of such Al inclusion to be 450 um^3 per 2.5×10^6 um^3. After taking Al density and Ni density into consideration, we can get the Al wt% to be ~0.002 wt%, which is much less than the remaining undetermined composition of the Ni foil. This suggests that the Al impurities possibly originate from the Ni foil. SIMS depth profiling should be conducted to provide direct and accurate information to validate such a hypothesis.

Another source can be the electrolyte. However, ICP-MS measurements were conducted for the electrolyte composition, and no Al was detected. Since the ICP-MS detection limit is 0.005 μg/L, we can confidently eliminate the possibility of Al impurity from the electrolyte.

The last possibility can be from the sealing epoxy, as the composition information provided by the supplier shows that it contains metal oxides, even though the specific composition is not given. ICP-MS measurement of the same amount of sealing epoxy immersed into fresh electrolyte for 24 hours yields an Al concentration of ~1000 ng/ml, which is a significant increase compared to the baseline of fresh electrolyte alone, which is 7 ng/mL. Therefore, a more detailed investigation should proceed such as using XPS for Al composition determination, to validate this hypothesis.

The initiation of the corrosion pitting is reported to be related to inclusions such as Al demonstrated here or other second phases particles[130, 131]. Such inclusions or secondary phase particles can cause high local discontinuity and therefore, weaken the surface passive film, either by reducing the thickness or generating localized stress. Additionally, the point defect model[132] proposed by D. D Macdonald, which has been widely used for explaining pitting formation and localized corrosion, is based on two important assumptions. The first one is the termination of film growth due to the cation vacancies generate and condense at the metal-film layer interface. This suggests the defect density at the location where pitting initiates can increase significantly, which is consistent with the findings of our Mott-Schottky measurement and analysis. Although the Mott-Schottky measurement is conducted on the whole sample surface, not the locale associated with corrosion pitting. Therefore, more localized or *in situ* investigation regarding this matter should be considered and conducted in the future.

The second important assumption of the model is that the passive film is continuously dissolving, either due to its thermodynamic instability or local pH change. This is consistent with our conditions and findings. Therefore, localized pH measurement could provide useful information regarding this assumption.

From the Mott-Schottky measurement and analysis, we not only know that the semiconductor behavior of the surface phases changes from more corrosion-resistive P-type to more corrosion susceptible N-type but also confirm that the donor density also increases dramatically with increasing charging time. The P-type is more corrosion-resistive simply due to the fact that it mainly contains defects that prevent cations from migrating from the metal substrate and penetration of harmful anions like Cl^-. The N-type as being corrosion-susceptible, performing the exact opposite. As a result, the higher the

N-type donor density it is, the weaker the surface phases is against film dissolution and breakdown. Therefore, both the semiconductor type and its donor density suggest that the surface phases are becoming more and more susceptible to film dissolution and breakdown, which exposes the bare Ni surface to the electrolyte. This combines with the Al impurities inclusion gives the necessary but insufficient condition for localized pitting initiation.

Further investigation based on Mott-Schottky analysis should also be performed to further understand how the electronic properties of the surface phases evolve not only with charging time but also with overpotential. Such as performing Mott-Schottky measurement on samples under different overpotentials, interpreting surface phases thickness by conducting further Mott-Schotty analysis.

6. SUMMARY AND FUTURE WORK

In this dissertation, the surface structure evolution and H uptake behavior of Ni under cathodic charging have been investigated. The localized corrosion initiation at N surface under cathodic charging has also been observed and investigated as a side discovery during the study of the first two parts. The first chapter gives a review of the current understanding of cathodically charged metal surfaces, with a focus on Ni. The second chapter introduces various characterization techniques that are useful and essential to the study of Ni under cathodic charging. The third chapter reported the observation and further investigation of new surface phases that possess distinct crystallographic structure from Ni under cathodic charging using complementary characterization techniques along with 2D XRD. The fourth chapter consists of the studies of the H uptake as well as the evolution of the HER pathway under cathodic charging. The last chapter gives a brief introduction and investigation of the localized corrosion features that initiated on the Ni surface under cathodic charging.

The study on surface phases successfully observed some previously un-noticed surface phases that are ~ 70mV more cathodic to the surrounding Ni surface, rich in Ni, O, S, and H with nm scale thickness. These phases are found to be thermodynamically unstable under cathodic polarization in an acidic aqueous environment that they are in a driven steady state in which the rate of formation and dissolution equal. A phase formation mechanism that these phases are likely the decay product of oxidation reaction that surface Ni hydride reacting with the electrolyte.

The H uptake study was conducted with its primary goal of seeking indirect evidence of surface hydride that resulting in the formation of the surface phases. We successfully charged the Ni samples to the equilibrium state of H and confirming that the Ni surface is reaching full H surface coverage under cathodic charging, which indicates that Ni surface hydride can form under such conditions. Additionally, by performing electrochemical measurements along with Tafel analysis, the switching of HER pathway from Volmer-Tafel to Volmer Heyrovsky with increasing overpotential and surface H coverage has also been confirmed. This explains the un-restricted current density behavior when there is full H surface coverage.

The investigation of localized corrosion suggests that localized corrosion pitting is likely to occur as the surface phases reach full surface coverage. Surface characterizations show that some Al-rich impurities inclusions are preferentially located inside the corrosion pitting sites and the pitting features exhibit crystal facets look. Corresponding Mott-Schottky analysis indicates that the semiconductor behavior of the surface phases changes from P-type to less corrosion-resistive N-type with increasing overpotential. Further analysis shows that the N-type donor density increases with increasing overpotential, which results in the surface phases layer more susceptible to dissolution and breakdown.

Several directions are proposed here as the future study to improve the current understanding and connect all the above-mentioned findings to a whole. First is the investigation of the direct evidence of surface hydride, and neutron reflectometry is one of the few promising techniques that are capable. The second one is performing more *in situ* localized surface characterization to capture the localized transient and interactions at the Ni surface. Some of the techniques include but are not limited to S-VET, localized EIS, and *in situ* KPFM. This can further improve the understanding of surface phase formation as well as localized corrosion initiation.

REFERENCES

1. Boniszewski, T.; Smith, G. C., A NOTE ON NICKEL HYDRIDE. *Phys. and Chem. Solids* **1961**, Medium: X; Size: Pages: 115-18.

2. J.W. Cable, E. O. W., W.C. Koehler, The crystal structure of nickel hydride. *Journal de Physique* **1964,** *25* ((5)), 460.

3. Endoh, E.; Otouma, H.; Morimoto, T., Advanced low hydrogen overvoltage cathode for chlor-alkali electrolysis cells. *International Journal of Hydrogen Energy* **1988,** *13* (4), 207-213.

4. Divisek, J.; Mergel, J.; Schmitz, H., Advanced water electrolysis and catalyst stability under discontinuous operation. *International Journal of Hydrogen Energy* **1990,** *15* (2), 105-114.

5. Ansari, N.; Balasubramaniam, R., Determination of hydrogen diffusivity in nickel by subsurface microhardness profiling. *Materials Science and Engineering: A* **2000,** *293* (1), 292-295.

6. Lawrence, S. K.; Somerday, B. P.; Ingraham, M. D.; Bahr, D. F., Probing the Effect of Hydrogen on Elastic Properties and Plastic Deformation in Nickel Using Nanoindentation and Ultrasonic Methods. *JOM* **2018,** *70* (7), 1068-1073.

7. Watson, J. W.; Meshii, M.; Shen, Y. Z., Effect of cathodic charging on the mechanical properties of aluminum. *Metallurgical Transactions A* **1988,** *19* (9), 2299-2304.

8. Bond, G. M.; Robertson, I. M.; Birnbaum, H. K., Effects of hydrogen on deformation and fracture processes in high-ourity aluminium. *Acta Metallurgica* **1988,** *36* (8), 2193-2197.

9. Elhoud, A. M.; Renton, N. C.; Deans, W. F., Hydrogen embrittlement of super duplex stainless steel in acid solution. *International Journal of Hydrogen Energy* **2010,** *35* (12), 6455-6464.

10. Domżalicki, P.; Lunarska, E.; Birn, J., Effect of cathodic polarization and sulfate reducing bacteria on mechanical properties of different steels in synthetic sea water. *Materials and Corrosion* **2007,** *58* (6), 413-421.

11. Panagopoulos, C. N.; El-Amoush, A. S.; Georgarakis, K. G., The effect of hydrogen charging on the mechanical behaviour of α-brass. *Journal of Alloys and Compounds* **2005,** *392* (1-2), 159-164.

12. Panagopoulos, C.; Papapanayiotou, P., THE INFLUENCE OF CATHODIC HYDROGEN CHARGING ON THE MECHANICAL-BEHAVIOR OF AL-4ZN-1MG ALLOY. *Journal of Materials Science* **1995,** *30* (13), 3449-3456.

13. Birnbaum, H. K., Mechanical properties of metal hydrides. *Journal of the Less Common Metals* **1984,** *104* (1), 31-41.

14. Thodla, R., Environmentally Assisted Cracking of High Strength Nickel Based Alloys Under Cathodic Protection. In *CORROSION 2018*, NACE International: Phoenix, Arizona, USA, 2018; p 13.

15. Liu, M.; Seita, M.; Duong, T.; Kuo, W. C. H.; Demkowicz, M. J., Preferential corrosion of coherent twin boundaries in pure nickel under cathodic charging. *Physical Review Materials* **2019,** *3* (6), 063606.

16. Juškenas, R.; Selskis, A.; Kadziauskien≐, V., In situ X-ray diffraction investigation of nickel hydride formation during cathodic charging of Ni. *Electrochimica Acta* **1998,** *43* (12), 1903-1911.

17. Rashkov, S.; Monev, M.; Tomov, I., Electrochemical formation and disintegration of the Ni H phase in bright nickel coatings. *Surface Technology* **1982,** *16* (3), 203-208.

18. Shizuku, Y.; Yamamoto, S.; Fukai, Y., Phase diagram of the Ni–H system at high hydrogen pressures. *Journal of Alloys and Compounds* **2002,** *336* (1), 159-162.

19. Song, G.; Atrens, A.; Dargusch, M., Influence of microstructure on the corrosion of diecast AZ91D. *Corrosion Science* **1998,** *41* (2), 249-273.

20. Chen, J.; Dong, J.; Wang, J.; Han, E.; Ke, W., Effect of magnesium hydride on the corrosion behavior of an AZ91 magnesium alloy in sodium chloride solution. *Corrosion Science* **2008,** *50* (12), 3610-3614.

21. Williams, G.; Neil McMurray, H., Localized Corrosion of Magnesium in Chloride-Containing Electrolyte Studied by a Scanning Vibrating Electrode Technique. *Journal of The Electrochemical Society* **2008,** *155* (7), C340.

22. Gong, M.; Wang, D.-Y.; Chen, C.-C.; Hwang, B.-J.; Dai, H., A mini review on nickel-based electrocatalysts for alkaline hydrogen evolution reaction. *Nano Research* **2016,** *9* (1), 28-46.

23. Safizadeh, F.; Ghali, E.; Houlachi, G., Electrocatalysis developments for hydrogen evolution reaction in alkaline solutions – A Review. *International Journal of Hydrogen Energy* **2015,** *40* (1), 256-274.

24. Popczun, E. J.; McKone, J. R.; Read, C. G.; Biacchi, A. J.; Wiltrout, A. M.; Lewis, N. S.; Schaak, R. E., Nanostructured Nickel Phosphide as an Electrocatalyst for the Hydrogen Evolution Reaction. *Journal of the American Chemical Society* **2013,** *135* (25), 9267-9270.

25. Bockris, J. O. M.; Potter, E. C., The Mechanism of Hydrogen Evolution at Nickel Cathodes in Aqueous Solutions. *The Journal of Chemical Physics* **1952,** *20* (4), 614-628.

26. Kimura, A.; Birnbaum, H. K., Hydrogen induced grain boundary fracture in high purity nickel and its alloys—Enhanced hydrogen diffusion along grain boundaries. *Acta Metallurgica* **1988,** *36* (3), 757-766.

27. Rettew, R. E.; Thodla, R., Corrosion of Nickel Alloys in Elevated Temperature Sour Gas Environments. In *CORROSION 2017*, NACE International: New Orleans, Louisiana, USA, 2017; p 9.

28. Klapper, H. S.; Klöwer, J.; Gosheva, O., Hydrogen embrittlement: the game changing factor in the applicability of nickel alloys in oilfield technology. *Philosophical Transactions of the Royal Society A: Mathematical, Physical and Engineering Sciences* **2017,** *375* (2098), 20160415.

29. Kim, S.-J.; Jang, S.-K.; Kim, J.-I., Electrochemical study of hydrogen embrittlement and optimum cathodic protection potential of welded high strength Steel. *Metals and Materials International* **2005,** *11* (1), 63-69.

30. Tavakoli, B. A.; Shimpalee, S.; Weidner, J. W.; Garcia-Diaz, B. L.; Martinez-Rodriguez, M. J.; Olson, L. C., The Effect of Nickel Alloy Corrosion Under Cathodic Protection inside High Temperature Molten Salt Systems. *Meeting Abstracts* **2016,** *MA2016-01* (15), 971.

31. Rudolf, P. R., 2-DIMENSIONAL X-RAY-DIFFRACTION AND SCATTERING OF MICROCRYSTALLINE AND POLYMERIC MATERIALS. *Spectroscopy* **1994,** *9* (6), 22.

32. He; Bob, B.; Preckwinkel, U.; Smith, K., Fundamentals of two-dimensional X-ray diffraction (XRD2). *Advances in X-ray Analysis* **2000,** *43*, 8.

33. Verkhoturov, S. V.; Eller, M. J.; Rickman, R. D.; Della-Negra, S.; Schweikert, E. A., Single Impacts of C60 on Solids: Emission of Electrons, Ions and Prospects for Surface Mapping. *The Journal of Physical Chemistry C* **2010,** *114* (12), 5637-5644.

34. Takano, N.; Kaida, S., Crack Initiation by Cathodic Hydrogen Charging in Nickel Single Crystal. *ISIJ International* **2012,** *52* (2), 263-266.

35. Abrams, H., Grain size measurement by the intercept method. *Metallography* **1971,** *4* (1), 59-78.

36. Coelho, A., TOPAS and TOPAS-Academic: an optimization program integrating computer algebra and crystallographic objects written in C++. *Journal of Applied Crystallography* **2018,** *51* (1), 210-218.

37. Eller, M. J.; Verkhoturov, S. V.; Schweikert, E. A., Testing Molecular Homogeneity at the Nanoscale with Massive Cluster Secondary Ion Mass Spectrometry. *Analytical Chemistry* **2016,** *88* (15), 7639-7646.

38. Latanision, R. M.; Kurkela, M., Hydrogen Permeability and Diffusivity in Nickel and Ni-Base Alloys. *CORROSION* **1983,** *39* (5), 174-181.

39. Lee, K. A.; McLellan, R. B., The diffusivity of hydrogen in nickel at low temperatures. *Scripta Metallurgica* **1984,** *18* (8), 859-861.

40. Seita, M.; Hanson, J. P.; Gradečak, S.; Demkowicz, M. J., Probabilistic failure criteria for individual microstructural elements: an application to hydrogen-assisted crack initiation in alloy 725. *Journal of Materials Science* **2017,** *52* (5), 2763-2779.

41. Li, J.; Oudriss, A.; Metsue, A.; Bouhattate, J.; Feaugas, X., Anisotropy of hydrogen diffusion in nickel single crystals: the effects of self-stress and hydrogen concentration on diffusion. *Scientific Reports* **2017,** *7* (1), 45041.

42. Schneider, C. A.; Rasband, W. S.; Eliceiri, K. W., NIH Image to ImageJ: 25 years of image analysis. *Nature Methods* **2012,** *9* (7), 671-675.

43. Baggio, S.; Becka, L. N., A reinvestigation of the structure of nickel sulphite hexahydrate, NiSO3.6H2O. *Acta Crystallographica Section B* **1969,** *25* (6), 1150-1155.

44. Hall, D. S.; Bock, C.; MacDougall, B. R., The Electrochemistry of Metallic Nickel: Oxides, Hydroxides, Hydrides and Alkaline Hydrogen Evolution. *Journal of The Electrochemical Society* **2013,** *160* (3), F235-F243.

45. Yoshio, S.; Maki, K., Computational modeling of the effect of varying aqueous solutions on Ni(OH)2 precipitates. *AIP Advances* **2018,** *8* (2), 025217.

46. Szklarska-Smialowska, Z.; Smialowski, M., Electrochemical Study of the Nickel-Hydrogen System. *Journal of The Electrochemical Society* **1963,** *110* (5), 444.

47. Soares, D. M.; Teschke, O.; Torriani, I., Hydride Effect on the Kinetics of the Hydrogen Evolution Reaction on Nickel Cathodes in Alkaline Media. *Journal of The Electrochemical Society* **1992,** *139* (1), 98-105.

48. Takano, N.; Yamamoto, H., Identification of nickel hydride phase in nickel matrix by optical microscope observation. *Results in Materials* **2020,** *5*, 100066.

49. Bourgeois, N.; Crivello, J.-C.; Cenedese, P.; Joubert, J.-M., Systematic First-Principles Study of Binary Metal Hydrides. *ACS Combinatorial Science* **2017,** *19* (8), 513-523.

50. Leckey, J. H.; Nulf, L. E.; Kirkpatrick, J. R., Reaction of Lithium Hydride with Water. *Langmuir* **1996,** *12* (26), 6361-6367.

51. Brown, C. A., Saline hydrides and superbases in organic reactions. VII. Potassium hydride, highly active new hydride reagent. Reactivity, applications, and techniques in organic and organometallic reactions. *The Journal of Organic Chemistry* **1974,** *39* (26), 3913-3918.

52. Thomé, L.; Traverse, A.; Brossard, L.; Bernas, H., Study of implanted nickel hydride via resistivity and hyperfine interaction experiments. *Hyperfine Interactions* **1981,** *9* (1), 559-562.

53. Motori, A.; Sandrolini, F.; Davolio, G., Electrical properties of nickel hydroxide for alkaline cell systems. *Journal of Power Sources* **1994,** *48* (3), 361-370.

54. Conway, B. E.; Angerstein - Kozlowska, H.; Sattar, M. A.; Tilak, B. V., Study of a Decomposing Hydride Phase at Nickel Cathodes by Measurement of Open - Circuit Potential Decay. *Journal of The Electrochemical Society* **1983,** *130* (9), 1825-1836.

55. Jeffrey Binns, W.; Zargarzadah, F.; Dehnavi, V.; Chen, J.; Noël, J. J.; Shoesmith, D. W., Physical and Electrochemical Evidence for the Role of a Mg Hydride Species in Mg Alloy Corrosion. *Corrosion* **2018,** *75* (1), 58-68.

56. Adhikari, S.; Lee, J.; Hebert, K. R., Formation of Aluminum Hydride during Alkaline Dissolution of Aluminum. *Journal of The Electrochemical Society* **2008,** *155* (1), C16.

57. Demkowicz, M.; Majewski, J., Probing Interfaces in Metals Using Neutron Reflectometry. *Metals* **2016,** *6* (1), 20.

58. Owejan, J. E.; Owejan, J. P.; DeCaluwe, S. C.; Dura, J. A., Solid Electrolyte Interphase in Li-Ion Batteries: Evolving Structures Measured In situ by Neutron Reflectometry. *Chemistry of Materials* **2012,** *24* (11), 2133-2140.

59. Sachtler, W. M. H., Work Function and Electrical Conductivity of Hydrogen Covered Nickel Films. The Effect of Contamination. *The Journal of Chemical Physics* **1956,** *25* (4), 751-752.

60. Lunder, O.; Lein, J. E.; Hesjevik, S. M.; Aune, T. K.; Nişancioğlu, K., Corrosion morphologies on magnesium alloy AZ 91. *Materials and Corrosion* **1994,** *45* (6), 331-340.

61. Ghali, E.; Dietzel, W.; Kainer, K.-U., General and localized corrosion of magnesium alloys: A critical review. *Journal of Materials Engineering and Performance* **2004,** *13* (1), 7-23.

62. Witten, T. A.; Sander, L. M., Diffusion-Limited Aggregation, a Kinetic Critical Phenomenon. *Physical Review Letters* **1981,** *47* (19), 1400-1403.

63. Zhou, Y.; Zeng, H. C., Kinetically Controlled Growth of Fine Gold Nanofractals from Au(I) via Indirect Galvanic Replacement Reaction. *ACS Applied Materials & Interfaces* **2015,** *7* (38), 21552-21561.

64. Samuelsson, I.-L., Effects of properties of sodium sulfate on precipitator performance. *O Papel (Brazil)* **2004,** *65*, 61-67.

65. Anzai, S.; Ozawa, K., Effect of Pressure on the Magnetic and Electrical Transition Point of the NiAs-Type NiS. *Journal of the Physical Society of Japan* **1968,** *24* (2), 271-274.

66. Jain, A.; Ong, S. P.; Hautier, G.; Chen, W.; Richards, W. D.; Dacek, S.; Cholia, S.; Gunter, D.; Skinner, D.; Ceder, G.; Persson, K. A., Commentary: The Materials Project: A materials genome approach to accelerating materials innovation. *APL Materials* **2013,** *1* (1), 011002.

67. de Jong, M.; Chen, W.; Angsten, T.; Jain, A.; Notestine, R.; Gamst, A.; Sluiter, M.; Krishna Ande, C.; van der Zwaag, S.; Plata, J. J.; Toher, C.; Curtarolo, S.; Ceder, G.; Persson, K. A.; Asta, M., Charting the complete elastic properties of inorganic crystalline compounds. *Scientific Data* **2015,** *2* (1), 150009.

68. Davis, J. R., *Nickel, Cobalt, and Their Alloys*. 2000.

69. Samsonov, G. V., Mechanical Properties of the Elements. In *Handbook of the Physicochemical Properties of the Elements*, Samsonov, G. V., Ed. Springer US: Boston, MA, 1968; pp 387-446.

70. Brug, G. J.; van den Eeden, A. L. G.; Sluyters-Rehbach, M.; Sluyters, J. H., The analysis of electrode impedances complicated by the presence of a constant phase

element. *Journal of Electroanalytical Chemistry and Interfacial Electrochemistry* **1984,** *176* (1), 275-295.

71. Estrada-Vargas, A.; Bandarenka, A.; Kuznetsov, V.; Schuhmann, W., In Situ Characterization of Ultrathin Films by Scanning Electrochemical Impedance Microscopy. *Analytical Chemistry* **2016,** *88* (6), 3354-3362.

72. Wohlfahrtmehrens, M., The mechanism of electrodeposition and operation of Ni(OH)2 layers. *Solid State Ionics* **1996,** *86-88*, 841–847.

73. Tunold, R.; Holtan, H.; Berge, M.-B. H.; Lasson, A.; Steen-Hansen, R., The corrosion of magnesium in aqueous solution containing chloride ions. *Corrosion Science* **1977,** *17* (4), 353-365.

74. Oldfield, J. W., Test techniques for pitting and crevice corrosion resistance of stainless steels and nickel-base alloys in chloride-containing environments. *International Materials Reviews* **1987,** *32* (1), 153-172.

75. Moll, D. V. V.; Salvarezza, R. C.; Videla, H. A.; Arvia, A. J., The Pitting Corrosion of Nickel in Different Electrolyte Solutions Containing Chloride Ions. *Journal of The Electrochemical Society* **1985,** *132* (4), 754-760.

76. Song, J.; Curtin, W. A., A nanoscale mechanism of hydrogen embrittlement in metals. *Acta Materialia* **2011,** *59* (4), 1557-1569.

77. Song, J.; Curtin, W. A., Atomic mechanism and prediction of hydrogen embrittlement in iron. *Nature Materials* **2013,** *12* (2), 145-151.

78. Pielaszek, J., MECHANISM OF MICROCRACK FORMATION IN NICKEL SINGLE CRYSTALS CATHODICALLY CHARGED WITH HYDROGEN. 1972.

79. Chen, Y. S.; Haley, D.; Gerstl, S. S. A.; London, A. J.; Sweeney, F.; Wepf, R. A.; Rainforth, W. M.; Bagot, P. A. J.; Moody, M. P., Direct observation of individual hydrogen atoms at trapping sites in a ferritic steel. *Science* **2017,** *355* (6330), 1196.

80. Takahashi, J.; Kawakami, K.; Kobayashi, Y., Origin of hydrogen trapping site in vanadium carbide precipitation strengthening steel. *Acta Materialia* **2018,** *153*, 193-204.

81. Dafft, E. G.; Bohnenkamp, K.; Engell, H. J., Investigations of the hydrogen evolution kinetics and hydrogen absorption by iron electrodes during cathodic polarization. *Corrosion Science* **1979,** *19* (7), 591-612.

82. Arantes, D. R.; Huang, X. Y.; Marte, C.; Kirchheim, R., *Hydrogen diffusion and permeation in micro- and nanocrystalline nickel*. 1993; Vol. 41, p 3215-3222.

83. Völkl, J.; Alefeld, G., Diffusion in solids. *AS Nowick and JJ Burton (New York: Academic)* **1975**.

84. Kirchheim, R.; Pundt, A., 25 - Hydrogen in Metals. In *Physical Metallurgy (Fifth Edition)*, Laughlin, D. E.; Hono, K., Eds. Elsevier: Oxford, 2014; pp 2597-2705.

85. Sieverts, A., Absorption of gases by metals. *Zeitschrift für Metallkunde* **1929,** *21*, 37-46.

86. Fukai, Y., *The Metal-Hydrogen System : Basic Bulk Properties*. 2005.

87. E. Fromm, E. G., Gase and Kohlenstoff in Metallen, Reine und angewandte Metallkunde in Einzeldarstellungen. *Springer* **1976**.

88. E. Fromm, G. H. o., *Intern. Metals Rev* **1980,** *25*.

89. Turnbull, A., Perspectives on hydrogen uptake, diffusion and trapping. *International Journal of Hydrogen Energy* **2015,** *40* (47), 16961-16970.

90. Taylor, C. D.; Neurock, M.; Scully, J. R., A First-Principles Model for Hydrogen Uptake Promoted by Sulfur on Ni(111). *Journal of The Electrochemical Society* **2011,** *158* (3), F36.

91. Faglioni, F.; Goddard, W. A., Energetics of hydrogen coverage on group VIII transition metal surfaces and a kinetic model for adsorption/desorption. *The Journal of Chemical Physics* **2005,** *122* (1), 014704.

92. Kresse, G.; Hafner, J., First-principles study of the adsorption of atomic H on Ni (111), (100) and (110). *Surface Science* **2000,** *459*, 287-302.

93. Shirazi, M.; Bogaerts, A.; Neyts, E. C., A DFT study of H-dissolution into the bulk of a crystalline Ni(111) surface: a chemical identifier for the reaction kinetics. *Physical Chemistry Chemical Physics* **2017,** *19* (29), 19150-19158.

94. Greeley, J.; Mavrikakis, M., A first-principles study of surface and subsurface H on and in Ni(111): diffusional properties and coverage-dependent behavior. *Surface Science* **2003,** *540* (2-3), 215-229.

95. Yatsymyrskyi, A.; Ischenko, E.; Gaidai, S.; Dyachenko, A.; Zakharova, T.; Lisnyak, V., *DFT Study of H2, H2O, and O2 Adsorption on Ni(111) Surface*. 2020; p 85-89.

96. Faglioni, F.; III, W. A. G., Energetics of hydrogen coverage on group VIII transition metal surfaces and a kinetic model for adsorption/desorption. *The Journal of Chemical Physics* **2005,** *122* (1), 014704.

97. Bai, L.; Harrington, D. A.; Conway, B. E., Behavior of overpotential—deposited species in Faradaic reactions—II. ac Impedance measurements on H2 evolution kinetics at activated and unactivated Pt cathodes. *Electrochimica Acta* **1987,** *32* (12), 1713-1731.

98. Grgur, B.; Krstajic, M., On the kinetics of the hydrogen evolution reaction on nickel in alkaline solution Part II. Effect of temperature. **2001**.

99. Bhardwaj, M.; Balasubramaniam, R., A new method for determining kinetic parameters by simultaneously considering all the independent conditions at an overpotential in case of hydrogen evolution reaction following Volmer–Heyrovsky–Tafel mechanism. *International Journal of Hydrogen Energy - INT J HYDROGEN ENERG* **2008,** *33*, 248-251.

100. Shinagawa, T.; Garcia-Esparza, A. T.; Takanabe, K., Insight on Tafel slopes from a microkinetic analysis of aqueous electrocatalysis for energy conversion. *Scientific Reports* **2015,** *5* (1), 13801.

101. Balluffi, R. W.; Allen, S. M.; Carter, W. C.; Kemper, R. A., *Kinetics of materials*. J. Wiley & Sons: Hoboken, N.J., 2005.

102. Jiang, L.; Verkhoturov, S.; Schweikert, E.; Demkowicz, M. J., Formation of Ni-O-H-S surface phases on cathodically charged Ni. *Corrosion Science* **2021**, 109424.

103. Yen, S. K., A retarding mechanism of thermally grown oxide films on hydrogen embrittlement of AISI 430 stainless steel. *Materials Chemistry and Physics* **1999,** *59* (3), 210-219.

104. Jeyaprabha, C.; Sathiyanarayanan, S.; Muralidharan, S.; Venkatachari, G., Corrosion inhibition of iron in 0.5 mol L-1 H2SO4 by halide ions. *Journal of the Brazilian Chemical Society* **2006,** *17*, 61-67.

105. Heusler, K. E.; Cartledge, G. H., The Influence of Iodide Ions and Carbon Monoxide on the Anodic Dissolution of Active Iron. *Journal of The Electrochemical Society* **1961,** *108* (8), 732.

106. Jegdić, B.; Dražić, D. M.; Popić, J. P., Open circuit potentials of metallic chromium and austenitic 304 stainless steel in aqueous sulphuric acid solution and the influence of chloride ions on them. *Corrosion Science* **2008,** *50* (5), 1235-1244.

107. Elhamid, M. H. A.; Ateya, B. G.; Pickering, H. W., The Effect of Iodide Ions on the Kinetics of Hydrogen Absorption by Iron. *Journal of The Electrochemical Society* **2000,** *147* (6), 2258-2262.

108. Verbraeken, M. C.; Cheung, C.; Suard, E.; Irvine, J. T. S., High H− ionic conductivity in barium hydride. *Nature Materials* **2015,** *14* (1), 95-100.

109. Radhakrishnan, T. P.; Shreir, L. L., Permeation of hydrogen through steel by electrochemical transfer—I. Influence of catalytic poisons. *Electrochimica Acta* **1966,** *11* (8), 1007-1021.

110. Berkowitz, B. J.; Burton, J. J.; Helms, C. R.; Polizzotti, R. S., Hydrogen dissociation poisons and hydrogen embrittlement. *Scripta Metallurgica* **1976,** *10* (10), 871-873.

111. Robinson, S. L.; Moody, N. R.; Myers, S. M.; Farmer, J. C.; Greulich, F. A., The Effects of Current Density and Recombination Poisons on Electrochemical

Charging of Deuterium into an Iron ‐ Base Superalloy. *Journal of The Electrochemical Society* **1990,** *137* (5), 1391-1397.

112. Bockris, J. O. M.; McBreen, J.; Nanis, L., The Hydrogen Evolution Kinetics and Hydrogen Entry into a-Iron. *Journal of The Electrochemical Society* **1965,** *112* (10), 1025.

113. Dull, D. L.; Nobe, K., EFFECT OF THIOUREAS AND TRIAZOLES ON HYDROGEN PENETRATION RATES IN IRON. *CORROSION* **1979,** *35* (12), 535-540.

114. Jerkiewicz, G.; Borodzinski, J. J.; Chrzanowskia, W.; Conway, B. E., Examination of Factors Influencing Promotion of H Absorption into Metals by Site ‐ Blocking Elements. *Journal of The Electrochemical Society* **1995,** *142* (11), 3755-3763.

115. Fuji, H.; Fujishiro, T.; Sagara, M.; Masaki, Y.; Hara, T., Effect of Hydrogen Sulfide on Hydrogen Entry Behavior of Low Alloy Steel. *ISIJ International* **2020,** *60* (4), 739-744.

116. Frumkin, A. N., *Advances in Electrochemistry and Electrochemical Engineering* **1962,** *Vol. 3* (Interscience), 287.

117. Hickling, A., THE ANODIC BEHAVIOUR OF METALS .1. PLATINUM. *Transactions of the Faraday Society* **1945,** *41* (6), 333-&.

118. Newman, J. F.; Shreir, L. L., Role of hydrides in hydrogen entry into steel from solutions containing promoters. *Corrosion Science* **1969,** *9* (8), 631-641.

119. Hill, M. L.; Johnson, E. W., HYDROGEN IN COLD WORKED IRON-CARBON ALLOYS AND THE MECHANISM OF HYDROGEN EMBRITTLEMENT.

Transactions of the American Institute of Mining and Metallurgical Engineers **1959,** *215* (4), 717-725.

120. Kim, K. T.; Park, J. K.; Lee, J. Y.; Hwang, S. H., Effect of alloying elements on hydrogen diffusivity in ?-iron. *Journal of Materials Science* **1981,** *16* (9), 2590-2596.

121. Huot, J.; Liang, G.; Schulz, R., Mechanically alloyed metal hydride systems. *Applied Physics a-Materials Science & Processing* **2001,** *72* (2), 187-195.

122. Zaluska, A.; Zaluski, L.; Strom-Olsen, J. O., Nanocrystalline magnesium for hydrogen storage. *Journal of Alloys and Compounds* **1999,** *288* (1-2), 217-225.

123. Dietrich, S.; Haase, A., Scattering of X-rays and neutrons at interfaces. *Physics Reports* **1995,** *260* (1), 1-138.

124. Zhou, X.-L.; Chen, S.-H., Theoretical foundation of X-ray and neutron reflectometry. *Physics Reports* **1995,** *257* (4-5), 223-348.

125. Penfold, J.; Thomas, R. K., The application of the specular reflection of neutrons to the study of surfaces and interfaces. *Journal of Physics: Condensed Matter* **1990,** *2* (6), 1369.

126. Dong, C. F.; Fu, A. Q.; Li, X. G.; Cheng, Y. F., Localized EIS characterization of corrosion of steel at coating defect under cathodic protection. *Electrochimica Acta* **2008,** *54* (2), 628-633.

127. Lu, Y. C.; Ives, M. B., The improvement of the localized corrosion resistance of stainless steel by cerium. *Corrosion Science* **1993,** *34* (11), 1773-1785.

128. Duboscq, J.; Sabot, R.; Jeannin, M.; Refait, P., Localized corrosion of carbon steel in seawater: Processes occurring in cathodic zones. *Materials and Corrosion* **2019,** *70* (6), 973-984.

129. Alkire, R.; Siitari, D., The Location of Cathodic Reaction during Localized Corrosion. *Journal of The Electrochemical Society* **1979,** *126* (1), 15-22.

130. Macdonald, D. D., Some personal adventures in passivity—A review of the point defect model for film growth. *Russ. J. Electrochem.* **2012,** *48* (3), 235-258.

131. Macdonald, D. D., PassivityÐthe key to our metals-based civilization. *Pure Appl. Chem* **1999,** *71* (6), 951-978.

132. Macdonald, D.; Engelhardt, G. R., Predictive Modeling of Corrosion. *Shreir's Corrosion* **2010,** *2*, 1630-1679.